Evolution of Turbidity Currents: New insights from direct field measurements

CATHARINA JANNA HEEREMA

SLATE
Submarine Landslides and their impact on European continental margins

Durham University

Evolution of Turbidity Currents:

New insights from direct field measurements

Catharina (Kate) J. Heerema

This thesis is submitted in partial fulfilment of the requirements for the degree of

Doctor of Philosphy

Earth Sciences Department

Durham University

Durham, 2020

Primary Supervisor: Prof. Peter. J. Talling

Secondary Supervisor: Dr. Matthieu J.B. Cartigny

Abstract

Underwater sediment density flows, including turbidity currents, are capable of transporting vast amounts of sediment, nutrients and pollutants to the deep-sea. These flows can be powerful, causing damage to seafloor infrastructure. Understanding how the flow velocity and magnitude develops over distance is thus important for risk assessments, as well as determining sediment fluxes. However, as few direct measurements are available, these flows remain rather poorly understood. This thesis aims to use three direct monitoring datasets from three different oceanographic settings worldwide that have captured turbidity currents in unusual detail, allowing for unique analysis of their flow evolution.

Detailed measurements of turbidity currents in Monterey Canyon, offshore California, show that their evolution depends on the initial velocity and the availability of an easily erodible substrate. Turbidity currents exceeding a velocity threshold can plateau with near-uniform velocities, and thus run out over greater distances. A new model is proposed for how these near-uniform velocities are obtained. In the Var Canyon-River system, France, nearshore measurements are used to analyse turbidity current velocity structures, and how these develop over distance. Turbidity currents are shown to self-organise over short distances by amalgamation of velocity peaks, which is partly controlled by erodible substrate availability. This efficient self-organisation occurs within 10 km, after which the original trigger is indiscernible. This has important implications for interpreting turbidity current deposits. Bute Inlet, British Columbia, is one of the most complete studies, where source-to-sink direct measurements are combined with sediment cores. These data allow for a unique analysis of turbidity current activity over space and time. The current-day channelized system is highly active with yearly events, although these events are low magnitude. In contrast, distally the system shows high magnitude events occurring on centennial time scales. These data suggest that infrequent mechanisms control large-scale events currently not observed directly. This thesis provides a detailed analysis of turbidity current development over distance, essential for determination of sediment fluxes and hazard assessment.

Contents

I, Kate Heerema, declare that this thesis, which I submit for the degree of Doctor of Philosophy at Durham University, is my own work and not substantially the same as any which has previously been submitted at this or any other university. The copyright of this thesis rests with the author. No quotation from it should be published without the author's prior written consent and information derived from it should be acknowledged. This project has received funding from the European Union's Horizon 2020 research and innovation program under the Marie Skłodowska-Curie grant agreement No 721403 - ITN SLATE.

Durham, April 21, 2021

Kate Heerema

Acknowledgements

First of all, many thanks to my supervisors at Durham University, Peter Talling and Matthieu Cartigny, for providing continuous support, guidance and encouragement. Pete, thanks for all the opportunities you have given me, I have had an incredibly diverse and rich PhD because of it. Not many people will have had the opportunity to pass the equator by ship for science, conduct research in the incredible scenery of Bute Inlet, or visit all the collaborating research insitutes. Matthieu; thanks for the laughs, the Dutch down-to-earthness, the patience and the discussions, both scientific and other. These conversations always lifted me up, and got me ready for another day of hard PhD work. Thanks as well to the wider turbidity current research group in and outside of Durham, for continuous support, discussions and crosswords.

Throughout my PhD I have had many opportunities to visit other research institutes abroad. These experiences have enriched my PhD beyond acknowledgements. Not only because of the science during these research stays, but even more so because of the incredible hospitality from all the people I met whilst on my research stays. I want to thank everyone at NGI Oslo for teaching me about numerical modelling and Norwegian culture. Those 6 months in Norway were an experience on their own, which I thoroughly enjoyed. Thanks to all at IFREMER for welcoming and hosting me, especially Ricardo. Thanks to everyone at MBARI, specifically Charlie and Mary Paull for hosting me. Finally, thanks to all at IOS Sidney. My many visits to IOS were always an incredible experience and very welcoming. The people, research cruise, lab work and snow storm were all amazing.

The opportunities given throughout my PhD are because of the ITN SLATE. I would like to thank all people in SLATE for this amazing journey, it was a wild ride. Specifically, thanks Rachel, Ricarda and Madda for the good chats, laughs, positivity and adventures. I am looking forward to our next adventure in the mountains!

Thanks to all fellow PhDs, making my time in Durham worthwhile. Kate Gallagher for many ice, snow and climbing adventures, in Scotland and Iceland, with more to

follow. Thanks to Eloïse and Sean (and Henk a.k.a. Hester), these last months have been memorable, thanks for your continuous support, with cocktails, food, laughs and even scientific discussions. Ilaria, my BBB, thanks for your support and laughs. Simon, thanks for the climbing, skiing, hiking, snowshoeing (sans snowshoes), and all other outdoor fun. Marie-Anne, thanks for all the laughs, climbing sessions and road trips. Liz, Nico, Sean R, Sophie, Chris, Dimitrios, Pavlos, thanks for the laughs, making the time in Durham fun!

My final thanks are to my friends and family abroad, helping me from afar, yet close by. Tack Vero, för allt. För din positivitet, skratt och tårar, och alla samtal detta håller mig upplyft, vanlight och lite galen. Kram på dig och jag saknar dig.

Voor mijn vrienden in Nederland. Bedankt voor jullie continue steun. Annikaas, Cato, Wes, voor altijd 2JD, dat nu toch behoorlijk aan het uitbreiden is, jullie zijn toppers. Ik ben benieuwd waar we staan over 5 jaar! Auk, Eric, Joost, Roel, voor de grappen, impressies, wolkenluchten, en blijkbaar yoga sessies. Uiteindelijk is mijn lange reis naar mijn PhD begonnen met jullie bij BWA, inclusief zoutzuur en gutsen.

Als laatste wil ik mijn familie bedanken, want zonder jullie was dit een onmogelijke reis geweest. Bedankt voor alles. Op naar de volgende reis!

Chapter 1

Introduction

1.1 Rationale

Subaqueous density flows, including turbidity currents, are driven by the excess density from the sediment load they carry (Kneller and Buckee, 2000). Turbidity currents are of interest for two main reasons. Firstly, their transport capacity makes these flows one of the most volumetrically important mechanisms of transporting sediment (Talling, 2014). Not only do these turbidity currents play a major role in transporting sediments, they are also very efficient in organic carbon burial, affecting the global carbon cycle (Galy et al., 2007, Hage et al., 2020). Furthermore, these flows contain nutrients essential for deep-sea ecosystems (Rowe, 1972, Vetter and Dayton, 1999); and are capable of transporting microplastics and other pollutants to the deep-sea (Gwiazda et al., 2015, Pohl et al., 2020). Second, turbidity currents are themselves often powerful and violent. Thereby, these flows can impact seafloor infrastructure, including oil and gas pipelines, as well as seafloor telecommunication cables transporting data across the globe (Canals et al., 2004, Carter et al., 2014, Sequeiros et al., 2019). Understanding how these flows develop over distance will improve hazard assessments, and improve our knowledge on the particle fluxes occurring from the continent to the deep sea. Therefore, we need a better understanding of how flows and their velocity, velocity signature and frequency changes with distance from source in particular. However, there are few direct measurements of these submarine flows in action, due to inaccessible locations, sometimes infrequent occurrence and ability to damage instruments placed in their path. This thesis uses three detailed direct monitoring data sets, which are used to understand how these flows develop over distance, and thereby their impact on seafloor hazards and particle fluxes.

1.2 Aims

The overall aim of this thesis is to use direct field measurements of turbidity currents to understand the evolution of flows over time and space. In particular, three unusually detailed flow monitoring datasets are analysed which include acoustic Doppler current profiler (ADCP) data. ADCPs return detailed measurements of velocity and backscatter (as proxy for sediment concentration) through the water column over a set interval. The first dataset is from Monterey Canyon, offshore California, and is one of the most detailed monitoring field experiments. This dataset includes 18 months of observations, at six mooring locations at sub-minute intervals. The second dataset includes especially proximal moorings in the Var Canyon, offshore South-East France. The third dataset includes the first source-to-sink ADCP measurements, in combination with sediment cores in Bute Inlet, a fjord in British Colombia, Canada.

These datasets are used to increase our general understanding on turbidity current flow evolution. Specifically, three specific research questions are addressed:

1. What determines the evolution of flows over distance? (Chapter 2)
2. Can you identify the trigger of a flow from its velocity signature? (Chapter 3)
3. How do the frequency and magnitude of turbidity currents change with distance, and what controls this pattern? (Chapter 4)

1.3 Previous Understanding of Turbidity Currents: Outcrops, Modelling and Experiments

Due to their violent and episodic nature, measuring turbidity currents directly is challenging. Much of our past understanding of turbidity currents has thus come from analysis of their deposits in sediment cores and rock outcrops, physical experiments in the laboratory, numerical and theoretical models.

Deposits, in rock outcrops or sediment cores, have often been the only direct information available on turbidity currents (e.g. Kuenen and Migliorini, 1950). These vertical sedimentary sequences are used to identify and describe turbidity currents and their flow properties (i.e. Bouma, 1962). As some examples; Hubbard et al. (2014) have suggested channel evolution models, which emphasises the bypass function of channels. Stevenson et al. (2014) have used sediment cores to reconstruct flows, and found relatively thin, fast, flows capable of carrying large sand volumes across a flat basin

floor. However, deposits only record the depositional phases of often decelerating flows, and inferring information such as the sediment support mechanism from a deposit is problematic as certain deposits can form in multiple ways (Talling et al., 2012).

Theoretical models have been used to predict turbidity current behaviour, such as the k-ϵ turbulence model (Eidsvik and Brørs, 1989) or the 4-equation model by Parker et al. (1986). Such models are typically compared onto laboratory scale flows, whose character may differ from full-scale flows in oceans or lakes due to scaling issues.

Yet key insights have come from physical experiments, where Kuenen (1937) was a pioneer demonstrating their potential existence and ability to form submarine canyons. Further insights include for instance; depositional models based on the sediment support mechanism (Middleton and Hampton, 1973); a sediment transfer mechanism where even dilute river plumes are capable to transfer sediments and initiate turbidity currents (Parsons et al., 2001); or experiments showing that a minor increase in sediment concentration, especially muds, can dampen turbulence effectively leading to rapid sediment settling and deceleration (Baas et al., 2009). Sequeiros et al. (2009, 2018) were able to generate self-accelerating turbidity currents in physical experiments and subsequently analyse their internal structure, thereby testing and advancing the theoretical model originally set up by Parker et al. (1986). Limitations on laboratory models include the necessity of scaling down experiments (Peakall et al., 1996). Laboratory models are often limited to speeds of tens of cm s^{-1}, and a few metres length (i.e. Middleton, 1966), whereas field measurements have shown turbidity currents can reach up to 19 m s^{-1} and can be several thousand km runout (Heezen and Ewing, 1952, Piper et al., 1999).

Finally, deposits and laboratory experiments have been compared to results from numerical modelling. For example, the 1979 Nice event was simulated by Mulder et al. (i.e. 1997). Luchi et al. (2018) demonstrate the potential for long runout of turbidity currents by using a two-layer model. However, numerical models depend on their input parameters, which are often not well-constrained. Furthermore, key assumptions are necessary, such as depth-averaged flow properties, or uniform grain sizes (c.f. Mulder et al., 1997, Parsons et al., 2007, Cantero et al., 2012, Luchi et al., 2018).

Although these depositional, laboratory and numerical models have resulted in many key insights about turbidity currents, each approach has significant limitations. This means there is a compelling need to directly measure active and full-scale turbidity currents in the field, at a large scale. The availability of field data from active events

can make a step change in testing numerical or theoretical models, and help to design laboratory experiments that more accurately reproduce field-scale flows. Testing of models against field data can then become more common, and with more field data emerging, it is likely to be the new standard (i.e. Mulder et al., 1997, Løvholt et al., 2019, van Rijn et al., 2019).

1.4 Previous Direct Monitoring

In-situ, direct, measurements of turbidity currents have become more commonplace, and give more detailed insights into flow properties. It is a developing field, with more detailed datasets, new instruments, an increasing number of simultaneous mooring deployments, higher resolution data, and increasingly more global locations.

1.4.1 Monitoring studies (Pre-ADCPs; '70s and '80s)

The timing of cable breaks has helped determine flow paths and transit velocities (i.e. Heezen and Ewing, 1952, Piper et al., 1999, Gavey et al., 2017). However, using cable breaks to determine transit velocities relies on the assumption that the front of the flow is responsible of the cable break, which may not be the case (Sumner and Paull, 2014). Inman et al. (1976) and Prior et al. (1987) were the first to directly measure turbidity currents using current meters at a fixed height. These studies measured currents up to 1.9 and 3 m/s, establishing down-canyon motion by discrete pulses, capable of transporting coarse sand several meters above the seafloor. These studies were the first to show that turbidity currents can be measured directly in the field.

1.4.2 Monitoring studies (ADCPs; '00s - onwards)

ADCPs measure velocities and acoustic backscatter in the water column above or below the instrument, and can thus provide unique data on turbidity currents over a set time interval, as well as being placed outside the main flow itself. ADCPs have been placed at multiple submarine locations to monitor turbidity current activity (Fig. 1.1; see Clare et al. (2017, 2020)). These locations include submarine canyons extending for hundreds of kilometers (i.e. Puig et al., 2004, Xu et al., 2004, Liu et al., 2006, de Stigter et al., 2007, Xu, 2010, Khripounoff et al., 2012, Azpiroz-Zabala et al., 2017, Paull et al., 2018); and smaller submarine systems (i.e. Hughes Clarke, 2016, Lintern et al., 2016, Hage et al., 2019, Normandeau et al., 2020). However, some

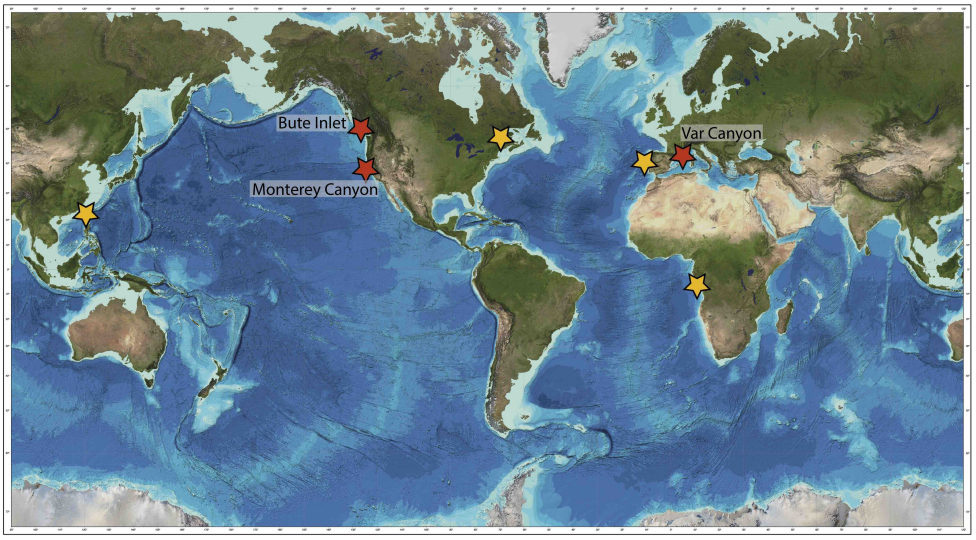

FIGURE 1.1: Locations with deployments of acoustic Doppler current profilers (ADCPs) used to measure turbidity currents. The stars highlighted in red are locations discussed in this thesis. Monterey and Var Canyon also have previous datasets with ADCP measurements. See Clare et al. (2017, 2020) for an overview of direct measurement locations. Image reproduced and modified from the GEBCO world map 2014, www.gebco.net.

deployments experienced heavy damage to the in-situ placed instruments (i.e. Inman et al., 1976, Sumner and Paull, 2014, Paull et al., 2018, Clare et al., 2020). Even though these events can be powerful, when comparing to the depositional record over geologic timescales, in-situ observations are limited to the small-scale flows that are constrained to the proximal canyon (i.e. Talling et al., 2015, Paull et al., 2018). Nevertheless, these direct measurements have led to important insights and step changes in our understanding on turbidity currents. For instance, Azpiroz-Zabala et al. (2017) found that flows can stretch markedly, leading to prolonged turbidity currents which can last up to a week. Liu et al. (2016) found that typhoon regimes lead to erosive turbidity currents in Gaoping Canyon, offshore Taiwan. In Monterey Canyon, Xu et al. (2004) were the first to measure vertical velocity profiles of turbidity currents, and Paull et al. (2018) measured the fastest in-situ turbidity currents to date, reaching up to 7 m s^{-1}. High-resolution repeat multibeam surveys in Howe Sound, British Columbia, led to new insights in triggering of events and their subsequent bedforms (Hughes Clarke et al., 2012, Hage et al., 2019). For instance, Hage et al. (2019) found that extremely dilute river plumes are able to trigger turbidity currents in combination with tidal forcing. Furthermore, these direct measurements can be used to verify, calibrate and improve laboratory, numerical and depositional models (Parsons et al., 2007, Kneller et al., 2016, Symons et al., 2016, Maier et al., 2019). By improving these turbidity current models, they will in turn give insights in less frequent, higher magnitude events with a more hazardous potential not measured directly.

1.5 Acoustic Doppler Current Profilers (ADCPs)

The deployment of acoustic Doppler current profilers (ADCPs) has drastically increased the ability to monitor turbidity currents in detail and obtain in-situ measurements of velocity structures (Clare et al., 2017). Chapter 2 and 4 use these data predominantly to derive flow arrival times, and hence transit velocities; whilst Chapter 3 looks at ADCP-derived time series of internal flow velocity.

1.5.1 Principles

Acoustic Doppler current profiler (ADCP) measurements are current profiles over depth, with each bin having a unique value (Fig. 1.2A). ADCPs use the Doppler shift principle to measure flow velocity (Teledyne, 2011). Four transducers, or beams, are mounted at an angle on the ADCP and transmit and receive sound pulses called pings (Fig. 1.2A). The Doppler shift and strength of the emitted versus received sound pulse is used to determine velocity and backscatter at each vertical cell. The velocity measurements are based on the Doppler shift between emitted and received frequency, and require four beams to calculate velocities in north, east and up directions, and to include a measurement error estimate (Teledyne, 2011). The echo intensity is the strength of returned signal, and can be converted to backscatter when correcting for noise attenuation and converted to sediment concentration when assuming a single grain size (Thorne and Hanes, 2002, Azpiroz-Zabala et al., 2017, Simmons et al., 2020). The data is projected over time, with each ensemble equalling an average of multiple pings.

1.5.2 Limitations and considerations

There are a few considerations for deploying and using ADCPs (Clare et al., 2020). ADCPs can be installed either upward or downward looking. The upward looking ADCPs will typically be moored on the seafloor to capture passing turbidity currents, making this configuration more vulnerable to direct damage from turbidity currents (Clare et al., 2017). Therefore, configurations with downward looking ADCPs are more common in turbidity current research. Here, there is still a possibility to be dragged down towards the seafloor during the passage of a turbidity current, or mounting cables can snap (i.e. Paull et al., 2018). The majority of the data discussed in this thesis is from downward looking ADCPs. The ADCPs can have various

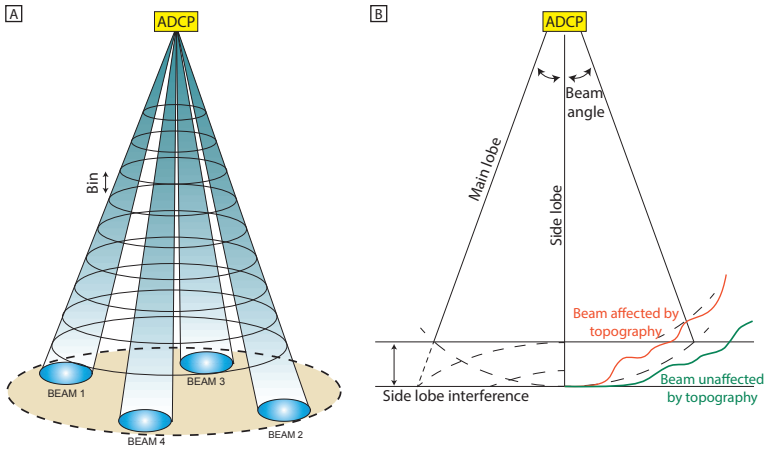

FIGURE 1.2: Basic working principles of an acoustic Doppler current profiler (ADCP). A) Four beams are used to calculate velocities and backscatter, the latter as a proxy for sediment concentration. Measurements are at set height intervals (bins). Image modified after Teledyne (2010). B) Interference types on a downward looking ADCP. The left depicts side lobe interference, where there is a region of interfering signals as the side lobe hits a surface before the main lobe. The right shows interference from bathymetry. Both are due to an overpowering echo from the first sound wave arrival. The footprint (height and angle of the ADCP) influences the extent of interference. Image modified after Clare et al. (2020).

frequencies at which the sound pulses are emitted. The studies presented here in Chapter 2, 3, and 4 use ADCP frequencies of 75, 300 and 600 kHz. Other studies have used 1200 kHz as well (i.e. Wynn et al., 2014, Hughes Clarke, 2016). The choice in frequency is a consideration between detail and range, as a higher frequency will result in more detail over a shorter range as energy dissipates quickly. Lower frequencies lead to greater range of measurements of the water column, but with less detail (Clare et al., 2020).

Major limitations when using ADCP measurements are in the near-bed region. Unfortunately, this region, where the interaction between turbidity currents and the seafloor occurs, is of particular interest (Talling et al., 2015). Firstly, a major limitation is the inability of ADCPs to penetrate higher density flows, leading to a blanking region often near the bed (i.e. Simmons et al., 2020). Second, side lobe interference and bathymetry interference can affect the lower bins of the data (Fig. 1.2B). Side lobe interference is due to the offset in the direct (side) and angled (main) lobe orientations, where the sidelobe will be in contact with the seafloor first. This contact leads to an overpowering echo (Teledyne, 2011). The bathymetry interference is also due to this overpowering echo, but in this case due to local bathymetry protruding into the beam (Clare et al. (2020); Fig. 1.2B). With an increasing footprint (ADCP mounting height in combination with beam angle) sidelobe interference increases,

and interference from i.e. canyon walls becomes more likely. However, it is preferable to mount an ADCP outside the main turbidity current, for safekeeping, as well as measurements. Therefore, ADCP mounting height is a careful consideration.

Finally, general limitations are battery power and memory storage, leading to reduced time intervals or reduced deployment times. Chapter 2 consists of three separate, but consecutive, 6-month deployments, cumulating to an 18-month monitoring study. Most measurements are at 30 s intervals, with one mooring at 10 s intervals. Chapter 3 had one ADCP deployed over a 7-month period, which collected over 20 min intervals. Chapter 4 consists of two separate deployments, 5 months in 2016 and a 7-month deployment in 2018. Time intervals varied between 2.5 seconds and 10 seconds per mooring.

1.6 Turbidity Current Terminology

A consequence of the difficulty of measuring turbidity currents in nature is the considerable debate on the definition of turbidity currents, due to a lack of suitable measurements (c.f. Talling et al., 2012). There are numerous definitions of turbidity currents, based on for instance their sediment support mechanism (i.e. Mulder and Alexander, 2001), flow state (i.e. Lowe, 1979) or flow rheology (i.e. Shanmugam, 2002). For now, these difficulties remain as direct measurements cannot always observe the physical processes in the field, and deposit-based classifications remain important (c.f. Parsons et al. (2007), Talling et al. (2012)). Throughout this thesis, the term turbidity current is used as a general term depicting a sediment density flow, driven by their excess sediment density (i.e. Middleton and Hampton, 1973). In Chapter 3 specifically, this is further specified that the dominant particle support, fluid turbulence, can be damped within near-bed layers, following Cantero et al. (2012). The terms "flows" and "events" are used interchangeably to depict a singular turbidity current episode. Further specific terminology necessary for Chapter 2 and Chapter 3 is specified in their respective terminology sections.

1.7 Thesis Structure

The core of this thesis are three scientific chapters, each seeking to understand the evolution of turbidity currents. Each chapter uses field monitoring data from a different submarine turbidity current system (Fig. 1.1, red stars). These datasets include

the most ADCPs deployed to date along turbidity current pathways, and only source-to-sink moorings covering an entire submarine system. These unique fields datasets are used to answer fundamental questions about flow behaviour. These questions include how these flows develop over distance, in terms of their front velocity (Chapter 2), internal velocity structure (Chapter 3) and frequency (Chapter 4). How flows develop over distance determines their impact on seafloor infrastructure, and how they transfer sediment, nutrient and pollutants to the deep sea. Thereby, in a broader perspective, each chapter contributes to improved hazard assessments, and to our knowledge on particle fluxes to the deep sea.

Chapter 2 – What determines the evolution of flows over distance?

Fundamental theories from the 60s and 80s have suggested that turbidity currents either erode, thereby become denser and accelerate (ignite) or deposit, become more dilute and decelerate (dissipate) (Bagnold, 1962, Parker, 1982, Parker et al., 1986). Another, intermediate flow state has been suggested where erosion and deposition are balanced (autosuspension)(Pantin, 1979). These theories have been tested in laboratory settings and numerical models, but there has not been a dataset with enough direct measurement stations in one deployment allowing for field testing of these suggested flow modes (i.e. Southard and Mackintosh, 1981, Fukushima et al., 1985, Sequeiros et al., 2009, Hu et al., 2015). Chapter 2 presents data from Monterey Canyon, where six moorings covering 52 km were deployed over 18 months (Paull et al., 2018). This dataset is the most exhaustive dataset on turbidity currents to date, and allows for the fundamental questions on the evolution of turbidity currents stipulated above to be addressed. The velocity of 13 events is analysed, via both the direct ADCP measurements at each mooring and transit velocities between moorings. All events initially ignite. The initial velocity of events severely impacts the subsequent runout distance. Marginal increases in initial velocities lead to substantially greater runout distances. If the velocity exceeds a threshold, flows can autosuspend. Additionally, seafloor substrate influences the ability of flows to ignite at a later stage.

Chapter 3 – Can you identify the trigger of a flow from its velocity signature?

In the literature, unique velocity structures that form a signature have been assigned to flood-triggered turbidity currents and their subsequent deposits (Mulder et al., 2003, Nakajima, 2006, Khripounoff et al., 2012, Zavala and Pan, 2018). These unique signatures have been used to reconstruct palaeo-floods, and their recurrence rates (i.e. Plink-Björklund and Steel, 2004, Nakajima, 2006). Direct measurements so far have shown ambiguity in these velocity signatures, suggesting it is not as straight-

forward to recognise flood-triggered turbidity currents as previously suggested (i.e. Khripounoff et al., 2012, Liu et al., 2012, Hage et al., 2019). Chapter 3 presents data from Var Canyon, offshore France in the Mediterranean. Here, we obtained detailed velocity measurements from an ADCP mooring 6 km offshore. In combination with river influx data, these velocity measurements provide insights in the recognition of river flood-triggered turbidity currents. Another mooring 16 km offshore, with a current meter, shows how the velocity signature of turbidity currents evolves over distance. We measured three events, two of which can be directly related to river peak discharges. Proximally, the data showed that the flood-triggered velocity signatures can (partially) be found, but that the event that is not related to a river flood actually meets most of the flood-triggered criteria. At the distal station, amalgamation and self-organisation of events leads to signal shredding, where the velocity signatures follow a more classic, surge-like velocity structure. Our findings have important implications for interpretation of flood-related sedimentary deposits. Recognition becomes particularly difficult when moving further offshore, as turbidity currents quickly self-organise and discard their trigger-specific criteria.

Chapter 4 – How do the frequency and magnitude of turbidity currents change with distance, and what controls this pattern?

As turbidity currents are capable of transporting vast amounts of sediment, nutrients, pollutants and plastics to the deep sea, it is important to understand over what timescales transport to the deep sea typically occurs. However, understanding the full-scale transportation of turbidity currents has been predominantly dependent on indirect methods such as outcrops, seismic data or sediment cores. Most direct measurements of turbidity currents are limited to the proximal extent of submarine systems. In Chapter 4, we present direct measurements from Bute Inlet, a Canadian fjord in British Colombia. Six ADCPs have been placed in this small-scale submarine channel system covering source-to-sink. Additional sediment cores throughout the submarine system, including the distal deep basin, provide a sedimentary record of past events. The combination of these datasets provides a unique insight in the frequency of turbidity currents over time and space. Three event frequencies are found. The direct ADCP measurements show frequent events, with ca. 100 events occurring near the delta, and one event reaching the lobe every year. The sediment cores show that coarse-grained sands are deposited on the terraces above the current-day thalweg, every ∼20 years. The deep basin shows a change from mud deposits to massive sand deposits, a change that occurred approximately 240 years ago. The frequencies of these events is found to be comparable to an adjacent Canadian fjord (Stacey et al., 2019).

Chapter 2

What determines the evolution of flows over distance?

This chapter has been published in *Earth and Planetary Science Letters*: **Heerema CJ**, Talling PJ, Cartigny MJ, Paull CK, Bailey L, Simmons SM, Parsons DR, Clare MA, Gwiazda R, Lundsten E, Anderson K, Maier KL, Xu JP, Sumner EJ, Rosenberger K, Gales J, McGann M, Carter L, Pope E and the CCE team (2020). 'What determines the downstream evolution of turbidity currents?'. Earth and Planetary Science Letters. `https://doi.org/10.1016/j.epsl.2019.116023`

Kate Heerema gratefully used the data collected by co-authors, and analysed the ADCP data. Conceptualisation of the paper, and analysis of the data was carried out by KH, with key input from supervisors PJT and MJBC. The paper was written by KH, with various comments from all co-authors. The grain-size data analysis, internal tide data and mooring deployments were provided by co-authors. The main author would like to acknowledge the fruitful discussions and invaluable input from the co-authors and their patience during the revision process.

2.1 Abstract

Seabed sediment flows called turbidity currents form some of the largest sediment accumulations, deepest canyons and longest channel systems on Earth. Only rivers transport comparable sediment volumes over such large areas; but there are far fewer measurements from turbidity currents, ensuring they are much more poorly understood. Turbidity currents differ fundamentally from rivers, as turbidity currents are

driven by the sediment that they suspend. Fast turbidity currents can pick up sediment, and self-accelerate (ignite); whilst slow flows deposit sediment and dissipate. Self-acceleration cannot continue indefinitely, and flows might reach a near-uniform state (autosuspension). Here we show how turbidity currents evolve using the first detailed measurements from multiple locations along their pathway, which come from Monterey Canyon offshore California. All flows initially ignite. Typically, initially-faster flows then achieve near-uniform velocities (autosuspension), whilst slower flows dissipate. Fractional increases in initial velocity favour much longer runout, and a new model explains this bifurcating behaviour. However, the only flow during less-stormy summer months is anomalous as it self-accelerated, which is perhaps due to erosion of surficial-mud layer with fine sands mid-canyon. Turbidity current evolution is therefore highly sensitive to both initial velocities and seabed character.

2.2 Introduction

Seafloor sediment density flows (called turbidity currents) are the dominant global mechanism for transporting sediment from the continental shelf to the deep sea. These flows play a crucial role in global organic carbon burial and geochemical cycles (Galy et al., 2007), and supply of nutrients to deep-sea ecosystems (Canals et al., 2006). Only rivers transport sediment over comparable areas, although one turbidity current can carry more sediment than the annual flux from all the world's rivers combined (Talling et al., 2013). Powerful turbidity currents can badly damage seafloor infrastructure, including oil and gas pipelines, and telecommunication cable networks. The latter carry over 95 % of global data traffic (Carter et al., 2014), forming the backbone of the internet and financial markets. Turbidity current deposits host valuable oil and gas reserves, and form thick sequences of ancient rocks that record Earth's history (Nilsen et al., 2008). The downstream evolution of velocities and runout lengths controls how sediment is dispersed, the resulting deposit character and shape, and hazards to seafloor infrastructure. It is thus important to understand how turbidity currents work, especially what controls their runout, and changes in flow velocity with distance.

Turbidity currents differ profoundly from terrestrial rivers; unlike rivers they are driven by the weight of sediment they carry, and this sediment can be entrained or deposited onto the seafloor along turbidity current pathways. Previous work suggested that exchange of sediment with the seabed may lead to positive feedbacks, such that turbidity current behaviour is inherently unstable and diverges (Fig. 2.1)

(Bagnold, 1962, Parker, 1982). These studies proposed that flows which erode sediment become denser, and thus accelerate, causing increased erosion, and further acceleration (Fig. 2.1A). This process is called ignition, and it may play a pivotal role in producing powerful and long runout flows. Conversely, flows that deposit sediment may decelerate, leading to further deposition ('dissipation'; Fig. 2.1B). Such positive feedbacks may produce thresholds in behaviour that depend on small differences in initial flow state. It has also been proposed that flows could achieve a near-uniform state in which erosion is balanced by sediment deposition, termed autosuspension (Fig. 2.1C, D) (Pantin, 1979). Here, turbulence within the flow is strong enough to keep particles in suspension, and counteracts their settling velocity (Parker, 1982). However, unlike ignition, there is no net gain of sediment from the bed, as the bed is too hard to erode (Fig. 2.1C), or sediment erosion balances sediment deposition during autosuspension (Fig. 2.1D). Flows that balance erosion and deposition will tend towards spatially uniform velocities, assuming that seabed gradient and flow width do not change markedly. Self-acceleration due to ignition is unlikely to continue indefinitely: increased sediment concentrations will eventually damp the turbulence that keeps sediment aloft (Baas et al., 2009) and shield the bed from rapid erosion, or increase frictional drag and thus reduce flow velocities. However, there is considerable debate over what happens after ignition ceases (Fig. 2.1A). Do flows reach a state of autosuspension; and if so, what do autosuspending flows look like? In particular, do flows develop a dense near-bed layer that drives the event (as proposed by e.g. Winterwerp (2006)), or remain an entirely dilute and fully turbulent suspension (e.g. Cantero et al., 2012)?

Turbidity currents are notoriously difficult to monitor in action, due to their location, episodic occurrence, and ability to damage instruments in their path (Inman et al., 1976, Talling et al., 2013). Consequently, there are very few direct measurements from oceanic turbidity currents, ensuring fundamental theories on how turbidity currents work are poorly tested. Multiple, high temporal resolution velocity measurements along a flow path are required to test how flow state evolves over distance. In particular, ignition and autosuspension have been difficult to reproduce in laboratory experiments (Southard and Mackintosh, 1981). This may be because most laboratory experiments are relatively slow moving, compared to full-scale oceanic flows, and thus have limited ability to erode their substrate, or fully support sediment with realistic grain sizes. Experimental flows thus tend to dissipate. Sequeiros et al. (2009, 2018) successfully produced self-accelerating turbidity currents in relatively slow moving (< 20 cm s^{-1}) laboratory experiments with low density particles, but they did not reproduce fully realistic processes of seabed erosion. However, new

technologies have recently led to major advances in monitoring of active turbidity currents (Hughes Clarke, 2016). This includes acoustic Doppler current profilers (ADCPs) that measure velocity profiles to within a few meters of the seafloor (Xu, 2010). Here we use ADCP and other sensor data to observe spatial patterns of flow ignition, dissipation, and autosuspension in unprecedented detail; and to study how flows work in general.

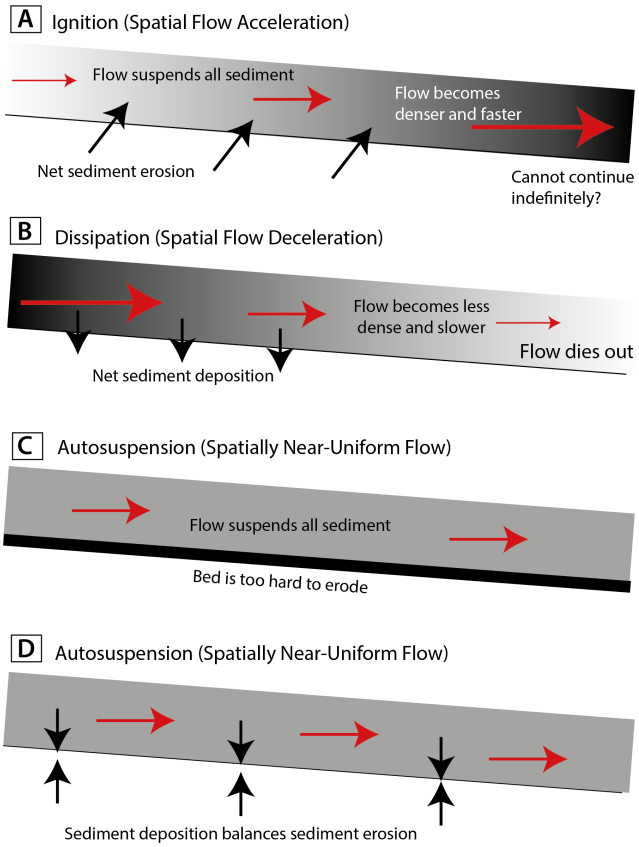

FIGURE 2.1: Ignition, dissipation and autosuspension of turbidity currents. (A) Ignition is caused by net sediment erosion that increases flow density, causing increased velocities. This positive feedback cannot continue indefinitely, as elevated sediment concentrations eventually damp turbulence, shield the bed from erosion, or increase friction. (B) Dissipation is caused by sediment deposition, which leads to spatial decreases in flow density, and thus velocity. This negative feedback causes the flow to eventually die out. (C and D) Autosuspension comprises a situation in which flow density remains constant, and flow velocities are spatially uniform. (C) Flow may be powerful enough to suspend all of the sediment it carries, but the substrate is too hard to erode. Alternatively, localised areas of erosion and deposition may also balance each other out, leading to no net change in suspended sediment. (D) Sediment deposition may be balanced by an equal amount of substrate erosion. Models for autosuspension in (C) and (D) assume flow is dilute and fully turbulent. We subsequently present an alternative model for autosuspension (Fig. 2.7), where flow is driven by a dense near-bed layer.

This study analyses the most detailed (7 locations at sub-minute intervals) field

measurements yet from oceanic turbidity currents, which include the fastest (up to 7.2 cm s^{-1}) flows captured via moored instruments. These measurements come from the upper 52 km of Monterey Canyon, offshore California (Fig. 2.2A) (Paull et al., 2018). Previous direct monitoring of turbidity currents has typically involved measurements at a relatively small number ($\leq$3) of locations along their pathway, which provides limited information on how flows behave (Khripounoff et al., 2009, Liu et al., 2012, Azpiroz-Zabala et al., 2017). By having measurements in seven locations along a turbidity current pathway we are able to determine how flows evolve. Here we focus on changes in the average flow front velocities between measurement locations (termed transit velocities), maximum internal velocities, as well as duration of flow velocities in each event (as measured by ADCPs).

2.2.1 Aims

The first aim is to document changes in turbidity current velocity and runout distance, and hence flow behaviour. What is the observed pattern of ignition, autosuspension and dissipation; and do multiple flows show a consistent pattern of behaviour? The second aim is to understand what causes these patterns of flow behaviour. In particular, we consider how two factors (initial velocity and substrate erodibility) affect flow behaviour, and how near-uniform flow (autosuspension) may follow ignition. Our third aim is to determine if broadly similar flow behaviour is seen elsewhere, although suitable field data are sparse. Our fourth aim is to compare these field observations to most widely accepted theories for ignition and autosuspension. To what extent do these new field data provide a test of past theories? Finally, we develop a new generalised model for how turbidity currents in submarine canyons floored by loose sand operate, which better explains these novel field observations.

2.2.2 Terminology

Turbidity current is used here as a general term for all types of submarine sediment density flow. *Dense flow* signifies sediment concentrations that are high enough to damp turbulence significantly, such that turbulence is no longer the main support mechanism, whilst *dilute flow* is fully turbulent. There is no single threshold value for sediment concentration at which turbulence is strongly damped, as this depends on multiple factors including flow velocity, sediment mineralogy and grain-size. But dilute flows typically have sediment concentrations of $\ll$ 1 %, whilst dense flows might often contain $>$ 10 % sediment by volume. *Diverging* behaviour denotes how

small changes in initial flow velocity are linked to large changes in subsequent runout distance. It does not imply that flow behaviour is bimodal, and intermediate runout lengths can still occur.

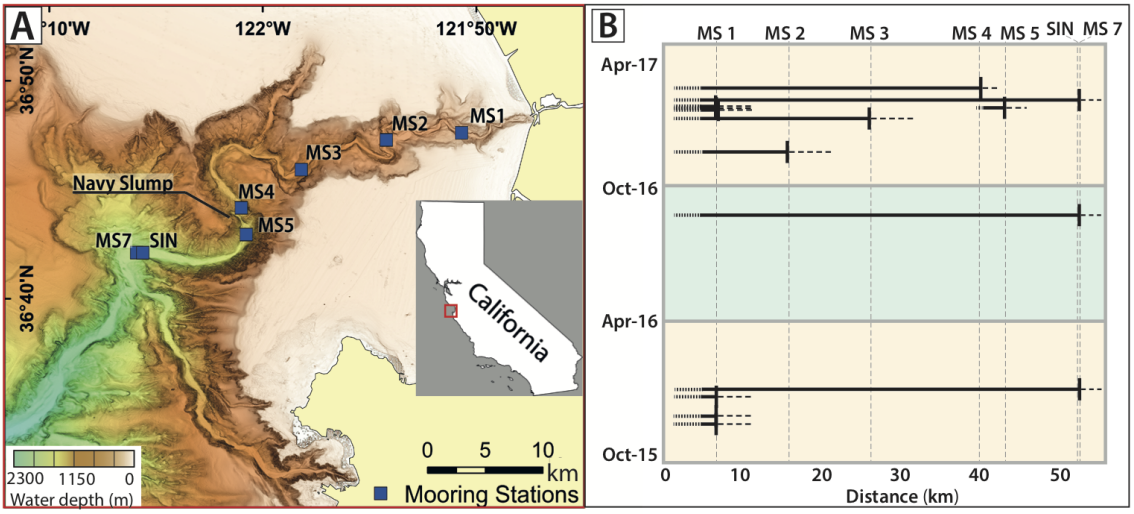

FIGURE 2.2: Location, runout distances and velocities of turbidity currents in Monterey Canyon. (A) Bathymetry map of Monterey Canyon showing location of moorings in this study (MS1 to MS7, SIN), and Navy Slump. (B) Timing and runout distance of turbidity currents in Monterey Canyon between October 2015 and April 2017. Horizontal lines show 13 events registered by ADCPs. The green and yellow boxes show the 6-month deployment periods. Locations of moorings (MS1 to MS7, SIN) are indicated. The exact point where flows terminate between moorings is uncertain.

2.3 Material and Methods

The Coordinated Canyon Experiment (CCE) monitored the upper 50 km of Monterey Canyon (California, USA) to water depths of 1850 m, and consisted of three consecutive 6-month deployments from 2015 to 2017 (Fig. 2.2) (Paull et al., 2018). Sand is primarily delivered to the canyon head via longshore drift, with little river input (Paull et al., 2005). The entire canyon-channel system extends for over 300 km, but flows that runout for over 60 km, to a water depth of 2,850 m, only occur every few hundred years (Stevens et al., 2014). Flows are confined, and experience a constant seafloor gradient and width in the upper part of Monterey Canyon (Fig. 2.3). Up to 2100 m water depth the Monterey Canyon has a sinuosity of 1.9 (Paull et al., 2011). The canyon briefly narrows at a constriction between 1300 and 1400 m water depth, called the Navy Slump (Figs. 2.2 and 2.3) (Paull et al., 2011). This study uses data recorded by ADCPs along the canyon thalweg (Fig. 2.2), which

were part of a larger instrumental array (Supplementary fig. 2.9) (Paull et al., 2018).

2.3.1 ADCP measurements

ADCPs documented velocity profiles through the turbidity currents (Fig. 2.3; Supplementary fig. 2.9), although they are typically unable to make measurements within a few meters of the bed. The shallowest five mooring stations (MS1 to MS5), and the deepest mooring station (MS7), had downward-looking 300 kHz ADCPs located approximately 65 m above the seafloor (Paull et al., 2018). ADCPs on these moorings recorded velocity profiles with 7 pings at 30 second intervals, with 1m vertical bins. A Seafloor Instrument Node (SIN) was located between MS5 and MS7, which contained three separate upward-looking ADCPs recording at 10 second intervals, using acoustic sources with three different frequencies (300, 600, 1200 kHz). No reliable ADCP measurements of current velocity are available from the shallowest mooring (MS1) for some flows, as this mooring broke loose on January 15, 2016 (Paull et al., 2018).

2.3.2 Maximum flow velocity measured by ADCPs

Determining the maximum reliable velocity measured by the ADCP is not straightforward. The arrival of an event is accompanied by mooring tilt and high near-bed sediment concentrations, influencing the ability of ADCPs to accurately record velocities (Paull et al., 2018). Side-lobe interference may compromise some ADCP measurements within 1-3 m of the seabed (Teledyne, 2011), although this depends on the relative strength of backscatter from side-lobe areas and sediment in the flow. We thus adopted a consistent procedure for calculating maximum ADCP-measured velocities, which excludes the 20 highest values during an event. This allows for similar treatment between short and long duration flows. The overall trend of internal velocities remains the same, and therefore our ADCP data processing does not change this paper's main conclusions.

2.3.3 Transit velocities and runout distance

Flow arrival times at the 6 ADCP moorings and SIN were used to measure transit velocities, which are average front velocities across distances between 0.5 km and 15 km (Fig. 2.3A). Arrival times are based on 30 second (or 10 second for SIN)

recording interval of the ADCPs, corrected for clock drift. Distances between sensors were measured along the canyon thalweg, based on a 15 m bathymetric grid. It is assumed that flows principally followed the thalweg (Fig. 2.2A). Flow front, frontal, and transit velocities are used interchangeably throughout this chapter.

2.3.4 Duration of powerful flow measured by ADCPs

As frontal or maximum velocities only tell part of how flow is evolving, and changes in velocity structure, the duration of a fast-moving flow was also quantified and presented (Table 2.1; Supplementary fig. 2.12). This duration, determined for three different velocity thresholds, provides an additional indication of how flows may lengthen or stretch over time. These velocity thresholds were determined by creating contourlines at the 1, 2 and 3 m s^{-1} velocity thresholds. These were especially useful for determining the end of a flow, as this is usually not very distinct (unlike the sudden onset start of a flow), and was also used for approximating flow height.

2.3.5 Canyon topography

Seafloor gradient is determined along the canyon thalweg (Fig. 2.3B), using an average of 10 grid-cells, with a 15 m resolution. Canyon width is defined using the area of active bedforms (Paull et al., 2018), and measured every 200 m down the canyon. The canyon floor is delimited by steep canyon walls with slopes of ∼10 to 45°.

2.3.6 Grain sizes

Sediment traps were mounted at 10 meters above the seafloor on the moorings (MS1-MS5, MS7; Supplementary fig. 2.9). They were tilted and brought closer to the bed by the initial powerful stages of some flows. Grain sizes in sediment traps from the upper canyon (MS1, MS2, and MS3) were used for most events. For the September 1st event, MS3 and MS4 are used, as the event ignited farther down in the canyon. Laser particle grain-size measurements were taken from sediment trap subsamples at every 1 or 5 cm intervals (Maier et al., 2019). Discs released automatically into the traps at 8-day intervals provided time markers. Supplementary fig. 2.13 shows grain-size distribution for the flow events, including mean grain sizes used for Fig. 2.6.

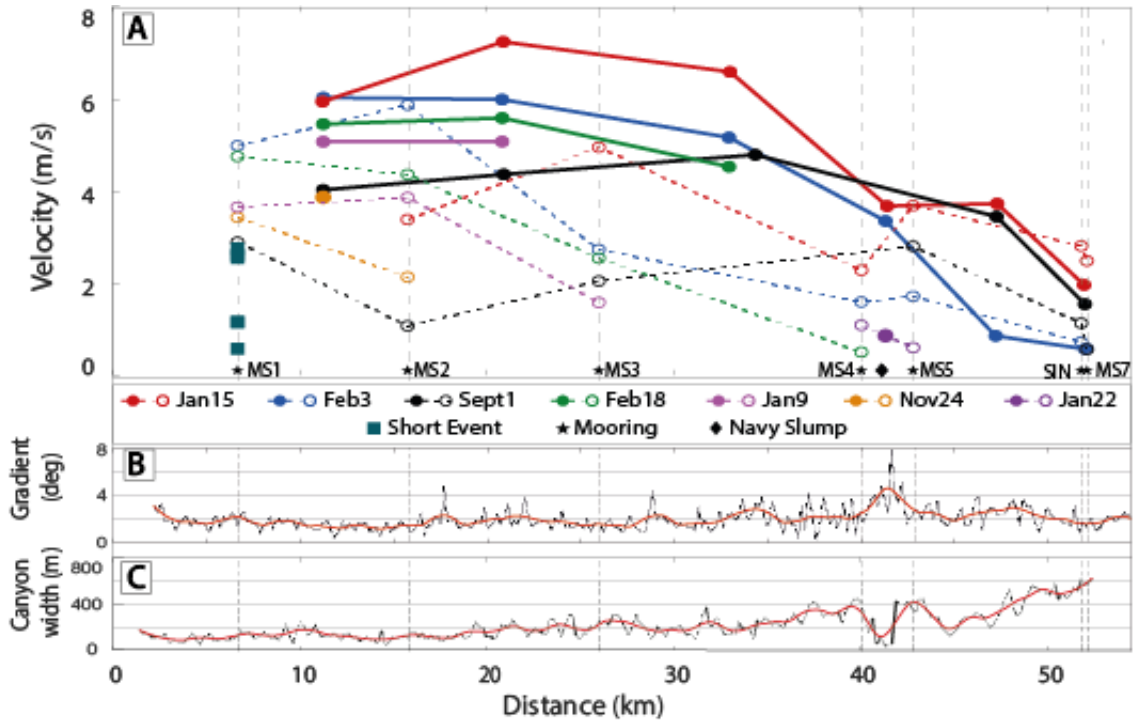

FIGURE 2.3: Velocities of turbidity currents in Monterey Canyon and properties of the thalweg. (A) Changes in flow velocity with distance along Monterey Canyon's thalweg. Solid dots and solid lines show frontal velocities between moorings. Open symbols and dotted lines show maximum internal velocity measured at each mooring by an ADCP, including for some flows that only reached the first mooring (solid squares). (B) Changes in thalweg gradient, including 10 grid cell average in red. (C) Changes in axial channel width, defined by the width of mapped bedforms, including 10 grid cell average in red.

2.4 Results

The entire sensor array in Monterey Canyon recorded 15 flows (Paull et al., 2018). Here we consider only the 13 flows measured using the moored ADCP array (Fig. 2.2B; Supplementary figs. 2.9 and 2.10), as we rely on ADCP measurements. Twelve of these 13 ADCP-measured flows started in the upper canyon at water depths of $<$ 300 m. Flows were measured first by ADCPs at Mooring Station (MS) 1, located 6.7 km from the canyon head (Figs. 2.2A and 2.3A). Many flows then rapidly dissipated, including six flows that died out entirely before MS2, which is 9 km downstream of MS1 (Fig. 2.3A). Of the seven flows measured at multiple moorings, three flows terminated within the sensor array. One event occurred only in the mid-canyon, between MS4 and MS5. Three further flows swept through the entire sensor array, running out for over 50 km from the canyon head, although they had very different velocities and durations at the final sensor site (Fig. 2.4). Most (12 of 13) flows were initiated during the winter months (Fig. 2.2B), during which time storm waves are

most pronounced and are thought to be important for flow initiation (Paull et al., 2018). Only one event occurred in the summer months. This event on September 1st 2016 did not coincide with large wave heights, a river flood, or earthquake, suggesting another, as yet poorly understood, trigger (Paull et al., 2018).

Transit velocities are available for the seven flows that reached multiple moorings (Fig. 2.3A). The transit velocities between the first two moorings (MS1 and MS2) have broadly similar values of between 4 and 6 m s^{-1}. The runout length of these flows varied greatly, with large increases in runout length correlating with only slightly faster initial frontal velocity (Fig. 2.3A). However, one event recorded during the CCE experiment showed a different trend, and it was the only event occurring outside the winter months, on September 1st (Fig. 2.2B). This event started with a comparatively low initial frontal velocity between MS1 and MS2 of $\sim$4 m s^{-1}, identical to the initial frontal velocity of the November 24th event (Fig. 2.3A) (Paull et al., 2018). However, the November 24th event failed to reach MS3; whilst the September 1st event accelerated between MS3 and MS5, and reached the end of the instrument array (Fig. 2.3A).

The maximum ADCP velocities measured within flows occurred within the first 10 minutes of the flow front arrival (Fig. 2.10). These internal velocities show a broadly similar pattern to the transit velocities (Fig. 2.3A). Flows with slower maximum ADCP-measured velocities at the first mooring tended to die out abruptly in the upper canyon, whilst events with faster ADCP-measured velocities ran out for much longer distances (Fig. 2.3A). Note that ADCP measurements define six shorter runout events that are only recorded at one mooring, and thus lack transit velocity data. Furthermore, for the internal maximum ADCP velocities, the emphasis is on the velocity trend. The absolute internal velocities are likely to be lower than expected, due to data limitations. ADCP measurements at the base and front of the flow are complicated, as the ADCP experiences tilting, and data collection is further limited by a blanking zone and sediment saturation. This region however is expected to have the highest velocities. For the post-processing of the ADCP data high maximum values are excluded, necessary due to data artefacts, but can also potentially include genuine high velocity measurements.

Flow behaviour is only partly captured by transit and maximum ADCP measured velocities. For example, modest increases in transit velocity are often associated with more prolonged periods of powerful flow (Fig. 2.4, Table 2.1). As a powerful (fast and dense, following (Paull et al., 2018)) flow is more efficient in entraining substrate, the duration of powerful flow is important for ignition or autosuspension. Flows tend

to stretch, as the frontal part of the flow runs ahead from the slower moving body and tail (Fig. 2.4) (Azpiroz-Zabala et al., 2017). Overall, long run-out events occurring in winter tended to significantly stretch, such that they extended for almost the entire length of the instrument array. Shorter winter events, based on data from the shorter winter event on November 24th, are initially $\lesssim$10 km in length as the event arrives at MS2, but die out in the upper-canyon. The long runout event in September was initially weak, but became much more prolonged and faster mid-canyon, as well as increasing its transit velocity, before dissipating rapidly between MS5 and MS7 (Fig. 2.4). Most flows started with a flow front thickness <10m, based on the flow height according to the velocity threshold contourlines. The long run-out events in winter developed thicknesses >30 m (Fig. 2.4) (Paull et al., 2018).

TABLE 2.1: Flow duration (in minutes) for each mooring station and event. For each event, a threshold flow velocity was set to determine the duration of the flow at each mooring. The ADCP data was displayed using contour lines corresponding to each threshold, allowing for determination of flow duration at every mooring. Left hand columns denote flow velocity threshold $\geq$ 1 m s^{-1}. Middle columns denote flow velocity threshold $\geq$ 2 m s^{-1}. The right-hand column denotes flow velocity threshold $\geq$ 3 m s^{-1}. Where no flow duration is given, there was no ADCP measurement (January 15, MS1, and September 1, MS4). A duration of 0 min indicates the flow is no longer measured at the specified threshold velocity at that mooring.

Flow Threshold	**≥ 1 m/s**							**≥ 2 m/s**							**≥ 3 m/s**						
Mooring	MS1	MS2	MS3	MS4	MS5	SIN	MS7	MS1	MS2	MS3	MS4	MS5	SIN	MS7	MS1	MS2	MS3	MS4	MS5	SIN	MS7
Distance (km)	6.7	16	26.0	40.0	43	51.8	52	6.7	16	26.0	40.0	43	51.8	52	6.7	16	26.0	40.0	43	51.8	52
Jan-15		87	141	182	213	112	89		9.5	59	23	41	37	22		8.5	30	0	25	0.5	0
Sep-01	20	3.5	73		22	45	0	1	0.5	7	0	11	0	0	0.5	0	0	0	3	0	0
Feb-03	48	74	73	67	65	0	0	28	17	26	0	3.5	0	0	16	15	2.5	0	0	0	0
Feb-18	34	26	70	0				15	12	16					7.5	8	1.5				
Jan-09	35	23	43					19	11	0					11	8	0				
Nov-24	33	15						12	3.5						9	0.5					
Jan-21	31							9.5							2						
Jan-20	25							7							2.5						
Dec-01	16							7							3						
Jan-23	9							0							0						
Jan-06	6.5							1							0						
Dec-11	2.5							0							0						
Jan-22				37	0						0	0						0	0		

2.5 Discussion

2.5.1 Is there a consistent pattern of behaviour for turbidity currents?

Eleven of the twelve flows show a broadly consistent pattern of runout behaviour, which can be based on the initial transit velocity between the first two moorings, and the maximum ADCP-measured velocities at the first mooring (Fig. 2.3A). Flows with the fastest initial velocities tend to run out further. However, small changes in initial transit velocities, or maximum ADCP-measured velocities, lead to much larger changes in runout distance and subsequent flow velocity. Runout distances are thus highly sensitive to initial velocities, leading to diverging flow behaviour (Fig. 2.3A). All flows initially accelerate, and the initially fastest flows have near-uniform transit velocities for several tens of kilometres and can stretch up to 35 km in length (Fig. 2.4). Flows with slightly slower ($\sim$0.5 m s^{-1}) initial transit velocities, or maximum ADCP-measured velocities, die out mid-canyon. The six slowest moving flows at MS1 terminate before reaching MS2 (Fig. 2.3A). These flows that die out in the upper or mid-canyon are initially powerful, and can sometimes carry heavy (800 kg) objects, or move moorings down-canyon, at velocities of $\geq$4 m s^{-1}, but their power does not persist for several kilometres. Only the fastest flows at the first mooring maintain their velocity for longer distances, and lengthen significantly. The single exception to this general pattern of behaviour (Figs. 2.3A and 2.4C) occurred on September 1st 2016. This flow's transit velocity and maximum ADCP-measured velocity increased in the mid-canyon (Fig. 2.3A), and the duration of powerful flow lengthened markedly (Fig. 2.4C).

These field data thus provide new insights into where and how flows ignite, dissipate or autosuspend. The most powerful flow (Jan 15) shows ignition between MS1 to MS3, followed by dissipation based on the transit velocities. A notable observation is that three of the four most powerful flows at MS1 have near-uniform transit velocities for $\sim$20-35 km, from MS1 to MS3; and near-uniform maximum internal (ADCP-measured) velocities from MS1 to MS2 (Fig. 2.3A). This suggests that an initial phase of acceleration (ignition) up-canyon of MS1 is followed by near-uniform flow velocities (autosuspension), at least near the flow front. Transit velocities are averages over substantial distances, and internal (ADCP-measured) velocities come from a few specific locations. Thus, it is likely that flow velocities show greater localized variability than depicted in Fig. 2.3A. However, available field data indicate near-uniform transit velocities (autosuspension) over substantial distances.

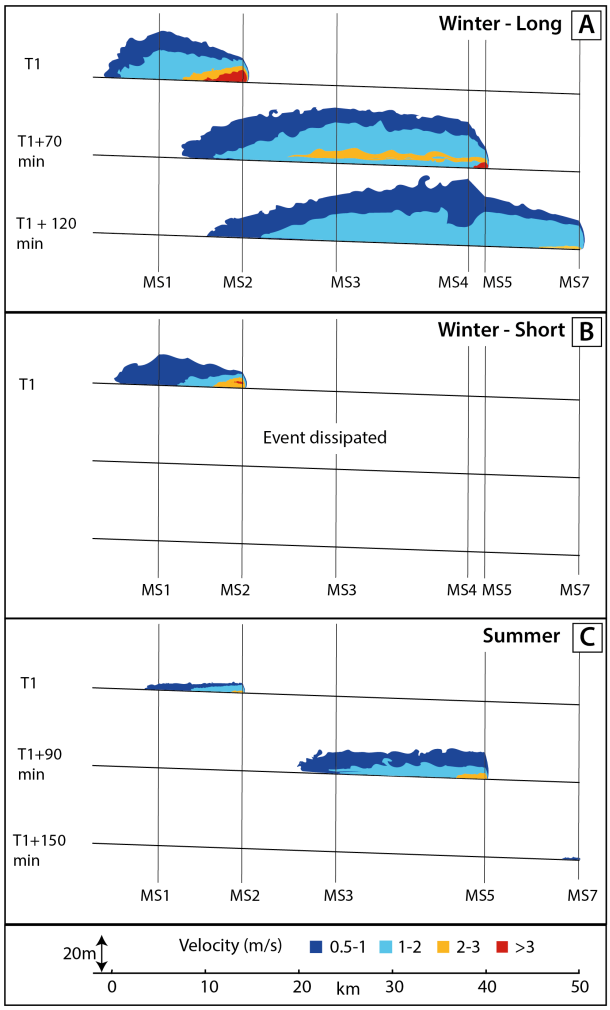

FIGURE 2.4: Turbidity current structure at consecutive snap-shots in time, showing changes in flow length, internal velocity structure, and flow thickness. Flow velocities between moorings are inferred, as are velocities in the lower 3-4 m of the flow (due to ADCP side-lobe interference). Flow thickness is based on the height where the velocity is lower than 0.5 m s^{-1}. The figure combines data at moorings (locations indicated) and personal interpretation on flow structure between moorings (A) Long runout flow, which is initially fast, based primarily on the January 15th event. The MS1 mooring was dragged down-canyon during the January 15th event. Thus, ADCP data from the February 3rd event are used for MS1 in the T1 snapshot, and it is unknown if the 15th January flow was present at MS1 during the T1+70 min snapshot. (B) Shorter runout flow that was initially powerful, but then dissipated rapidly, based on the November 24th event. This event carried an 800 kg object at $\geq$ 4 m s^{-1}, for $\sim$1 km in the upper canyon (Paull et al., 2018). (C) Example of an initially weak turbidity current on September 1st, which then accelerated markedly in the mid-canyon, and dissipated rapidly between MS5 and MS7. This is the only event that occurred during summer months (Fig. 2.2B).

2.5.2 What factors control turbidity current behaviour?

We now seek to understand what controls these patterns of flow behaviour. Twelve flows accelerated rapidly from rest within the upper 6.7 km of the canyon, reaching

velocities of at least 3 to 6 m s^{-1} at MS1 (Fig. 2.2). These turbidity currents were most likely generated by seabed failure, typically during storm events, as sediment plumes from rivers are weak or absent (Paull et al., 2018). An initial phase of acceleration will partly result from gravitational acceleration of the failed mass, but it may also indicate that flows eroded the seabed and self-accelerated (ignited). However, the relative importance of simple gravitational acceleration of an initial failure, and ignitive self-acceleration via subsequent seabed erosion, is uncertain due to a lack of repeat bathymetric surveys with high enough frequency upstream of MS1.

Beyond MS1, small ($<$ 0.5-1 m s^{-1}) increases in initial transit or maximum ADCP-measured velocities are associated with profound differences in subsequent flow behaviour (Fig. 2.3A). We thus infer that initial velocities in the upper canyon determine later flow behaviour. Flows with only fractionally higher initial transit velocities, or maximum internal ADCP-measured velocities, tend to run out for much greater distances (Fig. 2.3A; Table 2.1). This strongly diverging flow behaviour is not due to changes in seafloor gradient or canyon width, as canyon axial channel width ($\sim$200 m) and gradient ($\sim 2^{\circ}$) are relatively uniform from MS1 to MS3 (2.3B and C), and all of these flows experienced similar changes in canyon slope and width. However, the axial channel widens significantly beyond MS3 (from $\sim$200 to $\sim$600 m), which may explain why most flows consistently decelerate beyond MS3 and MS4 (Fig. 2.3A).

The September 1st event is anomalous, as it was initially slow moving but its transit velocity then increased mid-canyon (Fig. 2.3A), and the duration of powerful flow velocities increased (Fig. 2.4; Table 2.1). This acceleration is not related to steepening or narrowing of the canyon, and cannot be explained by a 'tail wind' from internal tides. Internal tides can be directed up or down-canyon; and if internal tides are directed down-canyon, this could increase the velocity of flows. This is not the case here (Supplementary Fig. 2.11). This flow was also the only event to occur in summer (Fig. 2.2B). One hypothesis is that self-acceleration of the September 1st event resulted from entrainment of a surficial-mud layer, deposited during less-stormy summer months. Surficial-mud layers that are 1-12 cm thick occur in the La Jolla Canyon, located south of Monterey Canyon on the same margin (Paull et al., 2013). Mud layers in cores from MS7 in Monterey Canyon are 1-3 cm thick, with modal grain sizes of $\sim$50-80 μm (Fig. 8 of Maier et al. (2019)). However, it is not clear whether surficial-mud layers are better developed during summer months, as information from repeat coring during different seasons is lacking. Moreover, strong (50-80 cm s^{-1}) internal tides in Monterey Canyon rework canyon floor mud throughout the year (Maier et al., 2019). An alternative hypothesis for mid-canyon ignition of the September 1st event is triggering of a local substrate failure between MS2 and MS3,

forming a knickpoint. Such knickpoints are observed in several places on the canyon floor, and they have been termed 'master head scarps' in past work (Paull et al., 2010b). However, we also lack suitably detailed time-lapse seabed surveys from the mid-canyon to determine whether a local knickpoint failure occurred.

2.5.3 Do submarine flows in other locations show similar behaviour?

Having determined that there is a consistent pattern of flow behaviour in Monterey Canyon, albeit with one exception, we now seek to understand if similar behaviour occurs elsewhere, and is thus of more wider and general applicability. There are few other locations worldwide where the transit or internal velocities of oceanic turbidity currents have been measured at more than 4 locations along the flow pathway. Indeed, we are aware of only 3 such datasets (Fig 2.5).

One of these field datasets comes from cable breaks along Gaoping Canyon, offshore Taiwan, which (unlike Monterey Canyon) is fed by a major river mouth (Fig. 2.5B) (Gavey et al., 2017). Seabed gradients along Gaoping Canyon (0.3°-1.0°; Gavey et al. (2017)) are somewhat lower than Monterey Canyon (1.6°- 2.3°; Paull et al. (2011)) (Fig. 2.5). Transit velocities in Gaoping Canyon are nearly constant for ∼100 km, suggesting that the turbidity currents reach a near-uniform equilibrium state. This pattern of uniform flow front velocities (autosuspension) is thus not specific to Monterey Canyon, and it may persist over even longer distances.

A second data set comes from a turbidity current that broke submarine cables offshore from the Grand Banks, Newfoundland, in 1929 (Heezen and Ewing, 1952, Piper et al., 1988). The turbidity current resulted from extensive but thin (average 5 m) failures on the continental slope, with ∼ 185 km^3 of sediment deposited on the Sohm Abyssal Plain (Piper and Aksu, 1987, Piper et al., 1988). These failures progressively entrained seawater and evolved into debris flows, and then turbidity currents which then merged into one turbidity current (Piper et al., 1999). Flow was confined initially within multiple valleys for the first 500 km of the pathway (Hughes Clarke et al., 1990), where it reached a transit velocity of 19 m s^{-1} on a gradient of ∼0.5° (Hughes Clarke, 1988). This initial phase of the flow eroded the seabed, and may have ignited, although the available data cannot constrain this. Transit velocities then decreased to 6.2 m s^{-1} on gradients of ∼0.15 to 0.05°, as flow became poorly confined, and spread to become several hundred kilometres wide (Fig. 2.5C; Heezen and Ewing (1952), Hughes Clarke (1988), Hughes Clarke et al. (1990), Piper and

Hundert (2002)). Its transit velocity continuously decreased with distance during these later stages, showing how reduction in confinement can control flow behaviour, leading to dissipation.

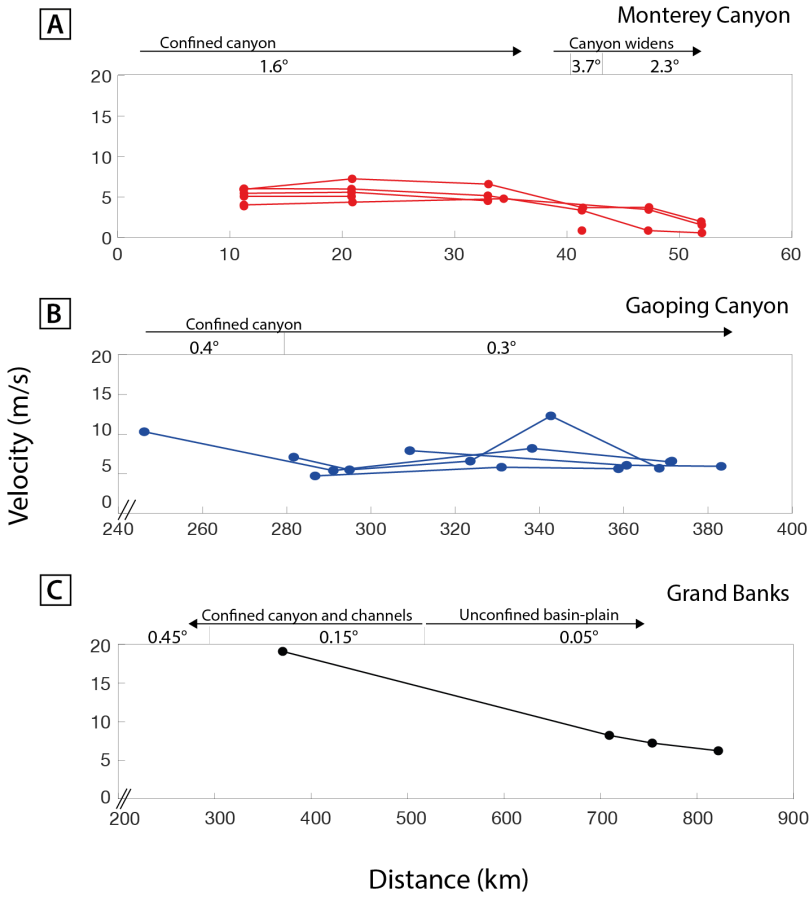

FIGURE 2.5: Changes in frontal velocities of turbidity currents over distance. Variations in seabed gradient and flow confinement are also shown. (A) Frontal velocities of flows in Monterey Canyon. Fig. 2.3B, C shows detailed changes in seabed gradient and channel floor width. (B) Frontal velocities of flows confined within Gaoping Canyon, offshore Taiwan, based on cable breaks (Gavey et al., 2017). Average seabed gradients are shown, but detailed surveys of canyon width are currently lacking. (C) Frontal velocities of the Grand Banks turbidity current in 1929, offshore Newfoundland, based on cable breaks (Heezen and Ewing, 1952, Hughes Clarke, 1988, Piper et al., 1999). Distance is from the initial earthquake epicentre, although coincident cable breaks occurred over a wider area. The initial part of this flow was confined by submarine fan-valleys, but was unconfined during its later stages, as it spread across a basin plain (Piper et al., 1999). Detailed data on the seafloor gradient over the entire length of the event are lacking, but are based on Stevenson et al. (2018) and Piper and Hundert (2002).

2.5.4 Comparison of field data to previous theory of autosuspension and ignition

We now compare our new field observations to previous influential theory that predicts when a submarine turbidity current will autosuspend or ignite (Bagnold, 1962, Pantin, 1979, Parker, 1982, Parker et al., 1986). It is important to understand whether these unusually detailed field observations can provide a robust test of such theories.

2.5.4.1 Initial energy-balance theory

Initial work (Bagnold, 1962, Pantin, 1979, Parker, 1982) formulated a theory for whether turbidity currents autosuspend or ignite that is based on energy losses and gains by the flow. It was assumed that movement of sediment down-slope results in loss of potential energy, whilst energy is expended by processes that keep sediment grains aloft. When energy gains equal or exceed energy losses, the flow can carry all of the sediment it suspends. Then, if the flow can also erode loose sediment from the bed, it ignites (Fig. 2.1). However, if no erodible material is available, the flow autosuspends. Alternatively, if energy losses exceed energy gains, then some of the suspended sediment will settle out, and the flow will eventually dissipate.

Equation 2.1 and figure 2.6 result from this initial energy-balance theory (Bagnold, 1962, Pantin, 1979, Parker, 1982), as previously depicted by Sequeiros et al. (2009). Figure 2.6 predicts the threshold frontal velocity (u_h) for ignition, as a function of sediment settling velocity (W_s) and seafloor gradient (β). The threshold constant for ignition to occur (ϵ), varies between different authors. Bagnold (1962) and Parker (1982) assumed that potential energy gain must at least equal or exceed energy losses ($\epsilon \leq 1$). In contrast, Pantin (1979) assumed that only a small fraction ($\epsilon \leq 0.01$) of potential energy gain will be available to keep sediment aloft, with most potential energy being dissipated in other ways.

$$\frac{W_s \cos\beta}{u_h \sin\beta} \leq \epsilon \begin{cases} \epsilon = 0.01 & \text{Pantin, 1979} \\ \epsilon = 1 & \text{Parker, 1982} \\ \epsilon = cos\beta & \text{Bagnold, 1962} \end{cases} \tag{2.1}$$

As we use the flow front velocity (u_h) to calculate the threshold for ignition, we only consider whether ignition or autosuspension occurs near the flow front. As noted by past authors (e.g. Bagnold, 1962, Pantin, 1979, Parker, 1982, Sequeiros et al., 2009), Equation 2.1 is a necessary condition for ignition, but it is not a sufficient condition

for ignition; indeed it is rather conservative (Parker et al., 1986). Suitable sediment must also be available for erosion and incorporation into the flow. This might not be the case, for example, if the flow was moving over hard bedrock.

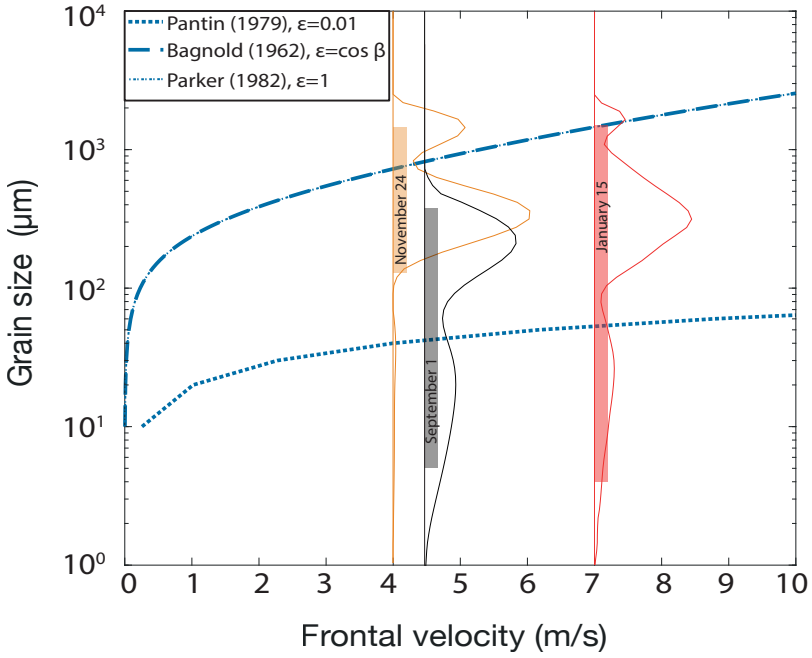

FIGURE 2.6: Comparison of field measurements in Monterey Canyon to past energy-balance theory for autosuspension, following Sequeiros et al. (2009). The figure illustrates the challenge of testing theory using field data, such as which grain size to use from a flow with a wide grain size range. Blue lines show the different threshold constants (ϵ in Equation 2.1) used by different authors, assuming a seabed gradient of 2°. Autosuspension occurs below the lines. If seabed sediment is available for erosion, the flow will also ignite. Note that results for the threshold constant of Bagnold (1962) coincide with those of Parker (1982) for the case of Monterey Canyon. Field measurements of three events (November 24th, September 1st, and January 15th) in Monterey Canyon are shown. Each flow is displayed along the x-axis according to their maximum frontal velocity. Each event shows the measured grain-size distributions, based on sediment traps located 10 m above the bed. The grain-size distributions shown here are averages for each event in sediment traps from the upper canyon where flows are assumed to ignite (see text, Supplementary Fig. 2.13 for more information). The coloured boxes show the 10^{th} percentile (D10) and 90^{th} percentile (D90) of the coarsest grain-size samples in traps from each event. The grainsize range for each event is given, as it is unknown which grainsize is most representative in the monodisperse approach of the theory (see subsection 2.5.5).

Measurements from Monterey Canyon can be combined with Equation 2.1 to compare observed and predicted flow velocities associated with ignition (Fig. 2.6). We use a seabed gradient of 2° (Fig. 2.1E) (Paull et al., 2018), and sediment traps on moorings for grain-size distributions for three separate turbidity currents. The sediment trap closest to the location of ignition in that flow is used (Fig. 2.1C). For January 15,

samples from MS2 and MS3 are used because the MS1 sediment trap at 10 meters above the seafloor was ripped off the mooring. For the September 1st event this grain-size curve is based on samples from MS3 and MS4, closest to the point of ignition. November 24th grain-size distribution is based on samples from MS1. These traps were initially suspended 10 m above the bed, but they were sometimes dragged closer to the bed during the first few minutes of flow (Paull et al., 2018). The maximum observed frontal velocities are used. The method of Ferguson and Church (2004) is used to estimate settling velocities for individual grains, which assumes that flow is dilute. Settling velocities could become hindered at higher sediment concentrations.

Figure 2.6 shows transit (average frontal) velocities needed for ignition for the grain sizes captured by traps in the Monterey Canyon flows, for different values of ϵ that have been proposed previously. There is reasonable agreement between our field observations with the approach of both Parker (1982), and Bagnold (1962). The three displayed flows that ignited in Monterey Canyon, show that their observed grain sizes in sediment traps mainly lie within the field of ignition (Fig. 2.6). Thus, these flows are likely to ignite according to theory, and are observed to do so. There is poorer agreement with Pantin (1979), suggesting that potential energy losses do not need to be 100 times greater than energy losses to keep sediment aloft, and thus for ignition to occur.

2.5.4.2 Subsequent more complex turbulence energy-balance theory

The simple energy-balance approach summarized by equation 2.1 (Bagnold, 1962, Pantin, 1979, Parker, 1982) sets out a necessary condition for autosuspension or ignition. However, flows that fulfil equation 2.1 need not ignite, as other conditions are also important. For example, sediment exchange with the seabed will strongly influence flow density and thus velocity (Parker et al., 1986, Traer et al., 2012), whilst entrainment of surrounding water will cause momentum to be lost (Parker et al., 1986).

Parker et al. (1986) therefore subsequently developed a more advanced and complete theory. This theory initially comprised three layer-averaged equations based on budgets of fluid (water) mass, sediment mass and momentum within the flow (Parker et al., 1986). A fourth layer-averaged equation was then based on budgets of turbulent kinetic energy within the flow, including turbulence production at the upper and lower flow boundary, dissipation of turbulence due to viscosity, and work done by turbulence against vertical density gradients (Parker et al., 1986). This approach led

to a more complex criterion for ignition (equation 16 of Parker et al. (1986)). This criterion involves layer-averaged sediment concentration, flow velocity and thickness, sediment settling velocity, bed shear velocity, and rates of sediment and water entrainment (Parker et al., 1986). This more advanced but complex criterion for ignition implicitly assumes that sediment is mainly supported by fluid turbulence. It would not apply to denser sediment flows in which turbulence is strongly damped, and where other processes become important for sediment support, such as support via grain-to-grain collisions, or excess pore pressure.

2.5.5 Why past autosuspension and ignition theory is difficult to test

Although unprecedented in their detail, our field observations from Monterey Canyon provide a rather weak test of the applicability initial simpler energy-balance theory (Bagnold, 1962, Pantin, 1979, Parker, 1982), and they are unable to test the more complex turbulent energy-balance (Parker et al., 1986) theory, for three key reasons.

First, both types of theory involve a single sediment settling velocity, and thus require that a representative grain-size is chosen. However, turbidity currents in Monterey Canyon contain a wide range of grain sizes (Fig. 2.6), as is often the case for turbidity currents elsewhere. Thus, there is an issue of which representative grain-size to choose from this wide distribution (Fig. 2.6). There are also major issues related to measurement of grain-size in the field via sediment traps, as traps only sample grain-size at a single height, and traps may be less effective at capturing finer grains than coarser grains.

Second, in the case of theory based on turbulent kinetic energy budgets (Parker et al., 1986), we lack sufficiently precise measurements of key parameters needed by this theory, most notably layer-averaged sediment concentrations, but also rates of sediment and water entrainment.

Finally, and most importantly, some key assumption that underpin past theories may not hold. For example, Parker's later theory based on turbulent kinetic energy budgets assumes that flow is dilute, such that turbulence is always the main support mechanism (Parker et al., 1986). Field evidence suggests that some turbidity currents in Monterey Canyon are driven by dense near-bed layers with high ($> 10\%$ by volume) sediment concentrations (Fig. 2.6) (Paull et al., 2018). These dense layers are needed to explain the fast ($\geq$4 m s^{-1}) movement of very heavy (up to 800 kg) objects for several kilometres (Paull et al., 2018). It is unlikely that entirely dilute

flows could carry such heavy objects, at high velocities, for such distances; the heavy objects are instead entombed in a dense near-bed layer (Paull et al., 2018). Turbulence is damped strongly in such dense near-bed layers, and settling will be hindered (Winterwerp, 2006). Other sediment support mechanisms become important, such as grain collisions or excess pore pressures that partly carry the sediment load. The more advanced ignition theory (Parker et al., 1986) would thus be unable to capture the behaviour of flows in Monterey Canyon with dense near-bed layers.

2.5.6 New travelling wave model

We now outline a new conceptual model for how initially fast moving turbidity currents operate in confined settings, underlain by loose sand, based on our field observations. Following Paull et al. (2018), this model includes dense near-bed layers that drive the flow, in which turbulence is not the main support mechanism. The model thus better fits detailed field observations from Monterey Canyon. A new model is needed because past theory for ignition and autosuspension (Parker et al., 1986) was not formulated to include dense near-bed layers. The new model differs from past work (e.g. Paull et al., 2018), as it explains how flows that initially ignite may then autosuspend, as they reach a uniform transit velocity.

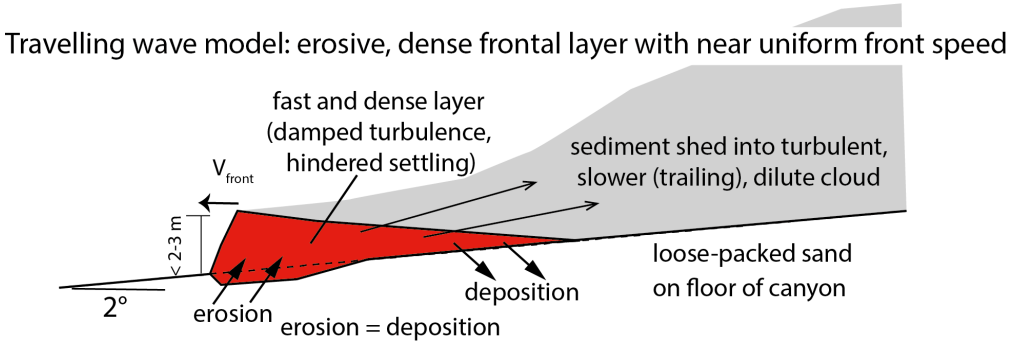

FIGURE 2.7: New travelling wave model. Travelling wave model for turbidity current behaviour in loose-sand submarine canyons, in which flows contain a fast and dense near-bed layer at their front, as proposed by Paull et al. (2018). Erosion at the front of this dense near-bed layer is balanced by sediment deposition from its rear, leading to uniform transit velocity and autosuspension. Sediment is shed backwards to form a trailing sediment cloud that is dilute and fully turbulent, which lengthens over time.

We propose that during initial ignition, and the following near-equilibrium (autosuspension) phase, a fast and dense near-bed layer exists at the flow front, which drives the overall event, similar to Fig. 2.7 (Winterwerp, 2006). This dense near-bed layer near the flow front maintains an approximately uniform frontal velocity, as erosion

of the bed near its front, is balanced by deposition at its rear (Fig. 2.7). Thus, although the dense layer is locally either erosive or depositional at a single location, erosion and deposition are balanced over the whole of the layer, such that the dense layer velocity is near-uniform. This leads to autosuspension (Fig. 2.7). However, unlike previously proposed autosuspension theory (shown in Fig. 2.1), here there is a lateral change in flow density whilst the flow is in autosuspension. We envisage that sediment concentrations in the dense layer (10-30%) are those attributed by Winterwerp et al. (1992) to hyperconcentrated flow, which is capable of forming the crescentic shaped bedforms seen along the floor of Monterey Canyon (Winterwerp et al., 1992, Paull et al., 2018). It has been suggested that liquefied flows of sand could only travel for short distances (Lowe, 1976) on steep slopes (>3°) due to rapid dissipation of excess pore fluid pressures and basal sedimentation. However, addition of small fractions of cohesive mud, as seen in Monterey Canyon (Maier et al., 2019), increase the time taken for excess pore pressure to dissipate by orders of magnitude and hinders settling (Iverson et al., 2010), thus greatly increasing runout of partly-liquefied flow. Sediment from the dense layer is shed backwards into a dilute and fully turbulent sediment cloud. This trailing cloud increases in length (stretches) as the dense flow front runs ahead of the trailing body (Figs. 2.4 and 2.7) (Azpiroz-Zabala et al., 2017).

We term this new model the 'travelling wave model', and it is broadly comparable to behaviour seen in laboratory experiments involving dense, dry granular avalanches (Supplementary fig. 2.14) (Pouliquen and Forterre, 2002, Mangeney et al., 2007). A key feature of these experiments is that the dry avalanches that are fast enough can erode their underlying substrate, in their case loose sand. These dry granular avalanche experiments show two types of behaviour (Pouliquen and Forterre, 2002, Mangeney et al., 2007). Slower moving avalanches dissipate, as they fail to erode and entrain their substrate. However, sufficiently fast moving dry granular avalanches erode, and form a travelling wave with near-uniform frontal transit velocities (Supplementary fig. 2.14) (Pouliquen and Forterre, 2002, Mangeney et al., 2007, Edwards and Gray, 2015). Erosion of sand from near the front of the travelling wave is balanced by deposition from its rear (Fig. 2.7). The avalanche thus contains a substantial fraction of locally eroded material. The transit velocity of this travelling wave is strongly determined by the thickness of the frontal avalanche, as in the dry granular experiments (Pouliquen and Forterre, 2002, Mangeney et al., 2007). Frontal thickness determines the down-slope driving force near the front, at least for near-uniform gradients and flow densities. The flow thickness in turn depends on the depth of eroded material, and thus on rates of frontal erosion (Pouliquen and Forterre, 2002,

Mangeney et al., 2007). A key requirement is fully water saturated substrate, which is the case for Monterey Canyon (Paull et al., 2018). Liquefaction is necessary for substrate remobilization and to reduce basal friction, thereby preserving downslope momentum (Iverson, 2012). Turbidity currents will differ in key regards from these dry granular avalanches that occur on far steeper ($> 30°$) gradients. For example, erosion of water-saturated canyon floor sediment, such as via abrupt loading and liquefaction, may allow turbidity currents to erode on much lower ($< 2°$) gradients than dry granular avalanches. Settling velocities will be much greater in air, and turbidity currents can also comprise trailing dilute suspensions. However, we draw a first-order analogy with the ability of faster moving dry granular avalanches that exceed a threshold and erode their substrate, whilst depositing from their rear, and thus maintain dense flow with near-uniform transit velocity.

This new travelling wave model also needs to account for crescent shaped bedforms that are abundant along the floor of Monterey Canyon (Paull et al., 2018), and many other sandy submarine canyons (Symons et al., 2016), which have been linked to instabilities (termed cyclic steps) in supercritical flows (Hughes Clarke, 2016). Bedforms in Monterey Canyon have amplitudes of 1 to 3 m, and wavelengths of 20 to 80 m (Paull et al., 2018). As discussed in more detail by Paull et al. (2018), tracking of extremely heavy (800 kg) objects showed that they experienced repeated vertical oscillations of 1-3 m, as they were carried down Monterey Canyon at velocities of $\sim$4 m s^{-1}. Bedforms were thus most likely continuously present, and must have been at least partly formed by the dense travelling wave. This is consistent with field observations and laboratory experiments showing that cyclic steps and up-slope migrating bedforms can form beneath supercritical flows with very high (20-40% volume) sediment concentrations (Winterwerp et al., 1990, 1992) as well as dilute supercritical flows (Kostic and Parker, 2006, Covault et al., 2017). Future work is now needed to test this new travelling wave model, such as via direct measurements of sediment concentration in turbidity currents, or by determining the importance of locally derived or far-travelled sediment in near-bed layers.

2.6 Conclusions

Here we analyse the most detailed measurements yet from within seafloor turbidity currents, showing how their transit and maximum measured internal velocities vary with distance.

Overall, we observed that small (< 0.5-1 m s^{-1}) increases in average transit velocities

are associated with large differences in subsequent runout (Fig. 2.8). Fractional increases in initial velocities may lead to flows with near-uniform velocities associated with autosuspension, enabling much longer runout. Flows with only slightly lower initial velocities die out in upper or mid-canyon. Patterns of transit and internal velocities with distance thus diverge markedly (Fig. 2.8).

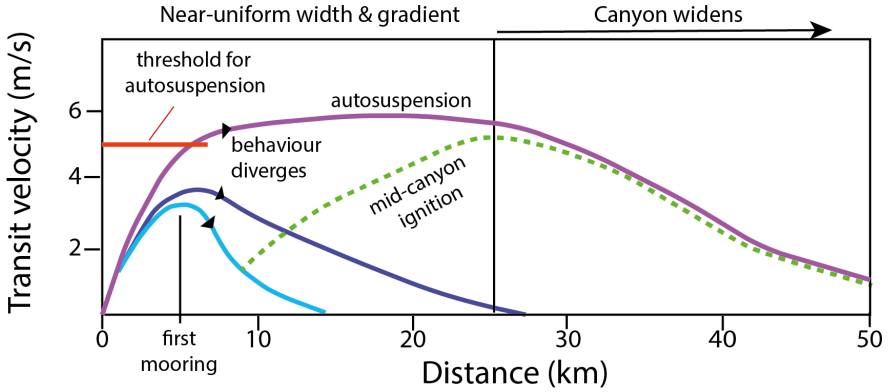

FIGURE 2.8: Summarising model for turbidity current behaviour in submarine canyons underlain by loose sand. Patterns of flow behaviour, based on frontal transit velocities that are simplified from Fig. 2.3A. Small increases in transit velocity at the first mooring are associated with major differences in subsequent flow velocities and runout distance, causing divergence in flow behaviour (purple, dark blue and light blue lines). However, flows can sometimes self-accelerate and ignite within the mid-canyon (green dotted line), due to changes in substrate strength and erodibility, or potentially knickpoint failure. There is a threshold initial transit velocity (red line) above which flows can autosuspend (purple line).

However, one flow in Monterey Canyon is an exception to this general pattern, as it self-accelerated mid-canyon (Fig. 2.8, dotted green line). It is also the only flow that occurred during less-stormy summer months. Erosion of a weak surficial-mud layer with underlying fine sand, is likely to also favour self-acceleration. Turbidity current behaviour may therefore be highly sensitive to both initial transit velocities and substrate character.

Our observations show that initial self-acceleration (ignition) can be followed by a phase of near-uniform transit velocities (autosuspension), at least for initially faster flow events (Fig. 2.8). Previous models have proposed that autosuspension may follow on from ignition, as erodible bed material runs out. But this is not the case in Monterey Canyon, as loose sand is available along the canyon floor. Instead, we propose that flows are driven by thin and dense, frontal, near-bed layers (which we call a travelling wave; Fig. 2.7). Faster moving travelling waves can reach an autosuspending state, as frontal erosion balances deposition from their rear, so that near-uniform frontal flow thicknesses and thus velocities are maintained. These

dense travelling waves shed a slower moving dilute sediment cloud, which lengthens as the flow runs out. But this dilute cloud does not drive the flow, and changes in its sediment concentration are thus less important. This travelling wave model itself needs further testing, including via direct measurements of near-bed sediment concentrations, but it is consistent with movement of very heavy objects at high velocity near the flow front (Paull et al., 2018).

2.7 Acknowledgements

C.J. Heerema is funded by the European Union's Horizon 2020 research and innovation program under the Marie Skłodowska-Curie grant agreement No. 721403 - ITN SLATE. This project received funding from the David and Lucile Packard Foundation, Natural Environment Research Council (grant NE/K011480/1, NE/M007138/1, NE/M017540/1, NE/P009190/1, and NE/P005780/1), U.S. Geological Survey (USGS) Coastal and Marine Program, and Ocean University of China. M.A. Clare acknowledges support from NERC National Capability project Climate Linked Atlantic Sector Science (NE/R015953/1). E. Pope was supported by a Leverhulme Trust Early Career Fellowship (ECF-2018-267).

2.8 Supplementary Material

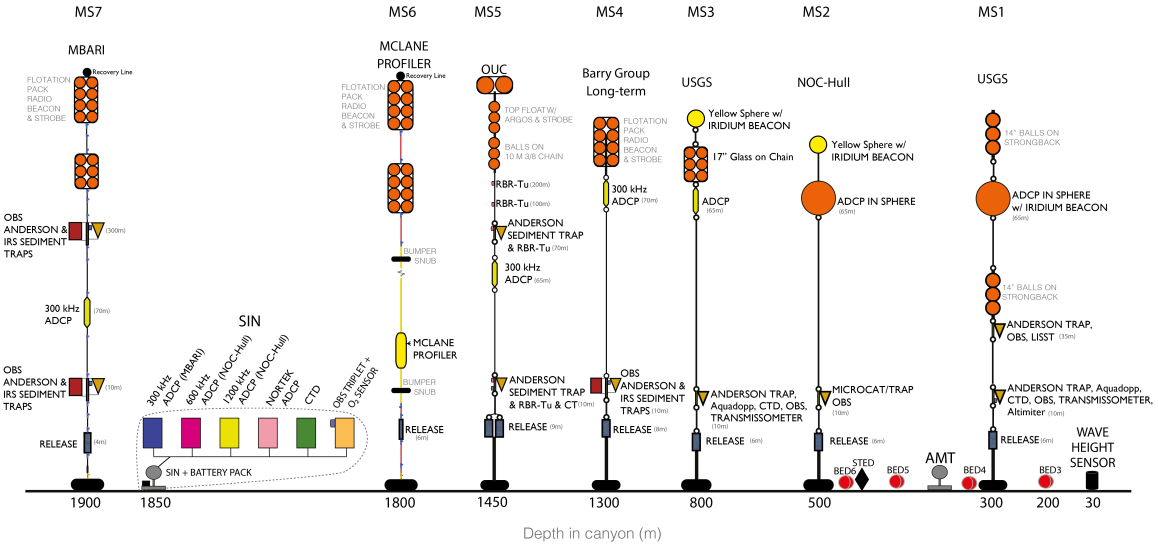

FIGURE 2.9: All instruments deployed in Monterey Canyon between October 2015 and April 2017 (after Paull et al. (2018)). For this study, the velocity measurements from ADCPs are considered, and sediment traps are used for grain-size analysis. Therefore, MS1-5, Seafloor Instrument Node (SIN) and MS7 are of importance. The 300 kHz ADCPs on the mooring stations were looking down, and recorded at 30s time intervals, and 1m vertical intervals. The SIN had 3 ADCPs looking up, and recorded at 10s time intervals. For a more detailed description of other instruments deployed, see Paull et al. (2018).

FIGURE 2.10 *(next page)*: Time series of ADCP measured velocity for each turbidity current in Monterey Canyon, at each mooring. Contour lines are at set velocity intervals. Vertical columns show the same mooring, whilst each horizontal row is a different flow event. Velocities <0.5 m s^{-1} are excluded. In each plot, the top left corner notes the maximum ADCP-measured velocity, which excluded the 20 highest ADCP measurements. All plots show velocity profiles measured 5 minutes before, and 40 minutes, after initial arrival of the turbidity current. 300 kHZ ADCP frequencies were used, facing downwards at the mooring stations and upward at the SIN (see Suppl. Fig. 2.9). For the September 1st event, 600 kHz frequency was used at the SIN, as the 300 kHz frequency ADCP was not available. For clarity, only 3 (out of 6) of the shorter events only measured at MS1 are displayed, and the event occurring between MS4 and MS5 is not displayed.

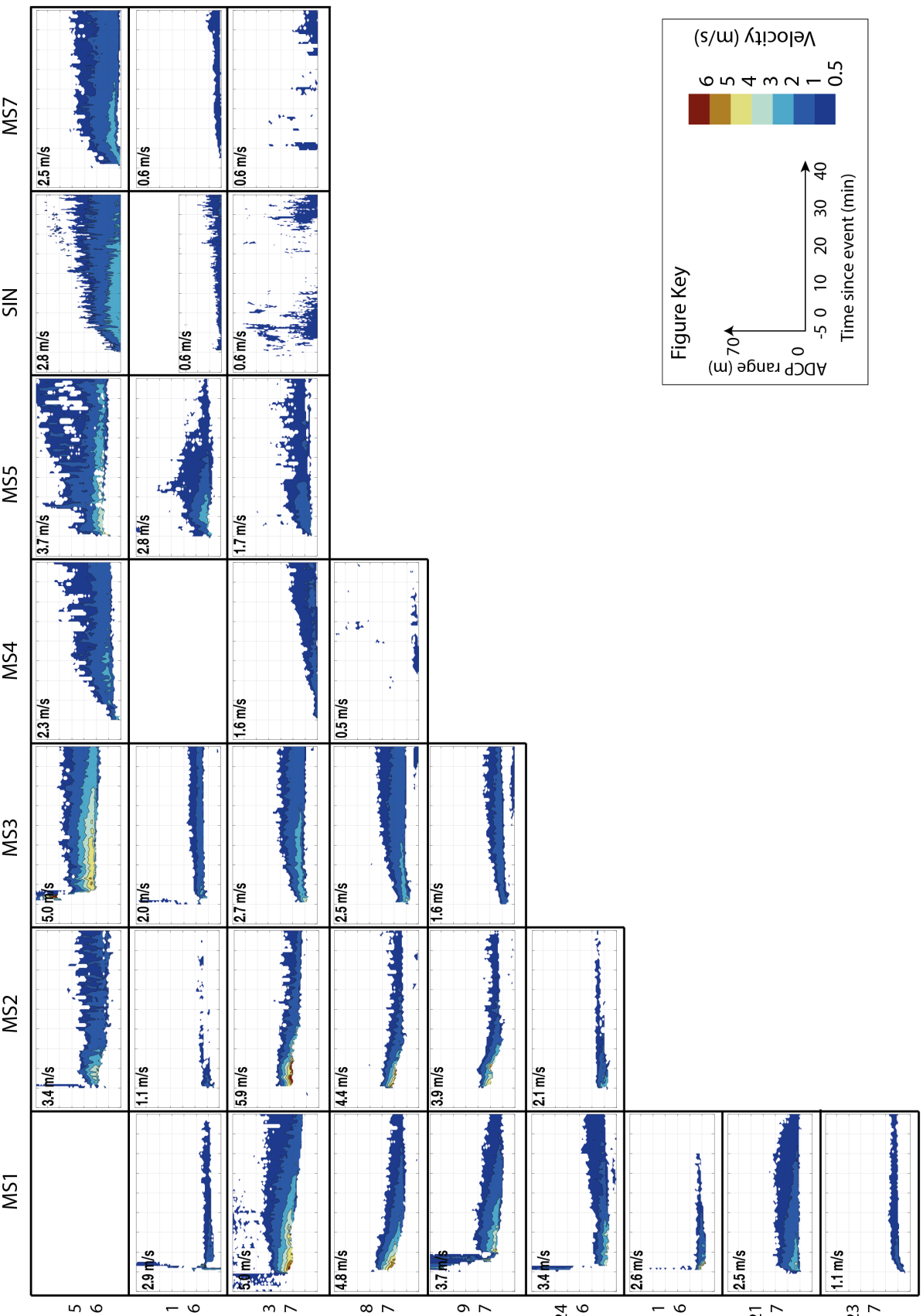
MS1
MS2
MS3
MS4
MS5
SIN
MS7
January 15 2016
September 1 2016
February 3 2017
February 18 2017
January 9 2017
November 24 2016
December 1 2016
January 21 2017
January 23 2017
Figure Key
Velocity (m/s)
6
5
4
3
2
1
0.5
ADCP range (m)
0
70
-5 0 10 20 30 40
Time since event (min)

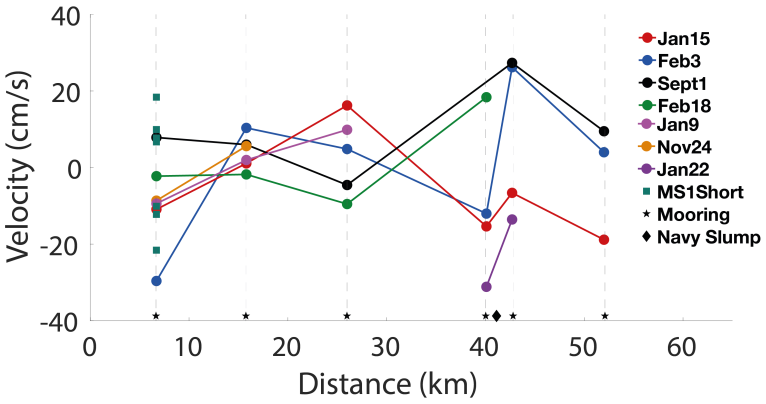

FIGURE 2.11: Variation in the velocity of internal tides in Monterey Canyon during turbidity current events. Negative values show flow direction down-canyon. The tidal velocities are based on ten minute averages of ADCP measurements immediately before flow arrival. The key for events corresponds to that in Fig. 2.3A, which plots changes in frontal and internal (ADCP measured) velocities for the same events. Frontal and maximum internal flow velocities are consistently much higher than these tidal velocities, suggesting that internal tides had limited effects of on flow ignition or dissipation.

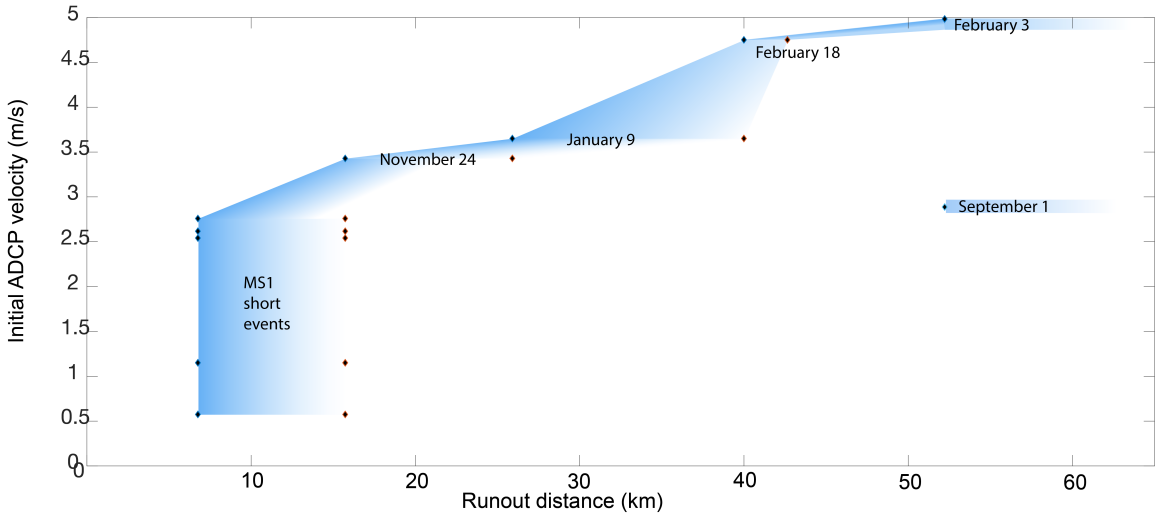

FIGURE 2.12: Relationship between initial ADCP velocity (at MS1) and runout distance of flows in Monterey Canyon. The runout distance shows the possible range for a flow to have dissipated. A flow will have ceased to exist between the last mooring a flow was recorded by an ADCP (blue diamonds), or the subsequent mooring where there was no event seen (red diamonds). The September 1st event does not fit the trend of increasing initial velocity corresponding to increasing runout distance. February 3rd and September 1st event have no end mooring, as they ran out past the last ADCP in the canyon. January 15th and January 22nd events are excluded, as they do not have measurements at MS1.

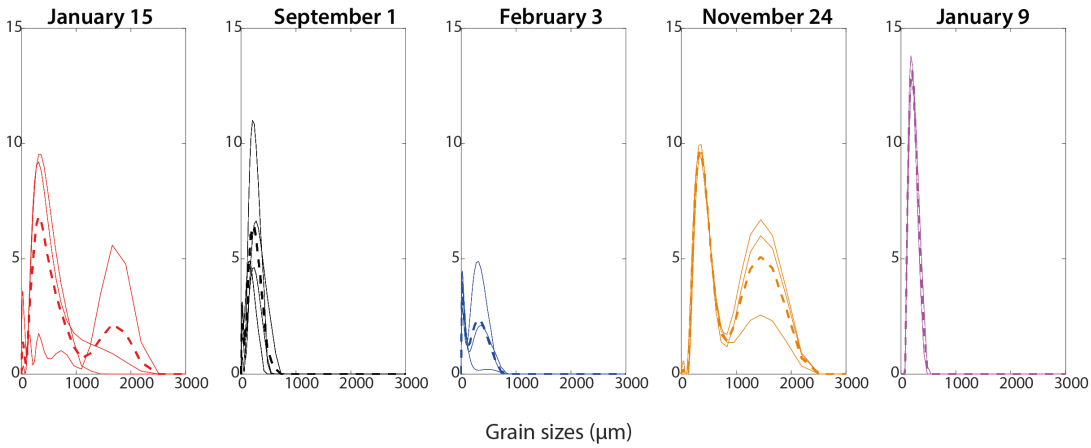

FIGURE 2.13: Grain-size distributions of events with run-out lengths that extended past MS1. The Anderson sediment traps located near the point of ignition in the canyon are used. The traps were located approximately 10m above seafloor, but they were likely tilted and dragged closer to the seafloor at the beginning of the events. For January 15, samples from MS2 and MS3 are used because the MS1 sediment trap at 10 meters above the seafloor was ripped off the mooring. For the September 1st event this grain-size curve is based on samples from MS3 and MS4, closest to the point of ignition. November 24th grain-size distribution is based on samples from MS1. The February 3rd grain-size distribution uses samples from MS3. For the events on January 9th and February 18th, there was no data available from MS1 or MS2, where the flow would be igniting and are therefore not included. By using ADCP data and intervalometer discs automatically dropped in the trap every eight days, sediment trap samples can be related to a specific event. Depending on the sediment thickness of an event within the trap 2 - 4 laser particle grain-size distribution measurements are available per event (solid lines). These measurements are in turn averaged, leading to one representative grain-size distribution per event (dashed lines).

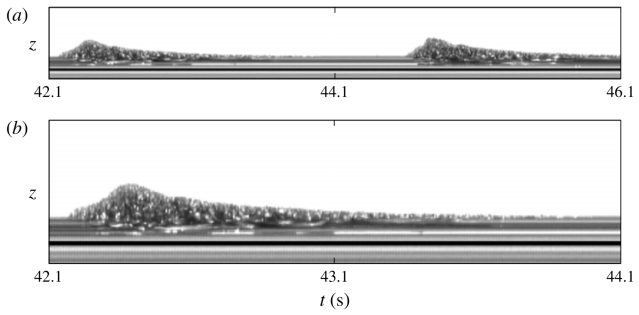

FIGURE 2.14: Examples of travelling waves in dry granular flows as seen in laboratory experiments (Edwards and Gray, 2015). In small-scale laboratory experiments, steadily travelling waves have been reproduced, eroding the static layer in front and depositing grains to the back. In Edwards and Gray (2015), this is referred to as granular erosion-deposition waves. If the waves travel at constant velocity, the erosion-deposition process is found to be in equilibrium.

Chapter 3

Can you identify the trigger of a flow from its velocity signature?

This chapter has been submitted to *Journal of Sedimentary Research*: **Heerema CJ**, Cartigny MJ, Silva Jacinto R, Simmons, SM, Apprioual R, Talling PJ. 'How distinctive are flood-triggered turbidity currents?'

Kate Heerema was responsible for the data analysis, conceptualisation, visualisation and writing the paper. MJBC provided key comments on this chapter, and SMS provided key resources to convert sediment concentrations. This chapter would not have been possible without the data collected by co-authors from IFREMER. Data analysis at IFREMER provided key opportunities for the post-processing. The main author would like to acknowledge the fruitful discussions and invaluable input from the co-authors and their patience during the revision process.

3.1 Abstract

Turbidity currents triggered at river mouths form an important highway for sediment, organic carbon and nutrients to the deep sea. Consequently, it has been proposed that the deposits of these flood-triggered turbidity currents provide important long-term records of past river floods, continental erosion and climate. Various depositional models have been suggested to identify river flood-triggered turbidite deposits, which are mainly based on the assumption that a characteristic velocity structure of the flood-triggered turbidity current is preserved as a recognizable vertical grain-size trend in their deposits. Four different criteria have been proposed to identify the

velocity structure of flood-triggered turbidity currents: prolonged flow duration, a gradual increase in velocity, cyclicity of velocity magnitude, and a low peak velocity. However, very few direct observations of flood-triggered turbidity currents exist to test these proposed velocity structures. Here we present direct measurements from the Var Canyon, offshore Nice in the Mediterranean Sea. An acoustic Doppler current profiler was located 6 km offshore from the river mouth, and provided detailed velocity measurements that can be directly linked to the state of the river. Another mooring, positioned 16 km offshore, showed how this velocity structure evolved down-canyon. Three turbidity currents were measured at these moorings, two of which are associated with river floods. The third event was not linked to a river flood and was most likely triggered by a seabed slope failure. The multi-pulsed and prolonged velocity structure of all three (flood and landslide triggered) events is similar at the first mooring, suggesting it may not be diagnostic of flood triggering. Indeed, the event that was most likely triggered by a slope failure suited the four flood-triggered criteria best, as it had prolonged duration, cyclicity, low velocity and a gradual onset. Hence, previously assumed velocity structure criteria used to identify flood-triggered turbidity currents may be reproduced by other triggers. Next, this study shows how the proximal multi-pulsed velocity structure re-organizes down-canyon to produce a single velocity pulse. Such rapid-onset, single-pulse, velocity structure has previously been linked to landslide-triggered events. Amalgamation of multiple velocity pulses thus leads to shredding of the flood signal, so that the original initiation mechanism is no longer discernible at just 16 km from the river mouth. Recognizing flood-triggered turbidity currents and their deposits may thus be challenging, as similar velocity structures can be formed by different triggers, and this proximal velocity structure can rapidly be lost due to self-organization of the turbidity current.

3.2 Introduction

Rivers directly connected to submarine channels are highly efficient in transporting large amounts of sediment, organic carbon and pollutants to the deep-sea (Galy et al., 2007). Consequently, the deep-sea depositional records from flood-triggered turbidity currents have been used to reconstruct paleo-floods (e.g. St-Onge et al. (2004), Plink-Björklund and Steel (2004); see review of Zavala et al. (2011) and references therein) and their recurrence rates (Mulder and Alexander, 2001, Nakajima, 2006). Such paleo-flood reconstructions rely on the underpinning assumptions that river floods create turbidity currents with a distinct velocity structure, and that

this distinct velocity structure is recorded in the turbidite deposits through unique grain-size variations (Mulder et al., 2003). It is assumed that this vertical grainsize trend translates to an identifiable velocity time series at a spatial point, from here on referred to as velocity structure. Previously suggested criteria to identify the velocity structure of a flood-triggered turbidity current include: 1) a prolonged duration due to the long time scale of river flooding in comparison to slope failure (Mulder et al., 2003, Zavala and Pan, 2018); 2) a gradual velocity increase at the start of the turbidity current (waxing) associated to the rising limb of the river discharge, followed by a waning turbidity current (Mulder et al., 2003); 3) multiple cycles of acceleration and deceleration (pulses) reflecting discharge fluctuations that are common within a single river flood (Khripounoff et al., 2012, Zavala and Pan, 2018); and 4) a low peak velocity, as flood-triggered turbidity currents are expected to be dilute and thus slow in comparison to the much denser landslide-triggered flows (Mulder et al., 2003, Nakajima, 2006, Khripounoff et al., 2012, Zavala and Pan, 2018). These four criteria are important in paleo-flood reconstructions as they are used to distinguish between flood-triggered and landslide-triggered turbidity currents, with landslide-triggered flows characterized by a sudden onset with a high peak frontal velocity (Kneller and Buckee, 2000, Mulder et al., 2003). However, there are few field observations of velocity structures within turbidity currents measured offshore river mouths to validate such an approach. To our knowledge, there are just four locations with direct measurements of such velocity structures (Khripounoff et al., 2009, 2012, Liu et al., 2012, Hughes Clarke, 2016, Lintern et al., 2016, Hage et al., 2019).

The velocity structures measured at these four locations of flood-triggered turbidity currents are not always consistent with the above-mentioned criteria. For example, observations in the Var Canyon have shown that landslide-triggered events can last twice as long as flood-triggered events (Khripounoff et al., 2012). A gradual increase in velocity was measured in a flood-triggered turbidity current in the Gaoping Canyon (Liu et al., 2012), but not in the flood-triggered flows in the Var Canyon (Khripounoff et al., 2012), on the Fraser Delta (Lintern et al., 2016), nor at the Squamish Delta (Hughes Clarke, 2016, Hage et al., 2019). Although multiple cycles of acceleration and deceleration are observed in the Var Canyon (Khripounoff et al., 2012), they have not been observed in any of the other events (Liu et al., 2012, Hughes Clarke, 2016, Lintern et al., 2016, Hage et al., 2019). Finally, the Var Canyon observations show that flood-triggered flows are indeed somewhat slower than landslide-triggered flows (Khripounoff et al., 2012), but in the Gaoping Canyon the observations show opposite velocity trends, as turbidity currents linked to river floods are the fastest (Gavey et al., 2017). Moreover, the turbidity currents observed in some river-associated systems

strongly resemble landslide-triggered flows with a single pulse characterized by a sudden onset (Hughes Clarke, 2016, Lintern et al., 2016, Hage et al., 2019). Overall, the variability in the direct observations show that using the velocity structure of a turbidity current to identify a flood trigger is not straightforward and more field measurements are needed to understand these variations.

Several mechanisms could explain the inconsistencies observed in the velocity structures of flood-triggered turbidity currents. For example, the duration of a turbidity current can change significantly down canyon due to stretching of the flow (Azpiroz-Zabala et al., 2017). Initially slow flows can accelerate rapidly as they start to bulk up due to erosion of the seafloor (Hage et al., 2019, Heerema et al., 2020), and multiple velocity pulses within the same event can amalgamate (Ho et al., 2018). Additionally, the velocity structure of flood-triggered turbidity currents is likely to vary significantly depending on the exact process by which the sediment is transferred from the river to the turbidity current. Three such transfer mechanisms have been proposed. First, at sufficiently high sediment concentrations (36-43 kg m^{-3}), excess sediment density causes a river plume to be denser than seawater, leading to a hyperpycnal river that plunges and continues along the seabed as a turbidity current (Mulder et al., 2003). Second, sea-surface (hypopycnal) river plumes can generate turbidity currents. Convective fingers of settling sediment can occur at sediment concentrations in excess of 1 kg m^{-3} (Parsons et al., 2001). Third, substantially more dilute river plumes (0.07 kg m^{-3}) have recently been found capable of initiating turbidity currents, by generating high sediment concentration on the bed due to near-bed flow convergence in tidal settings (Hage et al., 2019). The range of possibilities outlined above, combined with the scarcity of seafloor observations, severely limits paleo-flood reconstructions. High-resolution velocity measurements near the river mouth are needed to test the variability of turbidity currents close to the river mouth. Additionally, further velocity measurements down-canyon are needed to test how far down the system any potential flood-triggered velocity structure is preserved.

3.3 Aims

Here we present new field measurements of three turbidity currents offshore from the Var River mouth. This study extends the earlier work of Khripounoff et al. (2009, 2012) in this system. In this new study, high-resolution acoustic Doppler current profiler (ADCP) measurements of turbidity currents were collected just 6 km offshore from the river mouth. This ADCP mooring deployment is closer to the river

mouth than Khripounoff et al. (2009, 2012), and allows us to monitor the proximal velocity structure of the Var Canyon turbidity currents in unprecedented detail. We use these measurements to test the link between river floods and velocity structure of the turbidity currents. More specifically, we test whether the previously proposed criteria indeed distinguish flood-triggered turbidity currents from other triggers, at locations close to the river mouth. We then use a second mooring further offshore (16 km) to test whether such proximal velocity structure is preserved down-canyon. Finally, we discuss the implications of these findings for reconstructing paleo-flood records from turbidity current deposits.

3.4 Terminology

Confusion can occur if terms are not clearly defined, and terms such as *"hyperpycnal"* have been used by different authors in somewhat different ways (Shanmugam, 2018, Feng, 2019, Zavala, 2019). We therefore specify the terminology used throughout this paper. We define a turbidity current as a gravity driven subaqueous sedimentary density flow, where the dominant particle support is fluid turbulence (Mulder and Alexander, 2001), although turbulence may be damped within near-bed layers that characterize high density turbidity currents (Cantero et al., 2012). We call a turbidity current *"flood-triggered"* if sediment suspended during a river flood (a distinct, sharp, peak in river discharge) directly transfers into the turbidity current. Such direct transfer of flood-derived sediment could occur via two of the earlier mentioned mechanisms: instantaneously via plunging (Mulder et al., 2003) or via concentrated pockets of sediment in convective fingers (Parsons et al., 2001). We reserve the term *"hyperpycnal turbidity currents"* for turbidity currents that are direct continuations of plunging rivers (Talling, 2014). All non-flood triggered turbidity currents occurring in a river-fed submarine channel are here labelled as *"river-associated"* turbidity currents and include flows triggered by tides (Hage et al., 2019) and submarine landslides (Hughes Clarke et al., 2014). More specifically, we use the term *"landslide-triggered"* for surge-like turbidity currents, commonly assumed to be short duration due to non-permanent sediment supply (Mulder and Alexander, 2001), and consisting of a sudden onset with high velocity front and a subsequent waning flow (Kneller and Buckee, 2000).). The term "velocity structure" is used for a time-series of velocity measured at a single spatial point (e.g. mooring). Merging of pulses (distinct velocity peaks) within the velocity time-series is referred to as "amalgamation".

3.5 Study Area

The Var Canyon is located offshore Nice in the Mediterranean Sea, and extends for approximately 20 km before joining with the Paillon Canyon at 1850 m water depth (Fig. 3.1A; Piper and Savoye (1993)). The Var Canyon is a continuation of the Var River and begins directly at the river mouth. The Var River discharge has a yearly cyclicity of enhanced discharge in the spring and summer due to snow melt followed by high intensity rainfall floods separated by low river discharges during the winter (Mulder et al., 1998). The average annual discharge is 50 m^3 s^{-1}, with the bi-annual flood recurrence at 810 m^3 s^{-1} (http://www.hydro.eaufrance.fr).

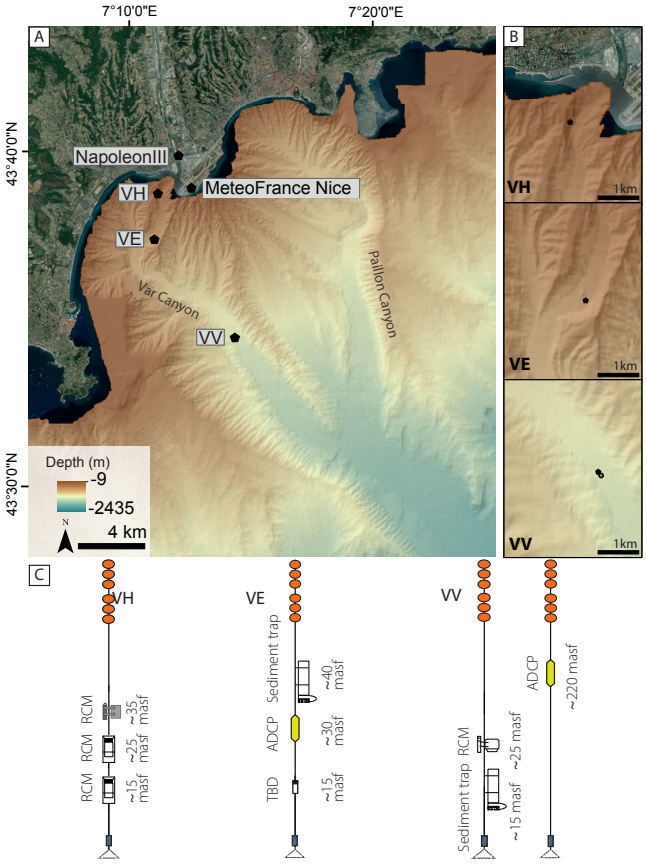

FIGURE 3.1: (A) Overview map of Var Canyon showing locations of three mooring stations (VH, VE and VV), and measurement stations for river discharge (Napoleon III) and meteorological data (MeteoFrance). (B) Detailed bathymetric maps of each mooring station. Note that mooring VH is offset from the canyon axis, and mooring VV moved a small distance during flows. (C) Set-up for each mooring, including both moorings at the VV site. ADCPs measure velocity profiles. RCMs are single-height current meters, and TBD is a turbidity sensor. Height in meters above seafloor (masf) are indicated.

The Var Canyon turbidity current activity is well known from the large landslide-triggered turbidity current that occurred during the construction of Nice Airport in

1979 (Mulder et al., 1997). Khripounoff et al. (2009, 2012) are the only studies in the Var Canyon that used direct velocity measurements of turbidity currents in this system. They found that within the canyon several turbidity currents are initiated each year by either river floods or submarine landslides (Khripounoff et al., 2012). Typical turbidity current velocities are between 20-90 cm s^{-1}, with a duration between 4 and 24 hours, and a flow thickness between 50-130 m (Khripounoff et al., 2009, 2012). In the Var Canyon, flood-triggered turbidity currents are found to have the lowest velocities, shortest duration and highest vertical extent (Table 1 in Khripounoff et al. (2012)).

3.6 Methods

Here we analyze a new dataset from the Var River-Canyon system that was collected during the Solveig III research cruise, from late June 2009 to early February 2010, a period spanning 7 months (Fig. 3.2; Blandin (2010)). We first compare velocity data from a proximal canyon mooring to river discharge measurements, to analyze the relationship between the velocity structure of turbidity currents and associated river discharge. We then use a second mooring to trace the changes in the velocity structure of the turbidity currents down the canyon. Another, third mooring was located directly offshore the river mouth, but was unfortunately misplaced just outside the canyon and consequently did not record any turbidity currents, as explained below.

3.6.1 Land stations

Var River discharges were recorded at the NapoleonIII site (Nice, France; Fig. 3.1A) every 15-minutes (HYDRO `http://www.hydro.eaufrance.fr`). Near Nice Airport, a MeteoFrance weather station recorded hourly maximum wind speeds based on 10-minute average values, as well as precipitation on an hourly basis (Fig. 3.1A).

3.6.2 Var Canyon mooring configuration

Initially three moorings (VH, VV, VE) were deployed within the Var Canyon (Fig. 3.1A, B), where the first mooring (VH) was unfortunately misplaced outside the canyon thalweg. Even though this mooring did not measure any turbidity currents, the mooring set-up and the resulting data are still presented here to provide a complete overview of the observations. However, the observations from mooring VH are

not analyzed in as much detail as those from the other thalweg moorings. Most instruments on the moorings recorded at a 20-minute interval, unless stated otherwise.

Station VH was located on the side wall of the submarine canyon at 121 metres water depth (mwd), and 2.8 km from NapoleonIII measurement station at the river mouth (Fig. 3.1A, B). On this mooring, there was a Seaguard Recording Current Meter (RCM) at 15 metres above the seafloor (masf), an RCM 11 at 25 masf that recorded every 5 minutes, and an Aquadopp RCM at 35 masf recording at 30 min intervals (Fig. 3.1).

Station VE was deployed at 518 mwd, at a location 5.7 km from NapoleonIII (Fig. 3.1A, B). Mooring VE had a turbidity sensor mounted at 15 masf (Fig. 3.1C). A downward-looking 300 kHz acoustic Doppler current profiler (ADCP) was mounted at 30 masf, which recorded over a series of 2 m high bins. Besides the maximum velocity, the velocity at 25 masf is also extracted from the ADCP data to enable a direct comparison between the depth-resolved ADCP data and the single depth point RCM measurements on the other moorings. A sediment trap (PPS 4/3-Technicap) was mounted at 40 masf. Settling particles were collected over a 9-day window using cylindrical sediment traps with a sampling aperture of 0.05 m^2. These traps were covered with a honeycomb baffle with 10 cm deep cells, which were 1 cm in diameter, and were equipped with 24 sampling bottles.

Station VV was located at 1280 mwd, 15.7 km away from the river mouth (Fig. 3.1A, B). Here, the sediment trap was located at 15 masf (Fig. 3.1C), with the same specifications and set up as at station VE. A RCM 11 was installed at 25 masf. An additional mooring with a 75 kHz ADCP, at 220 masf, was deployed at the same location. The height of this mooring allowed for the calculation of flow thickness, using depth averaged height calculations following the integral definition of Stacey and Bowen (1988). This ADCP recorded every 5 minutes, and had a 6 m vertical bin size.

The backscatter data of the 300 kHz ADCP at station VE were also used to estimate the sediment concentrations within the flows. The backscatter was converted to sediment concentration using an implicit inversion method with an iterative method of accounting for sediment attenuation (see Thorne and Hanes (2002)). The intensity of the acoustic backscatter depends on both grain-size of the suspended particles, as well as sediment concentration. Therefore, sediment concentrations derived by this method are sensitive to variations in grain-size. As the variations in grain-size are not known directly, we here assume that grain-size is constant with height above the bed, and through time (see Simmons et al. (2020) for a general discussion on likely

grain-size variation with height). As the Solveig III sediment samples were used for destructive sampling of carbon, an estimate from the Solveig I cruise (Silva Jacinto, 2008) between late November 2008 and early December 2008 was used instead. Here, a sediment trap at 500 mwd, a similar depth as Station VE, returned a mean grain-size of 40 μm. Furthermore, it is here assumed that the ADCP constant (Kt) is 2.31 x 10^7. The 75 kHz ADCP data, near station VV, is unsuitable for conversion of acoustic backscatter to sediment concentrations, due to a lack of a calibration value for a similar instrument.

3.7 Results

3.7.1 Var River observations

The river discharge followed its standard yearly cycle comprising a long-duration snow melt peak over the spring and summer, and high-intensity rainfall floods during winter (Fig. 3.2A). During the initial 4 months from July to September 2009, the river discharge gradually declined from 200 m^3 s^{-1} to 80 m^3 s^{-1}. Four winter floods occurred during the deployment (Fig. 3.2A). Two of these river-mouth floods exceeded 200 m^3 s^{-1}, with a peak discharge of 250 m^3 s^{-1} in October 2009, and a maximum peak discharge of 765 m^3 s^{-1} that occurred in December 2009. These two floods also correspond to increases in offshore flow velocities within the canyon, indicating turbidity currents were initiated in the Var Canyon (Fig. 3.2; events no. 4 and 5). The other two peaks in river discharge occurred in September and November 2009, with significantly lower discharges (86 and 105 m^3 s^{-1}), and did not produce turbidity currents at the seafloor moorings. Analysis of the local wind speed did not yield any correlation between the occurrence of turbidity currents and high wind speeds (Fig. 3.2A, blue line).

3.7.2 Var Canyon observations

At the most proximal station VH, there was a notable lack of turbidity current activity, with velocities limited to 20 cm s^{-1} (Fig. 3.2B). It is most likely that the flows were not recorded at station VH because this mooring was unintentionally deployed towards or on the canyon wall (Fig. 3.1B). The exact location is, however, hard to pinpoint due to the potential offset between the release location of the mooring and its final landing location. This is especially problematic in the narrow proximal part

TABLE 3.1: Overview of three main events measured at multiple sites (events 1, 4 and 5 in Fig. 3.3; 3.4).

		JULY [Event 1]		OCTOBER [Event 4]		DECEMBER [Event 5]*	
Var River	River discharge (m^3/s)	80		250		765	
	Calculated Suspended Sediment Conc. (kg/m^3) (after Mulder et al. 1998)	0.2-3		4-8		20-50	
Var Canyon	Station	VE	VV	VE	VV	VE	VV
	Onset	Gradual	Sudden	Sudden	Sudden	Sudden	Sudden
	Velocity pulses	Multiple surges	3 distinct repeats	Multiple surges	1 acceleration	Multiple cycles	1 acceleration
	Peak velocity (cm/s) [transit velocity]	34.8	26.4 [6.9]	61.8	30.2 [75.8]	101.6	84.4[64.1]
	Flow duration (hrs)	79-81hrs	71-78 hrs	21-25hrs	10-13 hrs	39-41 hrs	85-97 hrs
	Flow height (m) (approximately)	~20m	150m	>30m	130m	>30m	150m
	Temperature rise (Celsius)	0	0.2	0	0.2	0.2	0.2
	Sediment flux ($g/m^2/day$)	1624	242	532	90	5707	4956

*Only second stage of December event, 25th December onwards

of the canyon. Alternatively, it is possible the mooring was placed just on the side of the thalweg and that either the proximal turbidity currents were not thick enough to reach the current meters placed at 15 masf, or that the sediment plume from the river bypassed this VH mooring and flows started further down-canyon. Given the off-center release location, the narrow V-shaped canyon shape, and the total lack of velocity, temperature and turbidity signals, it is most likely that the mooring was misplaced, and therefore station VH did not record any of the turbidity currents. Station VE (ADCP data) and VV (RCM current meter data) recorded five separate turbidity currents, which are termed flows 1, 2, 3, 4 and 5 (Fig. 3.2). Flows 2 and 3 were recorded only at a single mooring, and are considered to be minor local events, as neither flow led to increased sediment flux in traps (Fig. 3.2C-D). The three remaining events (flows 1, 4 and 5) did lead to an increased sediment flux, and were recorded by both mooring station VE and VV (Fig. 3.2; Table 3.1). These three flows are now discussed in more detail (Figs. 3.3 and 3.4).

3.7.2.1 July event (Event no. 1)

This turbidity current lasted from 30 June to 5 July 2009. During this period, the Var River lacked a distinct flood peak (Fig. 3.3A). Instead, the river's discharge ($\sim$80 m^3 s^{-1}) continued a gradual decline following the peak snow melt in early spring (Fig. 3.2). Previous measurements have shown that comparable discharge levels in the Var River correspond to suspended sediment concentration of up to 3 kg m^{-3} based on previous direct river measurements (Mulder et al. 1998; Table 3.1). At

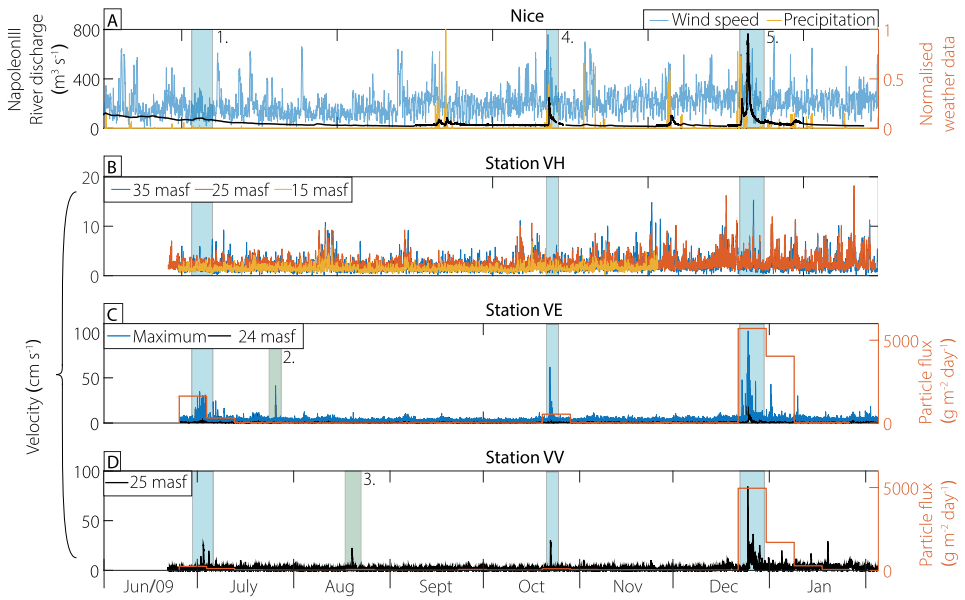

FIGURE 3.2: Complete time series of monitoring data. Five turbidity current events are highlighted, and numbered from 1 to 5. The three flows recorded at all moorings are shown by blue boxes, whilst green boxes highlight events only recorded at individual stations. A) Detailed time series of data from land stations. The NapoleonIII station provides river discharge data (black line, left axis). Wind speed (blue line) and precipitation (orange line) data come from the MeteoFrance station, and these weather data are normalized using the minimum and maximum values that occurred during the study period (right axis). B) Velocity measurements from single-height current meters (RCMs) at station VH, located at 15, 25 and 35 meters above seafloor (masf). C) Velocity measurements from a 300 kHz ADCP at station VE. Maximum velocity, and velocity at 24 masf, are shown for comparison. Particle flux from a sediment trap at station VE, based on a 9-day average. D) RCM velocity measurement from station VV, located at 25 masf, and particle flux based on 9-day average.

station VE, the July turbidity current lasted for nearly ∼3.5 days (Table 3.1). The velocity signal, as well as the sediment concentration, were characterized by a gradual onset followed by a long series of pulses (Figs. 3.3 and 3.4). Velocities and sediment concentrations gradually rose until a peak velocity of 35 cm s^{-1} occurred after roughly 1.3 days. Event 1 was not associated with an increase in temperature at station VE (Fig. 3.3B).

Ten kilometers further down canyon, at station VV, the July event re-organized in three distinct pulses, each lasting for ∼5-10 hrs. All these pulses show a sharp increase in velocity and temperature at the start of the flow followed by a gradual decline (Fig. 3.3C). The peak velocities are similar to those measured at station VE (Table 3.1, Fig. 3.3). The transit velocity between station VE and VV is particularly slow at ∼7 cm s^{-1}, suggesting that the first velocity peaks observed in VE dissipated before reaching station VV. The transit velocity would be more in agreement with

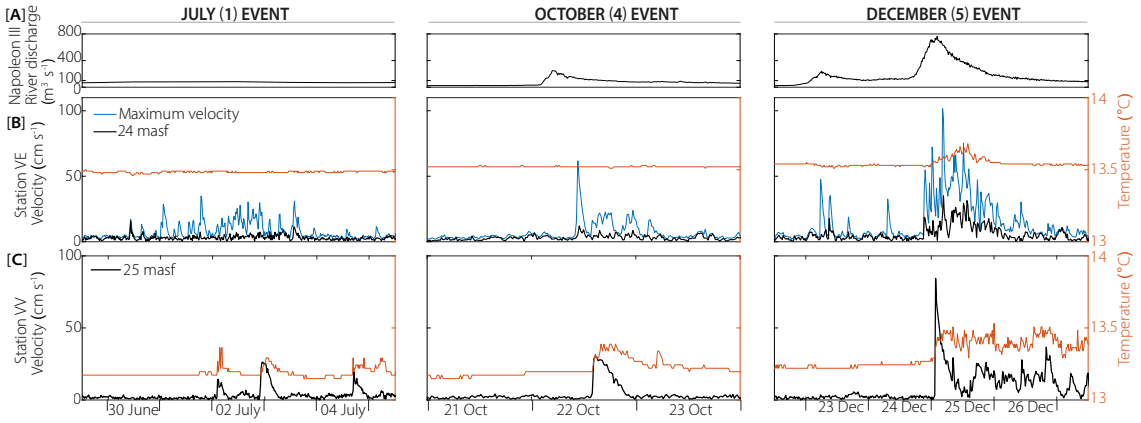

FIGURE 3.3: Detailed measurements for turbidity current events 1, 4 and 5 (see Fig. 3.2 for full time series). (A) River discharge at the NapeoleonIII station. (B) ADCP velocity (maximum recorded, blue, and at 25 masf, black) and temperature data from station VE. (C) RCM velocity and temperature data (both at 25 masf) at station VV. The scale is the same for velocity and temperature data at each station in parts (B) and (C).

the direct velocity measurements if early peaks dissipated between VE and VV, and a later velocity peak from station VE is considered to arrive first at station VV.

3.7.2.2 October event (Event no. 4)

Flow 4 in October 2009 coincided with a Var River flood with a discharge peak of 250 m^3 s^{-1} (Fig. 3.3A), equating to a suspended sediment concentration within the river of ~8 kg m^{-3} (Mulder et al. (1998); Table 3.1). At station VE, the duration of the event was between 20-24 hours (Table 3.1). The velocity structure and sediment concentration consist of a sudden onset followed by a complex series of higher and lower pulses (Figs. 3.3B and 3.4B). A peak velocity of 62 cm s^{-1} occurs at the front of the turbidity current.

At station VV, the flow duration was reduced by 50% to 10-13 hours (Figs. 3.3C and 3.4C, Table 3.1). The turbidity current is characterized by a single pulse with an abrupt onset. The velocity peaks at 30 cm s^{-1} at the start of the event, followed by a steady decline in velocity. Again, the increase in velocity at station VV is paired with an increase in temperature (Table 3.1, Fig. 3.3). The transit velocity between these two moorings, at 76 cm s^{-1}, suggests an acceleration of the turbidity current before its arrival at station VV.

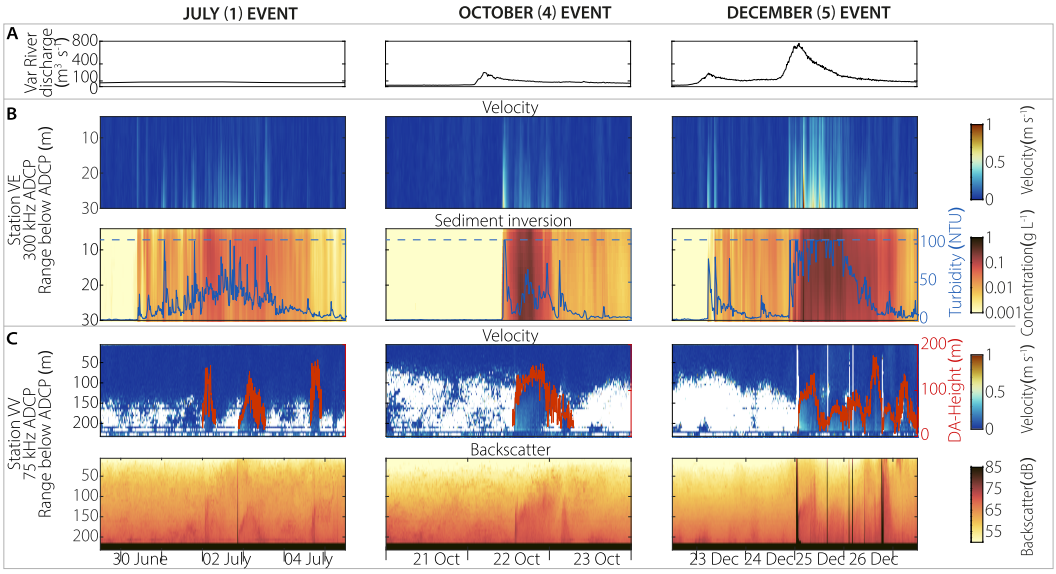

FIGURE 3.4: Comparison of flow structures for the three events recorded at multiple mooring sites (events 1, 4 and 5 in Fig. 3.2). (A) River discharge from Napoleon III station. (B) Time series data from 300 kHz ADCP at station VE, showing velocity and sediment concentration (from backscatter inversion) structure of each event. ADCP backscatter inversion is corrected for attenuation, and measurements from the turbidity sensor at 15 masf are shown by blue line, with saturation level indicated by blue dashed line. (C) Time series data from 300 kHz ADCP at station VV, showing velocity and acoustic backscatter structure of each event. At this site, ADCP backscatter data could not be inverted to sediment concentration due to coarse vertical resolution. Red line shows the flow thickness based on depth averaged (DA) height calculations following Stacey and Bowen (1988).

3.7.2.3 December event (Event no. 5)

Event 5 is associated with the largest flood observed during this 7-month deployment (Fig. 3.2). This flood consisted of two stages, and occurred between 23 and 26 December. In the first stage (23rd December), the river discharge increased over a ~7-hour window up to a peak discharge of 240 m^3 s^{-1} (Fig. 3.3A). This first peak is followed by a 28-hour period in which an elevated river discharge of ~120 m^3 s^{-1} was maintained. In the second stage (25th December), the rising limb of the flood reached its maximum discharge of ~765 m^3 s^{-1} in 10 hours (Fig. 3.3A). Overall the second stage flood lasted for about 39 hours, and the entire duration of elevated discharge during the December event is ~3.5 days. Extrapolation of the suspended sediment concentration in the river indicate that sediment concentrations of 20-50 kg m^{-3} are likely to have occurred during the second stage of the flood. Such levels of suspended sediment could be sufficient for the formation of a hyperpycnal turbidity current (Mulder et al., 1998).

At station VE, the measured velocities of the December event mirror the two-stage

river discharge curve. On the 23rd of December, following the first stage of the river flood, a sharp increase in the velocity and sediment concentration is observed at VE (Figs. 3.3B and 3.4B). The sharp increase is followed by several lower velocity peaks until the second stage. As the river reached its maximum discharge on the 25th of December, a series of new and higher velocity peaks were recorded at station VE. This second stage lasted for about 42 hours, had a sharp onset, with a further increase in sediment concentration, and reached its peak velocity (102 cm s^{-1}) about 7 hours after the start of this second stage (Figs. 3.3B and 3.4B; Table 3.1). Interestingly, the second stage of the December event is the only event that is significantly warmer than the ambient water at station VE.

The velocity peaks of the first stage of the December event are not observed at station VV. The arrival of the second stage is marked by a sharp increase in the velocity to its peak value of 85 cm s^{-1}, which is followed by a continuous decrease lasting about 13 hours. In the following 3-4 days, multiple velocity peaks, or pulses, occured (Figs. 3.3C and 3.4C). The transit velocity between station VE and VV, based on the first arrival time at either station, is 65 cm s^{-1}. The observed maximum velocity peak at station VE (102 cm s^{-1}) occured after the arrival of the front peak at station VV, and hence this proximal maximum velocity peak cannot be the distal maximal velocity peak. This observation implies that the maximum velocity peak at VE is not maintained down-canyon, but instead this proximal maximum velocity peak dissipates and becomes just a minor velocity peak at station VV.

3.8 Discussion

3.8.1 Is there a unique proximal structure of flood-triggered turbidity currents?

Flood-triggered turbidity currents are proposed to be identifiable by up to four criteria, such as a long duration, gradual onset, possible multiple cycles and relatively low velocities (Mulder et al., 2003, Khripounoff et al., 2012, Zavala and Pan, 2018). All turbidity currents observed in the proximal station in the Var Canyon display at least two of these characteristics, as all events (1, 4, 5) consist of multiple cycles and have a long duration in comparison to previous measurements in the Var Canyon (Khripounoff et al., 2012). The July event (event 1) was the only turbidity current with a gradual onset, and had low velocities in comparison to both the October and December events (events 4 and 5) as well as compared to events reported by Khripounoff

et al. (2012). So, if all events observed in this proximal mooring were flood-triggered, then the proposed set of criteria would work well to recognize flood-triggered turbidity currents. However, in contrast to the October event and December event, which were associated to river floods, the July event did not coincide with a river flood (Fig. 3.3).

Although the July event (event 1) fits the flood-triggered criteria best, it lacks any association with a flood. However, during the October and December events the river floods produced sufficiently high suspended sediment concentrations (4-8 kg m^{-3} for October and 20-50 kg m^{-3} for December; Table 3.1) to enable direct transfer of suspended sediment from the river to the turbidity current. For both events the sediment transfer could have occurred through convective fingering (Parsons et al., 2001). Additionally, the second stage of the December event (event 5) could be a hyperpycnal turbidity current, as the sediment concentration is sufficient for the river discharge to plunge and move along the seabed. Such a hyperpycnal trigger would be consistent with the unique increase in temperature observed at VE during this second stage.

The July event lacks a clear river flood (event 1, Figs. 3.2 and 3.3). Yet, during the July event the suspended sediment levels in the river discharge are estimated to be up to 3 kg m^{-3} (Table 3.1), which is still sufficient to form convective fingers (Mulder et al., 1998, Parsons et al., 2001). The river discharge measurements indicate that similar or higher levels of sediment concentration are expected continuously in the weeks leading up to the July event. Hence, if convective fingers were responsible for the transfer of sediment from the river to the submarine canyon, this should have resulted in continuous turbidity current activity over the weeks leading up to the event. Such continuous turbidity current activity was neither observed in the weeks leading up to the July event, nor in earlier measurements of Khripounoff et al. (2009) during similar river discharges in the years 2006 and 2007. It is more likely that the July event was initiated by some form of landslide, which generated a relatively sustained flow at the proximal VE station (Fig. 3.3B). One possible hypothesis is that this turbidity current was triggered by retrogressive (breaching) failure, which can lead to continuous sediment supply and thus prolonged flow (Mastbergen and Van Den Berg, 2003). Alternative initiation mechanisms, such as dense-water cascading or benthic storms, are less likely as the meteorological data do not indicate exceptional weather circumstances, nor is there a change in water temperature discernible at the station VE. A temperature drop would be expected for dense (cold) water cascading. Potentially, the relatively coarse data resolution limited the interpretation. However, the data still show gradual rise in velocity onset, despite the coarse temporal resolution,

and more detailed data will likely further highlight a gradual rise in velocity onset. The July event fits the flood-triggered criteria best (gradual onset, multiple cycles, low velocity and long duration). Thus, it is important that this July event was most likely triggered by a landslide. Although the flood-triggered criteria are present in the Var Canyon observations, these criteria might not be unique to flood triggers.

3.8.2 How does the proximal velocity structure evolve down-canyon?

We now discuss how the proximal velocity structure of the flows evolved and changed with distance, and its implications for inferring triggers from grain-size patterns in deposits. Next, we discuss what controls the evolution of this velocity structure.

The typical proximal velocity structure observed in station VE is different from the typical velocity structure seen 10 km further down canyon. At the proximal VE station, the three main events (1, 4, 5) all show multiple cycles of acceleration and deceleration (pulses). However, at the VV station, these multi-pulsed turbidity currents have self-organized into single-pulsed flows. At the most distal VV station, all these single-pulsed flows show a dominant velocity peak at the front of the flow, followed by a steady decline; as typically expected for landslide-triggered turbidity currents (Kneller and Buckee, 2000). This down-canyon transformation, from multi-pulsed to single-pulsed turbidity current, is consistent with laboratory experiments of Ho et al. (2018). These authors found that amalgamation of multi-pulsed flows is likely, as faster pulses within the flow experience a reduction in drag and consequently experience a forward advection to the flow front. The reduced drag is caused by the stratified water column that remained after the passage of the first pulse (Ho et al., 2018). The result of this efficient amalgamation of pulses in the Var Canyon system is that flooding signals are effectively shredded within the first 16 km of the submarine canyon system.

However, the field observations also show that amalgamation of pulses is not as straightforward as seen in laboratory experiments. For example, during the second stage of the December event (25^{th} of December onwards), the fastest peak is unable to catch up with the slower leading peak. Although this originally higher velocity peak from station VE is discernible 10 km downstream, it is now slower than the frontal peak. This suggests that amalgamation of individual flow pulses also depend on other factors besides reduced drag. We propose that the pulse propagation also depends on availability of easily erodible substrate on the seafloor. For the second stage of the

December event, the frontal pulse might have eroded the sediment freshly deposited by the first stage, causing the observed self-acceleration. Subsequently, the depleted seafloor could not fuel the following higher velocity peaks, resulting in deceleration of those initially higher velocity peaks. The importance of erosion and the state of the seafloor is consistent with previous observations. For example, Liu et al. (2012) documented that the first typhoon of the season produces the strongest turbidity current, Hage et al. (2019) showed that the first low tide of the spring cycle produces a fast and erosive turbidity current, and Heerema et al. (2020) showed that the first event after a prolonged quiescent period triggers the most ignitive flow. Overall, here in the Var Canyon the combined effect of erosion and amalgamation results in shredding of the flood signal within 16 km of the river mouth.

3.8.3 Further implications for identifying turbidity current deposits triggered by river floods

3.8.3.1 The applicability of depositional models

We now use our direct measurements to assess existing depositional models for flood-triggered events. The processes underpinning these models have been heavily debated (i.e. Shanmugam, 2018, van Loon et al., 2019, Zavala, 2019), and have led to three competing depositional models (Mulder et al., 2003, Plink-Björklund and Steel, 2004, Nakajima, 2006, Talling, 2014). Central to the initial model from Mulder et al. (2003) is that waxing and waning of the river flood causes a waxing and waning turbidity current velocity structure, and this is subsequently recorded in deposits via inverse-to-normal grading. This model suggests that the gradual rising limb of the river leads to a gradual increase in the velocity of the turbidity current, which in turn is recorded as a coarsening upward (inverse-graded) sequence in the deposits. Next, the falling limb of the flood produces a gradual decrease of the turbidity current velocity that produces an upward fining (normal-graded) deposit. Later models of Plink-Björklund and Steel (2004) and Zavala et al. (2006) include incremental deposition of thick sandy deposits due to prolonged duration of hyperpycnal events. This is in contrast to a third model that suggests flood-triggered turbidity currents form thin, fine-grained deposits, due to the slow and dilute nature of flood-triggered turbidity currents (Nakajima, 2006, Talling, 2014).

In our direct measurements, we do indeed find prolonged durations of flood-triggered events 4 and 5. These events last up to 4 days, and could lead to thick deposits as

suggested by Plink-Björklund and Steel (2004) and Zavala et al. (2006). The variable peak velocities (26 - 102 cm s^{-1}) between the measured events could be consistent with both the proposed sandy beds (Plink-Björklund and Steel, 2004, Zavala et al., 2006), as well as finer silt beds (Nakajima, 2006, Talling, 2014), as deposit grainsize can be an indication of the energy, and thus velocity, of an event (Komar, 1985). However, the velocity onset of the events tends to be abrupt, especially at the distal station, suggesting that the inverse grading proposed by Mulder et al. (2003) becomes less likely with distance from the river mouth.

Remarkably, multiple inverse-graded deposits are found on a terrace in the Var Canyon at ∼30 km from the Var river mouth, and are interpreted to reflect river-triggered turbidity currents (Mulder et al., 2001). These findings contradict our measurements that demonstrate efficient self-organization of turbidity currents within 16 km from the Var River mouth. The existence of these inverse-graded deposits of Mulder et al. (2001) could suggests that more exceptional events in the geologic record are able to retain their gradual velocity onset further down-canyon, leading to these distal inverse-graded deposits. The persistence of these inverse-graded deposits further offshore suggests that the recent direct monitoring observations do not yet include those high-magnitude low-frequency turbidity currents (Mas et al., 2010). Some insights into these high-magnitude flows might be gained from looking at the large hyperpycnal turbidity current in December. Proximally, this event does indeed show a somewhat gradual onset, as the peak velocity occurs ∼7 hours after the start of the event. However, amalgamation prevents the preservation of this gradual onset further downstream. Interestingly, the large hyperpycnal event (maximum river discharge 610 m^3 s^{-1}) measured by Khripounoff et al. (2012) on December 15, 2008, shows that amalgamation is not always able to completely re-organize turbidity currents within the first 16 km. The December event presented in Khripounoff et al. (2012) shows how a large flood-triggered flow generally resembles a landslide-triggered velocity structure at location VV, just like the events presented here. However, this December 2008 event still consists of two distinct peaks at station VV (Khripounoff et al., 2012). The second, faster, peak is projected to catch up within 5-10 km to finalize self-organization into a single peak, surge-type flow, based on their peak velocity and arrival times. Potentially, the incomplete amalgamation observed by Khripounoff et al. (2012) could be due to the fact that the rising limb of that December event lasted twice as long as the December flood presented here. It may thus be possible that during even longer river floods, the flood-triggered velocity structure is preserved further offshore. Such preservation of the gradual onset of the turbidity current velocity could explain the observed inverse grading deposits by Mulder et al.

(2001).

In summary, all three depositional models are to some extent consistent with our direct measurement observations of flood-triggered events. Flood-triggered events could indeed result in traction structures, such as climbing ripples or plane-parallel lamination, due to sustained flows (Plink-Björklund and Steel, 2004, Zavala et al., 2006). Especially proximally, large flood-triggered events could also result in inverse-to-normal graded sequences (Mulder et al., 2003), and vertical alternation of traction structures reflecting cyclicity in the flow (Nakajima, 2006, Zavala et al., 2006). Although all proposed models work for some flows, it should be kept in mind that none of these depositional models apply exclusively to all flood-triggered flows. Furthermore, events without a flood trigger can also fulfil the proposed criteria for flood-triggered events.

3.8.3.2 How reliable is the depositional record for reconstructing paleo-floods?

Turbidite records of paleo-floods have been used to reconstruct recurrence intervals of river flooding (Mulder et al., 2001, Nakajima, 2006), and understand the effects of sea-level change on river floods (Plink-Björklund and Steel, 2004). However, this study has shown that although the velocity structure of flood-triggered turbidity currents is consistent with the proposed criteria, this structure is not unique to flood-triggered events (Fig. 3.5). For instance, initially multi-pulsed and prolonged velocity structures have been observed without a flood, as in the landslide-triggered July event (event 1). Moreover, similar river discharge levels have not consistently led to turbidity currents in the canyon. For example, Khripounoff et al. (2012) observed a 640 m^3 s^{-1} river flood that did not immediately lead to a turbidity current, whilst a 610 m^3 s^{-1} river flood produced a turbidity current. Additionally, three similar river floods of $\sim$250 m^3 s^{-1} led to substantially different turbidity current activity. A first flood (230 m^3 s^{-1}) described in Khripounoff et al. (2012) did not lead to any activity. A second flood (240 m^3 s^{-1}) during the first phase of the December event (described here) led to activity only at the first mooring. Lastly, the October flood (250 m^3 s^{-1}, described here) triggered an event that was observed at all mooring stations. Thus, recognition of paleo-floods based only on velocity structure and subsequent grain-size trends might be problematic. Additional indicators, such as substantial organic matter content with high carbon-nitrogen ratio, could be needed to confidently infer flood triggers. However, this may also be problematic, as seabed failures on the delta may also remobilize recently deposited sediment with similarly high organic carbon

contents or carbon-nitrogen ratios.

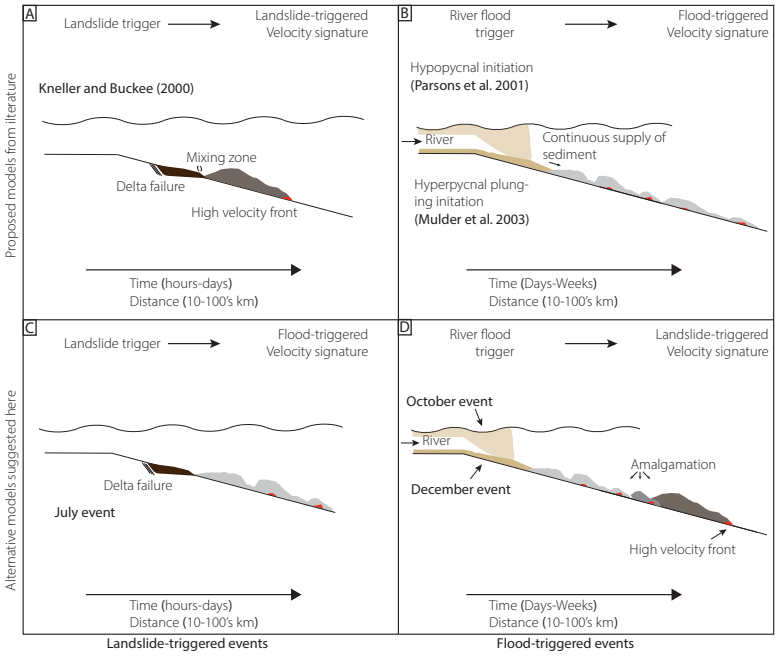

FIGURE 3.5: Summary figure of how different triggers are linked to subsequent flow structures. (A) and (B) are the classic mechanisms pre-existing in literature, showing how specific triggers lead to unique velocity signatures. (C) and (D) show crossover mechanisms discussed in this study. Here, specific triggers do not lead to their expected velocity signatures.

In conclusion, turbidity currents without a flood trigger can resemble flood-triggered turbidity currents (Fig. 3.5), potentially due to the sustained nature of breach failures. In addition, flood-triggered turbidity currents can look like landslide-triggered turbidity currents, as erosion and amalgamation in turbidity currents lead to self-organization of the flow within tens of kilometers. Lastly, similar river flood discharges do not consistently lead to similar turbidity currents. Thus, reconstructing paleo-floods on the basis of the rock record might prove substantially more complicated than previously assumed.

3.9 Acknowledgements

We thank the crew members of the Solveig III cruise, as well as all technicians and the scientific team involved in the efforts. CJH is funded by the European Unions' Horizon 2020 research and innovation program under the Marie Skłodowska-Curie grant agreement No 721403 - ITN SLATE. MJBC was supported by a Royal Society Research Fellowship.

Chapter 4

How do the frequency and magnitude of turbidity currents change with distance, and what controls this pattern?

This chapter is being prepared for sumbission to *Sedimentology*: **Heerema CJ**, Talling PJ, Hage S, Chen Y, Pope E, Cartigny MJB, Stacey CD, Lintern GD, Enkin R, Croudace IW, Clare MA (tbc). 'Source-to-sink study of turbidity current frequency and magnitude in fjords.'

Kate Heerema is responsible for the data analysis, visualisation, conceptualisation and writing the paper. The data collection was carried out by several co-authors, and organised by IOS, Canada. Core logs were provided by SH and YC. Subsampling was done by KH, facilitated by IOS co-authors. Sediment analysis at GAU was in collaboration with IWC. Invaluable input in writing the chapter was provided by PJT, MJBC, and EP.

4.1 Abstract

It is important to understand how the frequency and magnitude of turbidity currents vary with distance from source for assessing hazards to seabed infrastructure, and to determine the rate of sediment and organic carbon transfer into the deep sea. To understand both long-term and short-term system behaviour, a combination of deposits

and direct monitoring of turbidity currents is essential. Yet, very few studies have combined these data to understand how turbidity current frequency and magnitude vary over distance from source to sink. Here we present one of the most detailed studies yet of source-to-sink event frequency and magnitude along a channelized submarine system. Two direct measurement field campaigns, each conducted over ∼6 months, are combined with sediment cores.

Three event frequencies are recognised in Bute Inlet. High frequency flows are measured directly, and are initiated during spring thaw, i.e. the freshet season. Ca. 100 events occur at the delta near the channel head, with activity declining to 1 event per year over a ∼45 km long channel. Intermediate frequency events occur every ca. 20 years, and are recorded as coarse-grained sandy deposits on the terraces above the channel thalweg. A proposed key mechanism for these events is the migration of knickpoints. These steep steps in the channel migrate upstream on average past a point on the channel every ∼15 years. Prior to erosion the height between terrace and thalweg will be temporarily reduced, thereby allowing for coarse-grained sand deposition on terraces. This implies that there need not be a magnitude difference between high and intermediate frequency events, but only a difference in relative thalweg elevation. High magnitude, infrequent, events are deposited in the deep basin. Here, thick and large-volume sands were last deposited ∼240 years ago. The origins of these events remain speculative, but it appears other factors control these flows, such as landslides or glacial lake outburst floods.

These event frequencies and magnitudes found in Bute Inlet are comparable to the nearby Howe Sound fjord system. Both systems show high current-day activity in the channel, and see a recurrence of much larger events on centennial timescales. Thus, it might be that these large-scale events are due to regional or global mechanisms, found in other submarine systems as well.

4.2 Introduction

Turbidity currents are sediment-driven gravity currents occurring on the seafloor. These events can be very powerful, and they are a globally important mechanism for transporting nutrients, carbon, and sediments to the deep-sea. Turbidity currents therefore dictate the fluxes on which benthic ecosystems (Paull et al., 2010a), carbon sequestration (Galy et al., 2007) and the global sediment cycle (Talling et al., 2012) depend. To better quantify these fluxes, we need to understand how and why the frequency and magnitude of turbidity currents vary with distance. Understanding

turbidity current frequency and magnitude will also allow for better risk assessments for underwater infrastructure, including telecommunication cables and oil and gas pipelines (Carter et al., 2014, Sequeiros et al., 2019). Furthermore, determining the frequency and triggers of turbidity currents may provide insights into other important geohazards, such as river floods and earthquakes (Mulder et al., 2001, Goldfinger et al., 2007, Johnson et al., 2017). Whereas the frequency-magnitude distribution of events has long been measured in subaerial rivers (Wolman and Miller, 1960), there are few studies on turbidity current frequency and magnitude, and even fewer studies that provide detailed information of how this changes from source-to-sink.

Obtaining data from active turbidity current systems is difficult, as events are often powerful, destructive and infrequent (i.e. Prior et al., 1987, Paull et al., 2018, Clare et al., 2020). Recent developments have led to more direct measurements, giving further insights into turbidity current activity (Xu, 2010, Khripounoff et al., 2012, Azpiroz-Zabala et al., 2017, Paull et al., 2018). However, these direct measurements are usually restricted to the proximal parts of systems (i.e. Paull et al., 2018), or have a limited number of measurement stations (i.e. Khripounoff et al., 2012). Furthermore, turbidity currents captured by these direct measurements are typically the smaller scale and more frequent events that infill submarine canyons or channels, rather than much larger and more infrequent flushing events (Piper and Normark, 2009, Stevens et al., 2014). A large-scale event, passing through an entire submarine canyon, has yet to be documented (Fildani, 2017), as monitoring periods are of relatively short duration (i.e. Prior et al., 1987, Xu, 2010, Khripounoff et al., 2012, Paull et al., 2018). Deposits from turbidity currents are thus needed to understand larger magnitude and more infrequent events (Talling et al., 2015). Previous studies which used deposits for the analysis of past event frequencies commonly included deposits at distal locations (i.e. Mulder et al., 2001, Goldfinger et al., 2007, Stevens et al., 2014, Gwiazda et al., 2015, Allin et al., 2016). Combining data from cored deposits and direct monitoring is needed to determine turbidity current magnitude and frequency spanning greater distances and times. We are currently only aware of one other study that has combined direct measurements with deposits, which comes from Howe Sound in British Columbia (Stacey et al., 2019). However, this study only had monitoring data from one mooring. Furthermore, recent forced avulsion (in 1971) of the Squamish River has led to re-routing of the system and thus poorly developed submarine channels that extend for < 2 km (Stacey et al., 2019). This forced avulsion is likely to have modified the frequency-magnitude characteristics.

Here, we present a uniquely detailed dataset from Bute Inlet, a fjord in British Columbia, Canada (Fig. 4.1). These data include direct measurements at six loca-

tions along a 45 km long submarine channel. These direct measurements give insights into present-day activity in the incised channel, from the proximal delta to the distal lobe. These measurements are combined with sediment cores which have been obtained throughout the submarine system, including the channel and distal, unchannelised, deep basin (Fig. 4.1). This study will use a unique combination of sediment cores, sediment accumulation rates, and detailed direct monitoring, to analyse how the frequency and magnitude of turbidity currents vary from source-to-sink along the fjord.

4.3 Aims

The overarching aim is to understand the spatial and temporal scale of turbidity current activity from source-to-sink. This chapter has three specific aims. First, we aim to document the frequency and magnitude of turbidity currents in Bute Inlet. Second, we seek to understand what causes the observed frequency-magnitude distribution. Third, we aim to put the findings from Bute Inlet in a broader perspective, by comparing them to a nearby submarine system (Howe Sound) where sufficiently detailed information is available.

4.4 Study Area

Bute Inlet fjord is located in British Columbia, Canada. Two main rivers feed into the fjord, the Homathko and Southgate Rivers (Fig. 4.1A). The Homathko River provides the primary influx of freshwater (75%), with the Southgate River supplying 15% of the total annual freshwater influx, and numerous small streams along the margin providing the remaining 10% (Zeng et al., 1991). The Homathko River has a mean monthly discharge of $\sim$270 m^3 s^{-1} (`https://wateroffice.ec.gc.ca/index_e.html`), with a sediment load that comprises 15% gravel, 65% sand, 15% silt and 5% clay (Prior et al., 1986). From the Homathko Delta, the submarine system stretches out for 80 km to 650 m depth in the deep basin, where a sill dictates the end of the submarine system. The submarine system can be divided into five morphological regions (Fig. 4.1A, adapted from Zeng et al. (1991)). The *delta* includes the Homathko and Southgate Deltas, and is considered to start at the Homathko Delta, extending for $\sim$7 km to include the upper-most incised channel as well. The remaining $\sim$35 km of the incised channel can be divided into two further zones. The *upper channel* ex-

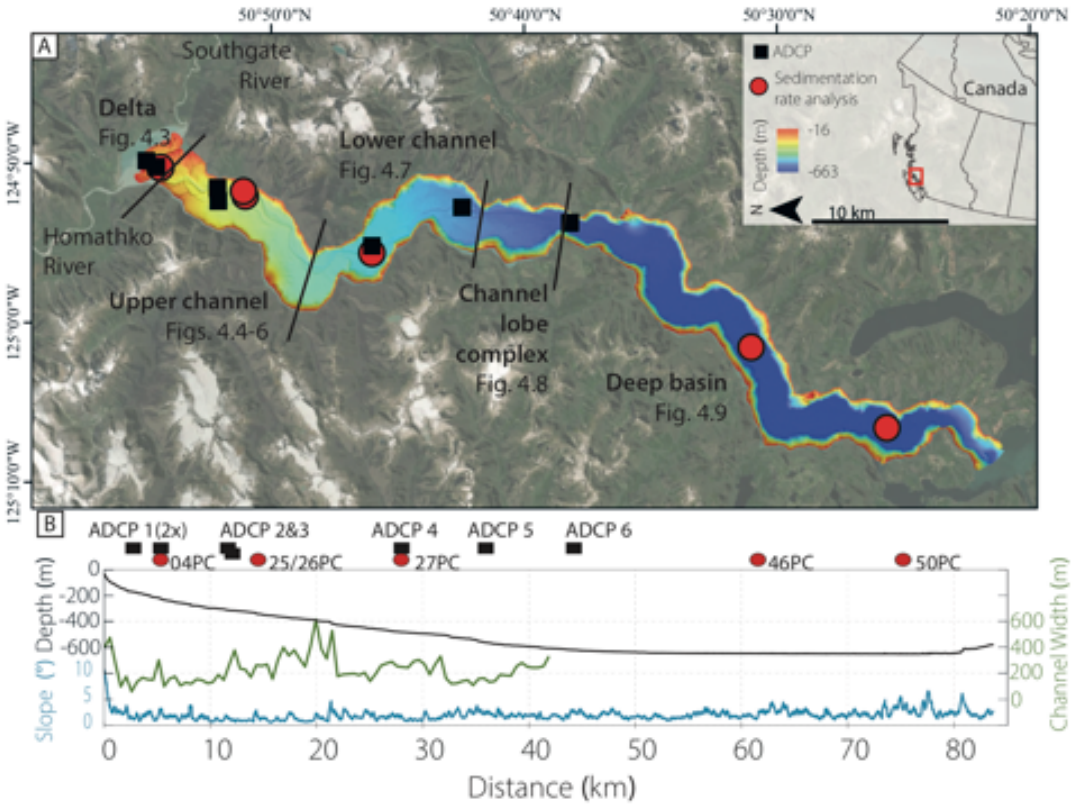

FIGURE 4.1: A) Bathymetry map of Bute Inlet. The map includes the morphological zones, locations of mooring stations with acoustic Doppler current profilers (ADCPs, black squares) and sediment cores that are analysed for sediment accumulation rate (red circles). Base map is from ESRI, see Heijnen et al. (2020) for details on bathymetry data. B) Seabed gradient along thalweg (blue), water depth (black), and submarine channel width based on distance between terraces (green) for the Bute Inlet submarine system. Also indicated are locations of ADCPs and sediment cores analysed for accumulation rate .

tends from ∼7-22 km, and consists of an incised channel with multiple terrace levels. The *lower channel* has a simpler geometry, where the incised channel has a single terrace, located ∼15-20 m above the thalweg, although this incised channel becomes less distinct distally. This lower incised channel extends between ∼22-37 km from the Homathko Delta, and transitions into the *channel-lobe-complex* (37-42 km). Finally, beyond the lobe is the *deep basin*, extending another ∼35-40 km towards the Georgia Strait. The slope varies from ∼8° on the delta-front, to ∼1.5° - 0.5° in the incised channel. The slope in the deep basin is less than 0.05°, although near the sill there can be some fluctuations in the slope (Fig. 4.1B; Prior et al. (1987), Gales et al. (2019)). The width of the ∼42-km long incised channel varies between 100-400 m (Fig. 4.1B).

The well-established channel in Bute Inlet is a result of extensive turbidity current activity (Gales et al., 2019), typically coinciding with elevated river discharge dur-

ing the spring thaw, or freshet season (Prior et al., 1987, Bornhold et al., 1994). Subsequent channel maintenance and deepening of the submarine channel is driven by knickpoints, which are upslope migrating steep steps on the channel floor (Gales et al., 2019, Heijnen et al., 2020). The first direct measurement of turbidity current activity in Bute Inlet stems from 1985. Geophysical instruments were deployed at three locations along the channel axis, including current meters, event detection vanes and tilt meters (Prior et al., 1987). Events with maximum velocities of 3.4 m s^{-1}, and thicknesses exceeding 30 m were detected. Prior et al. (1987) found two different frequency and magnitude scales based on the mooring data: low velocity, frequent events with limited runout, and large-scale infrequent events travelling at high velocities over long distances. A subsequent study recorded 35 events during a 13-month deployment period, with 80% of events occurring when the Homathko River discharge exceeds 300 m^3 s^{-1} (Bornhold et al., 1994).

4.5 Methods

The data discussed here were collected aboard the Canadian Coast Guard Ship (CCGS) Vector, and Research Vessel John Strickland, including sediment cores and direct monitoring data. Both types of data capture the spatial evolution of turbidites from the delta to the lobe. The sediment cores further include the distal basin as well.

4.5.1 Direct measurements

Six downward-looking acoustic Doppler current profilers (ADCPs) were deployed in 2016 and 2018, covering the submarine system from the delta morphological zone up to the channel-lobe-complex (Fig. 4.1; Table 4.1). These instruments all had a recording interval of 10s or less. In 2016, moored instruments were deployed from June until October, and in 2018 between May and November (Pope et al., in prep; Chen et al., in prep). Figure 4.1 shows the locations of all moorings. The three distal moorings were deployed at approximately the same locations during both field campaigns. The first ADCP, nearest the Homathko Delta, was located 2.5 km further upstream in 2018, as compared to 2016. Moorings two and three monitored a prominent knickpoint during both field campaigns, with an ADCP upstream and downstream of the knickpoint. In 2018, these moorings were placed 350 m further upstream to capture the same knickpoint. Due to a technical issue no velocities were

TABLE 4.1: Specifics of the ADCP deployments in Bute Inlet over the 2016 and 2018 field seasons.

Mooring	2016 Distance from Homathko Delta (km)	2018 Distance from Homathko Delta (km)	Morphological Zone	Comments on Data Collection
ADCP 1	5.3	2.9	Delta	2016 Only Backscatter Data; Failed after 31/07/2016
ADCP 2	11.9	11.5	Upper Channel, Upstream Knickpoint	2016 Only Backscatter Data. 2018 Failed, No Data
ADCP 3	12.5	12.1	Upper Channel, Downstream Knickpoint	2016 Only Backscatter Data
ADCP 4	27.9	27.9	Lower Channel	
ADCP 5	35.7	35.7	Lower Channel	2016 Only Backscatter Data
ADCP 6	43.9	43.9	Channel-Lobe-Complex	2016 Only Backscatter Data

recorded in 2016, apart from the fourth ADCP. Furthermore, in the 2016 field season the first ADCP, located closest to the Homathko Delta, failed at the end of July. In 2018 the second ADCP, located upstream of the knickpoint, did not record any data (Table 4.1).

The ADCP data are used to determine runout distance of events. The ADCPs record vertical changes in the water column, in either backscatter intensity (a proxy for sediment concentration) or velocity. The event arrival is derived from a sudden change in velocity and/or backscatter data. ADCP along-channel distances from the Homathko Delta are subsequently used to determine runout distance of events. If events dissipate between moorings, the upstream mooring is considered the terminal point for that event.

4.5.2 Sediment cores

A total of 50 box (BC) and piston (PC) cores were obtained between 2015 and 2018 (Figs. 4.3-4.9). The sediment cores in the channelized system of Bute Inlet are predominantly located near ADCP locations, with additional piston core sites on the basin floor. The piston cores have a diameter of 6.5 cm, and can reach up to several meters' depth below the seafloor, although near-surface disturbance is common. Box cores, with a maximum depth of approximately 30 cm, preserve sediment structures near the seafloor surface. The sediment cores were logged, and grain sizes were assessed visually during logging, following clay-silt-very fine-fine-medium sand divisions (mud-2000μm). Selected piston cores had x-radiographs taken. The sediment cores

are used to understand the spatial and temporal change in sediment deposition. The deposit thickness and maximum observed grain size give an indication of the energy of an event. As the slope in the channelized system is relatively constant, and assuming a wider range of grain sizes are always available, then grain size will be a direct indicator of event speed and hence relative flow intensity (Komar, 1985).

4.5.3 Sediment accumulation rates and age dating

Sediment accumulation rates were calculated based on ^{210}Pb activity alongside ^{137}Cs. Analysis was done by GAU-Radioanalytical Laboratories (University of Southampton) under oversight from Raddec International Ltd. ^{210}Pb accumulation rate calculations are based on the difference between background and surplus ^{210}Pb. The background ^{210}Pb stems from continuous radioactive decay of ^{238}U in the sediments, and is considered stable over time (Appleby and Oldfield, 1992). The excess ^{210}Pb originates from atmospheric input, which gets fixed to terrestrial material to eventually be deposited on the seafloor. Assuming a constant influx of this excess ^{210}Pb, radioactive decay reduces levels of excess ^{210}Pb over time, and thus older sediments which are more deeply buried will have lower ^{210}Pb abundances (Appleby and Oldfield, 1992). Following exponential decay (half-life of 22.3 years), these excess ^{210}Pb values are reduced to background values over ∼110 years (i.e. 5 half-lives). This decay curve of the excess ^{210}Pb over depth is used to establish a sediment accumulation rate. Measuring ^{210}Pb can be done via either alpha or gamma spectrometry. Both are used in this study, where alpha spectrometry is destructive and gamma spectrometry is quick and non-destructive. Only hemipelagic muds are sampled for analysis, as the constant-flux, constant-sedimentation (CF-CS) model that was used assumes a constant sediment accumulation rate. The straight line fit of the natural logarithm of the excess activity is used to determine the sediment accumulation rate.

The ^{210}Pb method is seen to be effective because an additional, independent geochronometer (^{137}Cs) is used to corroborate the results. Elevated ^{137}Cs levels are caused by atmospheric nuclear testing from 1952-1963, which reached a peak in 1963 before the Partial Test Ban Treaty came into force (Ritchie and McHenry, 1990). Levels of ^{137}Cs have since remained elevated, although oceanic processes have become more important (Hirose and Aoyama, 2003). The first appearance of ^{137}Cs indicates a probable age of ∼1954 (Appleby and Oldfield, 1992). The observation of a peak indicates ∼1963. The ^{137}Cs activity can thus be used as marker horizons, with 1954 or 1963 as reference dates. Based on these marker horizons, a crude estimate for sediment accumulation rates can be made to corroborate ^{210}Pb results.

Both ^{210}Pb and ^{137}Cs analysis assume that turbidity current erosion and deposition are insignificant in the sediment cores, as constant sedimentation is assumed. Therefore, the accumulation rates are corrected for by removing the (instantaneously deposited) sand layers, to obtain a sediment accumulation rate with an event-free depth, i.e. without turbidity current deposits, following Stacey et al. (2019). Here, any layers coarser grained than silty mud are considered event deposits. Thick and coarse-grained events are considered large events, following the suspension criterion (Komar, 1985). It is assumed that mud layers are hemipelagic, which is not necessarily the case. Furthermore, it is not possible to account for erosion of sediments, which could lead to hiatuses in the cores.

In total, six cores were analysed, located on the delta, upper and lower channel and the deep basin. One of the piston cores (04-PC), located on the delta, was only analysed for ^{137}Cs, as it lacked sufficient hemipelagic sediment for background sedimentation analysis, and can thus only give indication of post-1954 deposition. The remaining five piston cores were analysed as well via gamma and/or alpha ^{210}Pb. See Fig. 4.10 for sample numbers and depths.

4.5.4 Event frequency calculations

Event frequencies are subsequently estimated based on two methods. The first method is based on the ADCP data, and the second method is based on sediment accumulation rates and core logs. The ADCP data directly record event occurrence during periods of a few months over recent years. Sediment accumulation rates then provide frequencies for event deposits over longer periods, up to several hundred years. For this method, the calculated background sediment accumulation rate, which is applied to the entire sampled depth, is combined with the logged sediment flow deposits. In some cases, cores recorded multiple types of event deposits, such as thinner and finer-grained or thicker and coarser grained event deposits. In such cases, two frequencies were calculated for the different event types.

4.6 Results

The direct measurements, sediment cores and sediment accumulation rate analysis are discussed separately, following the five morphological zones in Bute Inlet. These morphological zones are, from proximal to distal; the delta, upper and lower channel, the channel-lobe-complex, and finally the deep basin zone (Fig. 4.1).

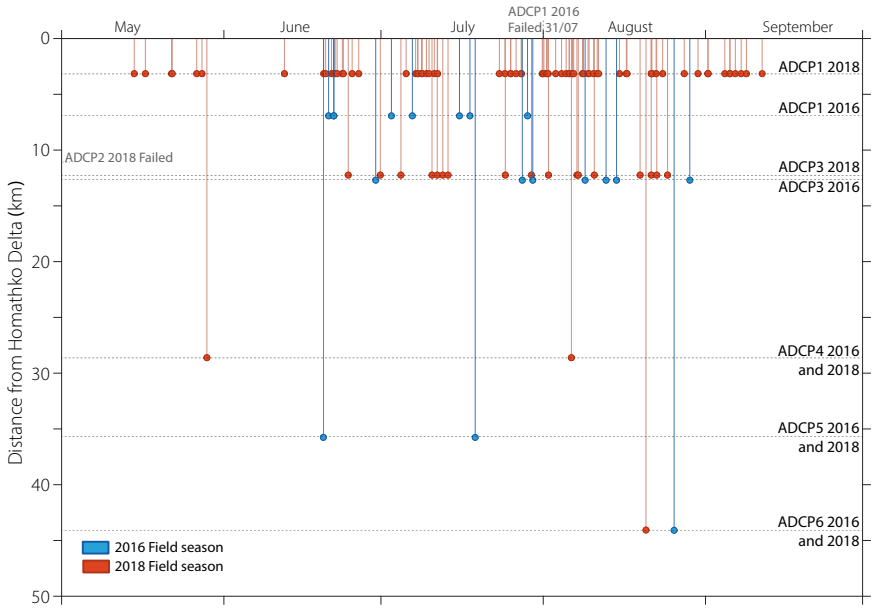

FIGURE 4.2: Timing and run-out distance of submarine events in Bute Inlet, measured over two field seasons in 2016 (blue lines) and 2018 (red lines). Each line represents an individual event and its runout length. Months are indicated at the top, mooring locations are indicated on the right, and distance from Homathko Delta shown on the left. During the 2016 field season, the first mooring (ADCP1 2016) failed after the end of July. In 2018, the first mooring (ADCP1 2018) was placed 2.5 km further upstream, whilst the third mooring (ADCP3 2018) was moved 350m upstream. ADCP2 failed in 2018.

4.6.1 Direct measurements

The greatest turbidity current activity was measured at the most proximal mooring in the delta morphological zone in both 2016 and 2018. In the 2016 field season, the first ADCP failed late July. Up to then, 13 events were recorded at the first ADCP (Fig. 4.2). The two ADCPs in the upper channel both measured 10 events, five of which were recorded after the first mooring failed. These five events are assumed to have been generated upstream of ADCP 1. Thus, 18 events occurred on the delta in 2016, and 8 of these events died out before the second mooring, located 7 km further down-channel (Fig. 4.2). Only three events are recorded beyond the upper channel zone. ADCP 5, located 7 km further downstream from ADCP 4, is the final measurement of two events. One event was measured at the final mooring station on the channel-lobe-complex (Fig. 4.2). In 2018, 95 events were recorded by the first ADCP. The second mooring failed, but the third mooring recorded 21 of the original 95 events. Again, only three events are recorded beyond the upper channel zone. In 2018, ADCP 4 is the final measurement of two events, 30 km from the delta. Only one event is measured at both ADCP 5 and 6, running out to the channel-lobe-complex (Fig. 4.2). The ADCPs provide detailed data over two field seasons, at set

distances along the channelized system. Therefore, flow frequency calculations based on the ADCP data might appear discrete, but is likely to be present a continuous flow frequency pattern.

4.6.2 Sediment cores

The sediment cores are described according to morphological zone. Fig. 4.3 shows the delta; Figs. 4.4-4.6 the upper channel; Fig. 4.7 the lower channel; and Figs. 4.8 and 4.9 show the channel-lobe-complex and deep basin respectively.

4.6.2.1 Delta

The majority of sediment cores collected in the delta morphological zone were taken along transect AA', aligned with ADCP 1 from 2016 (Fig. 4.3). The sediment cores closest to the thalweg (01-PC, 02, 03-BC) show thick sands, with grain sizes up to 2 mm. The two box cores show that the top layer in the thalweg consists of silty mud. At 2 m above, and 170 m outside the main thalweg, two sediment cores (04-PC, 05-BC) show thin alternations of sand and silty mud. The sand grain size varies between fine to very coarse (up to 2 mm). Nearly 40 m above, and 340 m outside the thalweg, mud deposition prevails as shown in 06-BC. 300 m down-channel from transect AA', two sediment cores 15 m above the thalweg (07-PC, 08-BC) show frequent mud and thin sand alternations, with grain sizes up to 375 μm.

4.6.2.2 Upper channel

In the upper channel morphological zone, there are two areas with multiple sediment cores (Fig. 4.4): the knickpoint area, where two ADCPs tracked a major knickpoint feature, and a terraced sequence located ∼1.5 km down-channel from the knickpoint. The thalweg in the knickpoint area has eight sediment cores of which seven are box cores (transect BB'; Fig. 4.5). These sediment cores show that the thalweg consists predominantly of thick sands with grain sizes up to 2 mm, often with a thin mud cap. Just outside the thalweg, four further sediment cores were recovered from the inner terrace. 9-PC is located 25 m above the thalweg, and shows predominantly mud, with sand alternations. This nearly eight-metre long piston core shows three thicker (>10 cm) sand horizons. The other two piston cores (13 and 18-PC) show even thicker sand deposits, up to 45 cm thick. Yet, the box core next to 18-PC shows

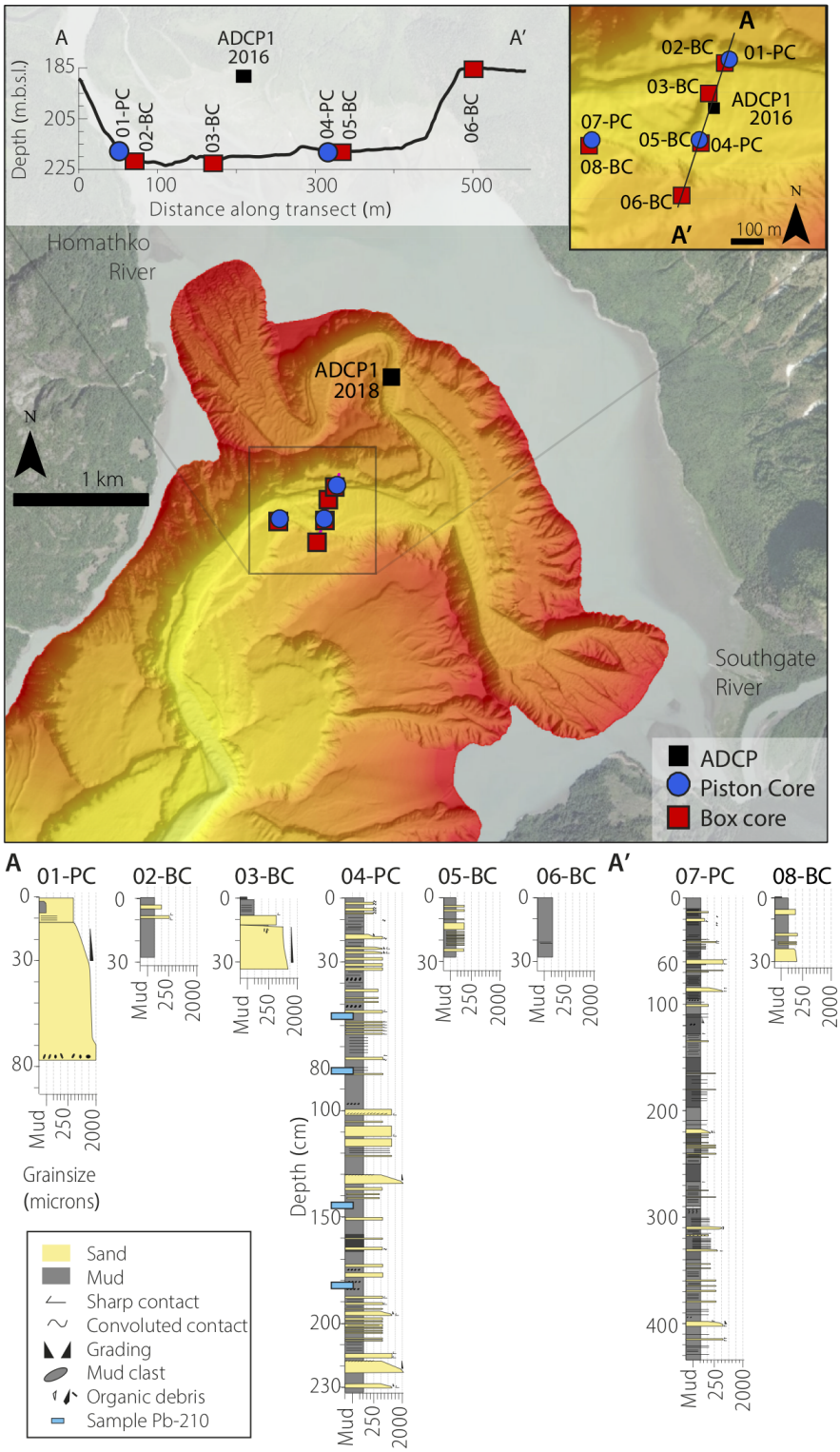

FIGURE 4.3: Delta morphological zone. Transect AA' is north to south, aligned to ADCP1 deployed in 2016 (see inset top right). The inset top left shows the channel profile along AA' and core locations. Core 04-PC also includes sample depths for analysis on sediment accumulation rates (blue rectangles). On the right, the two down-channel cores (07, 08) are shown. Note, vertical scales for core logs are not all the same. Colour scale of bathymetry is displayed in Fig. 4.1.

silty mud (19-BC; Fig. 4.5). The terraced sequence includes four sediment cores (23-BC, 24-26 PC, transect CC', Fig. 4.6). With each terrace above the main thalweg, the sediment cores become more dominated by mud deposits, with fewer sand layers. Still, the sediment core located furthest above the main thalweg (26-PC) has a distinct coarse-grained (1 mm) fining upward sand deposit (Fig. 4.6).

4.6.2.3 Lower channel

Two transects of sediment cores were collected from the lower channel morphological zone (Fig. 4.7). Transect DD' is aligned along ADCP 4, at ∼30 km down-channel from the Homathko Delta, and includes five sediment cores. Sediment cores both inside and 10-15 m above the thalweg show thick sand deposits, with typical sand grain sizes around 250 μm, reaching up to 2 mm (Fig. 4.7). A single piston core, 32-PC, is located 1.1 km down channel from the DD' transect. This piston core from the terrace again shows thick sand deposits (up to 50 cm), with grain sizes of up to 500 μm. Transect EE', along ADCP 5, includes four sediment cores. Similar to the sediment cores in transect DD', coarse-grained sand deposits are found both on the terrace and thalweg. In the thalweg (34-BC), a thick sand deposit with a thin mud cap was recovered, similar to the thalweg box core at transect DD'. An attempt to obtain a piston core from the thalweg failed. On the terrace, sand deposits reach 1 mm grain size, and mud deposits become more prominent (Fig. 4.7).

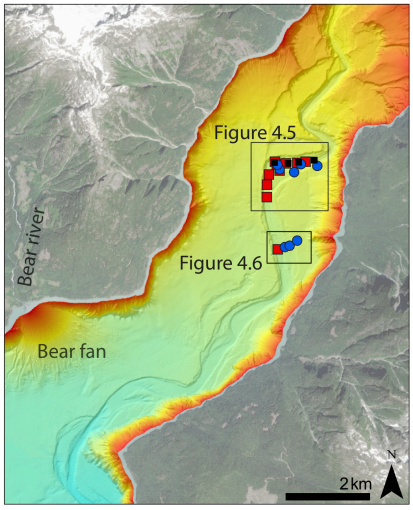

FIGURE 4.4: Upper channel morphological zone. The complicated geometry in this morphological zone includes multiple terrace levels. Two areas are highlighted, the main knickpoint zone (see Fig. 4.5) and a multi-terraced zone (see Fig. 4.6). Colour scale of depth is displayed in Fig. 4.1.

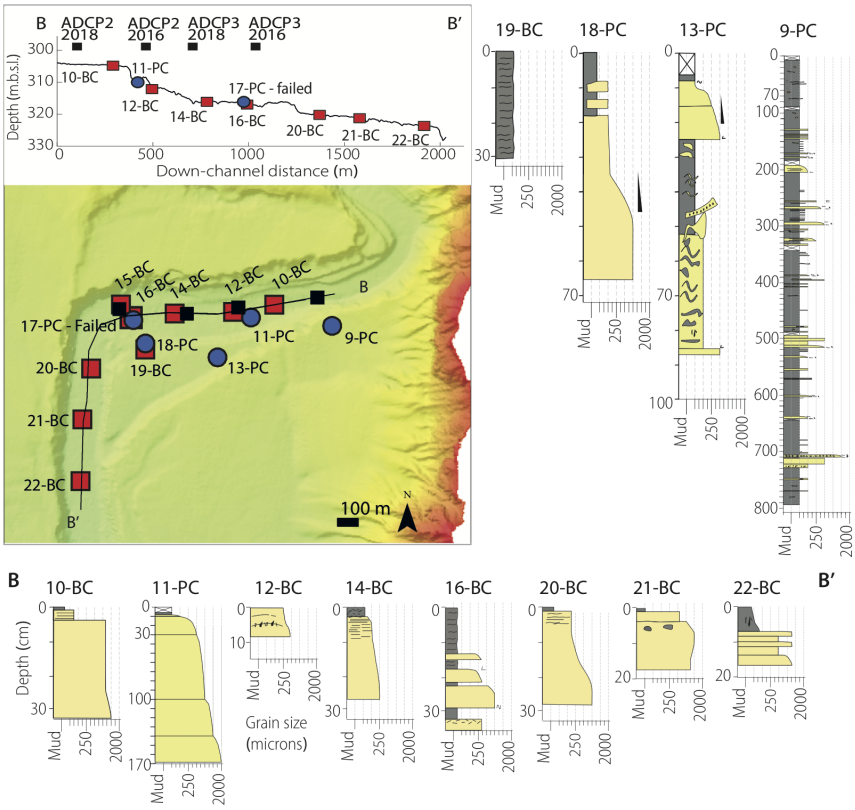

FIGURE 4.5: Knickpoint area in the upper channel morphological zone. Transect BB' is along the thalweg, inset shows transect profile and core locations. BB' core logs are displayed below. On the right are the inner bend core logs. Colour scale of bathymetry is displayed in Fig. 4.1; core log key in Fig. 4.3.

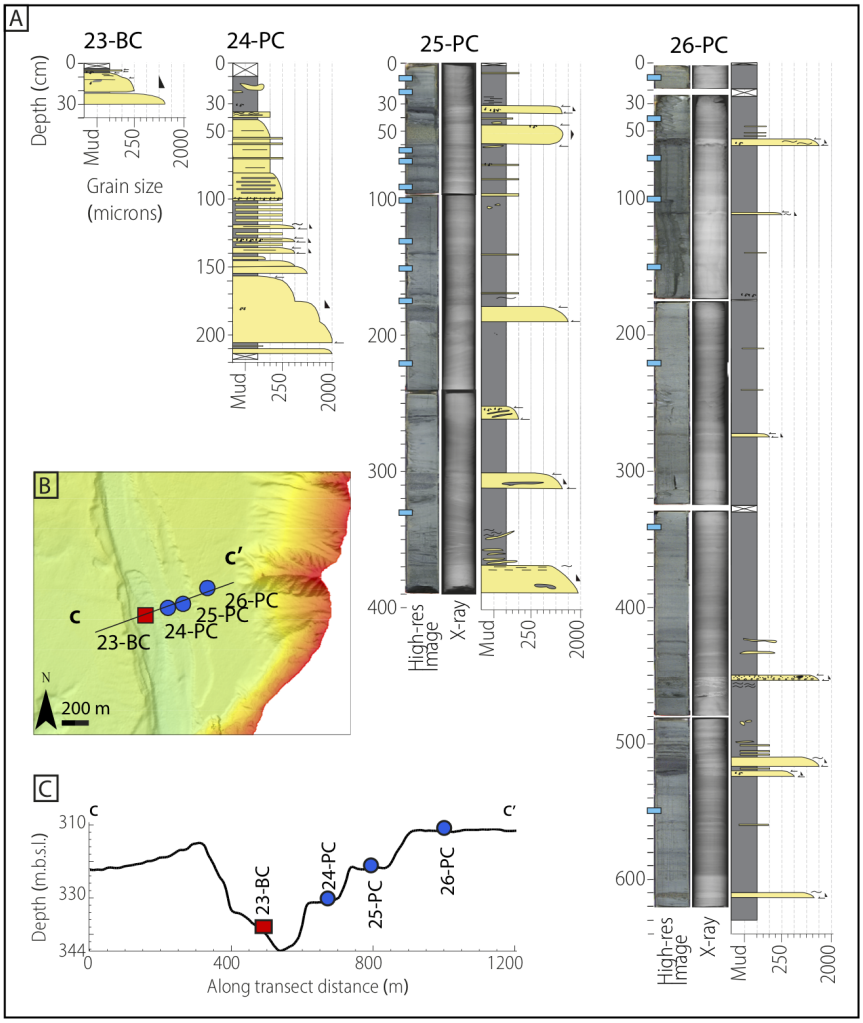

FIGURE 4.6: Upper channel morphological zone, terraced sequence. A) Core logs. Sample depths used for sediment accumulation rate analysis are indicated on 25-PC and 26-PC, and X-radiographs and high-resolution images are included. Core log key in Fig. 4.3. B) Shows detailed bathymetry map, Colour scale of bathymetry is displayed in Fig. 4.1. C) Profile of the channel with core locations.

FIGURE 4.7 *(next page)*: Lower channel morphological zone, which includes a single terrace. There are two transects with cores aligned with ADCP 4 and 5. Insets show detailed profile of channel with core locations. Transect DD', along ADCP4, includes five core logs of which 27-PC is subsampled for sediment accumulation rates. Transect EE' is along ADCP5 and includes 4 core logs. 32-PC is a single core ca. 1km downstream from transect DD'. Colour scale of bathymetry is displayed in Fig. 4.1; core log key in Fig. 4.3.

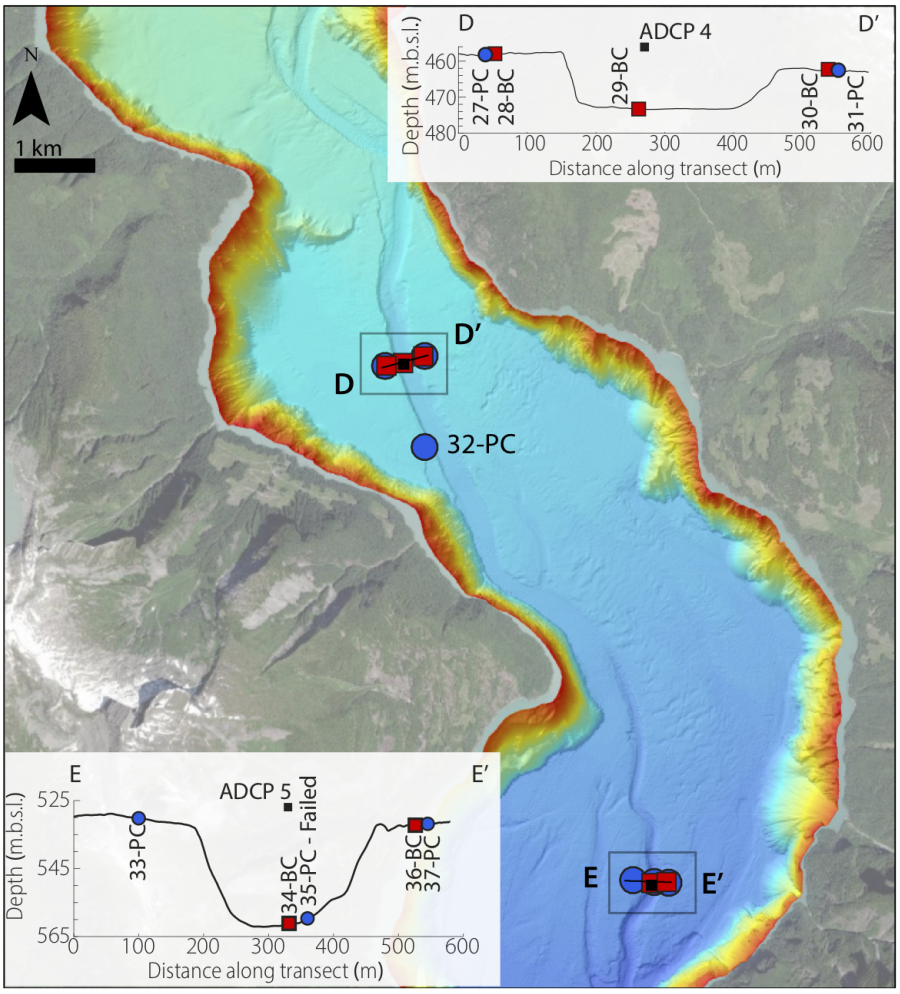
N
1 km
D
D′
ADCP 4
Depth (m.b.s.l.)
460
470
480
0
100
200
300
400
500
600
Distance along transect (m)
27-PC
28-BC
29-BC
30-BC
31-PC
D
D′
32-PC
E
E′
ADCP 5 - Failed
525
545
565
33-PC
34-BC
35-PC - Failed
36-BC
37-PC
E
E′

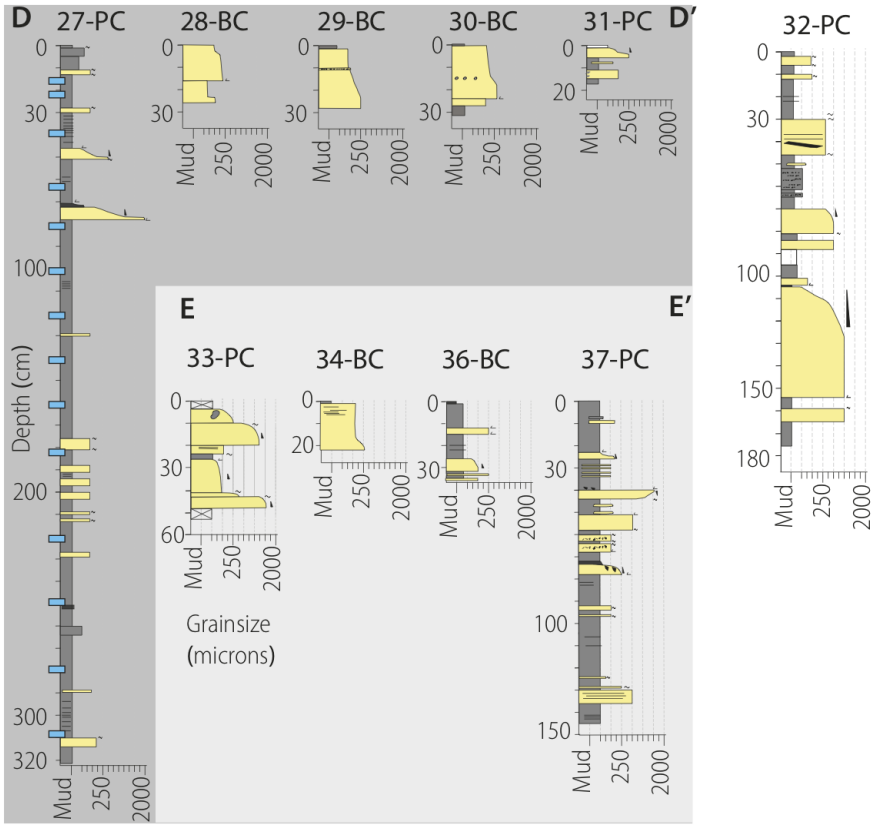
D
27-PC
28-BC
29-BC
30-BC
31-PC
D′
32-PC
Depth (cm)
0
30
100
200
300
320
Mud
250
2000
E
E′
33-PC
34-BC
36-BC
37-PC
60
20
150
180
Grainsize
(microns)

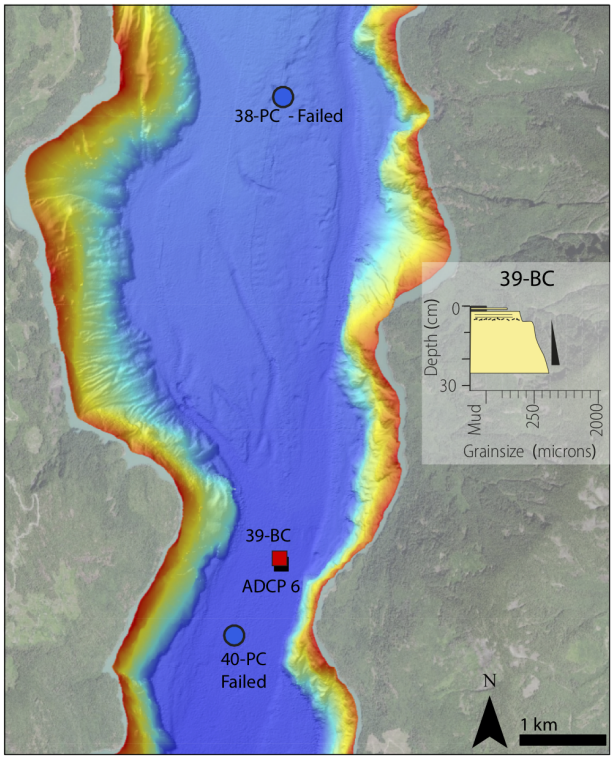

FIGURE 4.8: Channel-lobe-complex morphological zone. Only the box core near ADCP 6 was successful. Colour scale of bathymetry is displayed in Fig. 4.1; core log key in Fig. 4.3.

4.6.2.4 Channel-lobe-complex

Only one sediment core was successfully retrieved from the channel-lobe-complex zone (Fig. 4.8). Two piston cores (38 and 40-PC) failed. The box core (39-BC) taken near ADCP 6 shows a thick sand deposit with a grain size up to 375 μm, and a thin mud cap.

4.6.2.5 Deep basin

A total of 10 piston cores were recovered from the deep basin (Fig. 4.9). Nearer the channel-lobe-complex, these are shorter (around 50 cm), but more distally these piston cores extend to 8 m. The grain size in all distal piston cores rarely exceeds 375 μm. 41-46 PC all show mud and sand deposits in the upper 50 cm. The sand deposits vary in thickness, but are most often >10 cm. 47-PC has a thick layer of organic matter near its surface. 48-50 PC all show 150-250 cm thick mud deposits at the top of the core, above substantial sand deposits. The thickness of the bottom sand layer in 46, 47 and 48-PC is possibly exaggerated. Additional suctioning of sand from

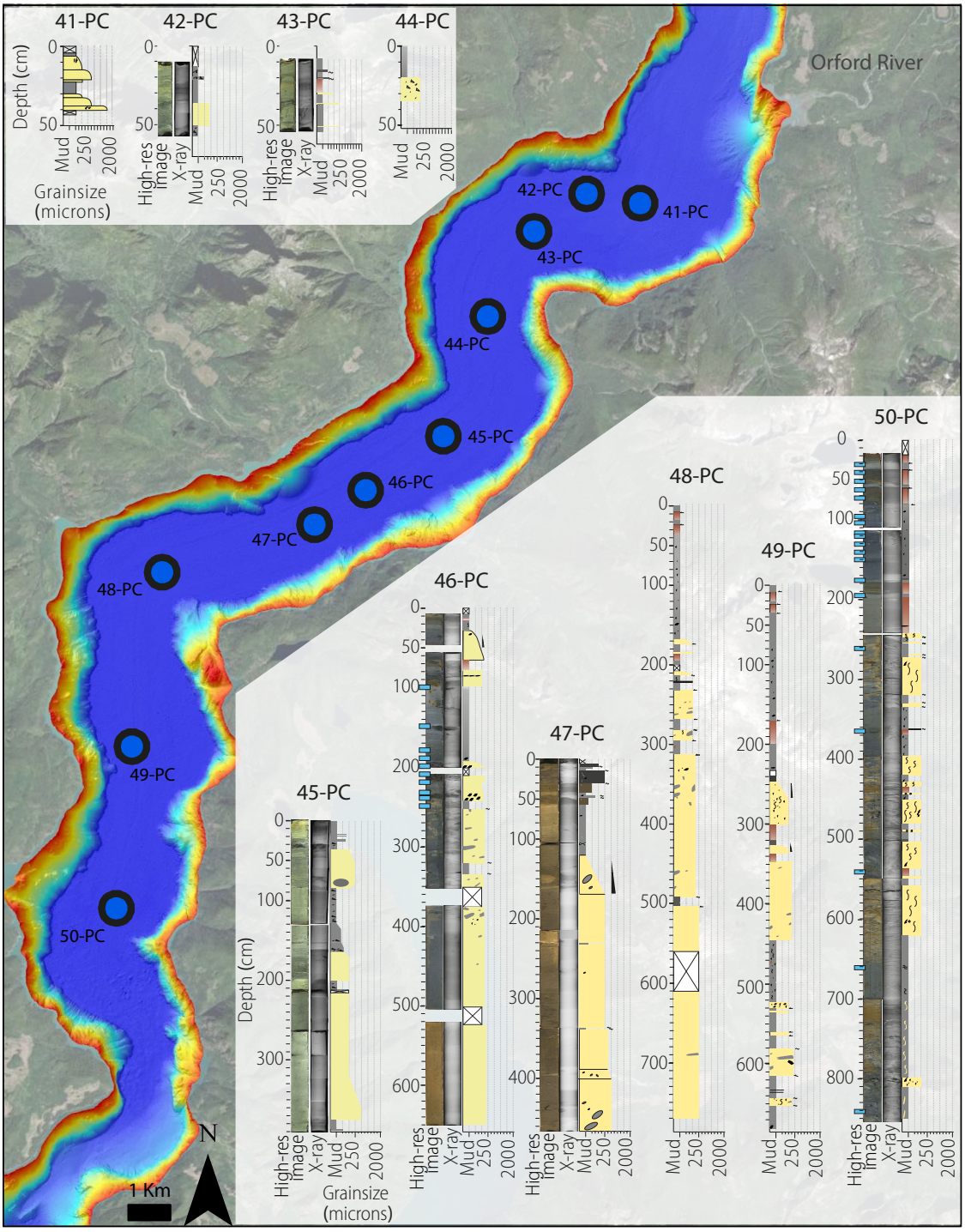

FIGURE 4.9: Deep basin morphological zone. There is a total of 10 piston cores, six include X-radiographs and high-resolution images. 46-PC and 50-PC have been subsampled for sediment accumulation rate analysis. Colour scale of bathymetry is displayed in Fig. 4.1; core log key in Fig. 4.3.

surrounding sand layers during extraction cannot be ruled out due to a lack of mud cap (i.e. Stow and Aksu, 1978). Furthermore, 47-PC was reportedly unconsolidated and post-recovery deformation is possible (Pers. comm. C. Stacey, scientist onboard CCGS Vector during recovery).

4.6.3 Sediment accumulation rates and age dating

Five piston cores were analysed for sediment accumulation rates using ^{210}Pb, and a sixth piston core was analysed for ^{137}Cs only (Table 4.2). The data will be discussed according to distance from the Homathko Delta.

The piston core from the delta (04-PC) was analysed for ^{137}Cs only, due to the dominant presence of sand horizons (Figs. 4.3 and 4.10A). The results show ^{137}Cs activity at all sampled depths, suggesting post-1954 deposition of at least the upper 181 cm (Fig. 4.10A). Event-free depth calculations, removing all layers coarser than silty mud, suggest a minimum sediment accumulation rate of 2.3 cm yr^{-1} (Table 4.2). However, as there are no ^{210}Pb measurements to validate the ^{137}Cs results, the calculated accumulation rate can merely be used as a guideline.

In the upper channel morphological zone, two terrace sediment cores were analysed (25, 26-PC; Fig. 4.5). 25-PC is located on the middle terrace. The ^{137}Cs activity suggests an approximate accumulation rate of 1.7 cm yr^{-1} (Table 4.2). The ^{210}Pb-derived accumulation rates are lower, at 0.9 $\pm$ 0.2 (alpha) and 1.2 $\pm$ 0.2 (gamma) cm yr^{-1} (Fig. 4.10B; Table 4.2). Possible explanations for the offset between the ^{210}Pb and ^{137}Cs results include a systemic change in the ^{210}Pb supply rate, singular events such as sidewall slumping, a hiatus in the sediment record, or post-depositional redistribution of either ^{137}Cs or ^{210}Pb due to remobilisation (Benoit and Rozan, 2001, Arnaud et al., 2006, Appleby, 2013). Combining the accumulation rates with core logs, an event frequency can be established. Within the sample depth (330cm), a total of 12 events are logged, which includes all sandy events (i.e. grain sizes greater than the background silty muds). Four of these 12 events are more substantial, with a coarse-grained and thick (>5cm) deposit (Figs. 4.5 and 4.10B). For the ^{210}Pb results, this equates to an event every 22 $\pm$ 3 years, increasing to every 65 $\pm$ 11 years for coarse-grained events only (Table 4.2). The ^{137}Cs results suggest a recurrence interval of every 13 years, increasing to every 40 years based on large events only.

TABLE 4.2: Bute Inlet event frequencies based on the sediment accumulation rates.

Morphological Zone		Delta	Upper Channel	Upper Channel	Lower Channel	Deep Basin	Deep Basin
Piston Core no.		04-PC	25-PC	26-PC	27-PC	46-PC	50-PC
Core log events within sampling depth		34	12 (>5cm: 4)	6	13	2	240cm*
Cs-137	1963 assumed event free depth (cm)	144	76	Abnormal Cs137 data. Not usable	36	34	52
	Estimated accumulation rate (cm/yr)	2.3	1.7		0.8	0.6	1.1
	Event Frequency (Years)	N/A	13 (40)		28	35cm event emplaced in last ~55 years	218*
Gamma Pb-210	Accumulation rate (cm/yr)	No data	1.2	Abnormal Pb210 data. Not usable	0.9	Not enough data points to establish Pb-210 excess	0.9
	Error		0.2		0.3		0.1
	Event Frequency (Years)		19 (57)		25		258*
Alpha Pb-210	Accumulation rate (cm/yr)		0.9	1.6^	No data		1
	Error		0.2	0.2			0
	Event Frequency (Years)		25 (76)	n/a			250 *

* For distal core it is the depth of sand horizons first seen

^ These results are not used further, based on other data discrepancies in core

26- PC is located on the highest terrace, one terrace above 25- PC. Figure 4.10C shows that the gamma activity measurements (^{137}Cs and ^{210}Pb), do not show the expected activity dependency with depth. Background levels of ^{137}Cs have remained elevated since 1954 (Hirose and Aoyama, 2003), thus the lack of activity in the shallower samples suggests the results are unsuitable for further analysis. The gamma ^{210}Pb also shows a kick, disrupting the exponential decay curve, and is not analysed further. Interestingly, the alpha spectrometry for ^{210}Pb actually displays a classic exponential decay curve, with a calculated sediment accumulation rate of 1.6 ± 0.2 cm yr^{-1} (Fig. 4.10C; Table 4.2) Although this accumulation rate roughly agrees with 25-PC on the lower terrace, based on the overall inconsistencies in these data, an accumulation rate cannot be established with certainty. The data in this core underpin the necessity to combine ^{137}Cs and ^{210}Pb data to establish accumulation rates.

FIGURE 4.10 *(next page)*: Sedimentation rates and ^{137}Cs activity alongside core logs, and where available high-resolution images and x-radiographs. Gamma and alpha spectrometry sedimentation rates are given where calculated in respective colours. Open symbols indicate the samples used for sediment accumulation rate calculations. The sample depth assumed for 1954 peak ^{137}Cs activity is indicated with † symbol. The key for the core logs is displayed in Fig. 4.3. A) 04-PC in the delta is only analysed for ^{137}Cs activity. B-D) Piston cores in the mid-channel section. E, F) Piston cores in the deep basin.

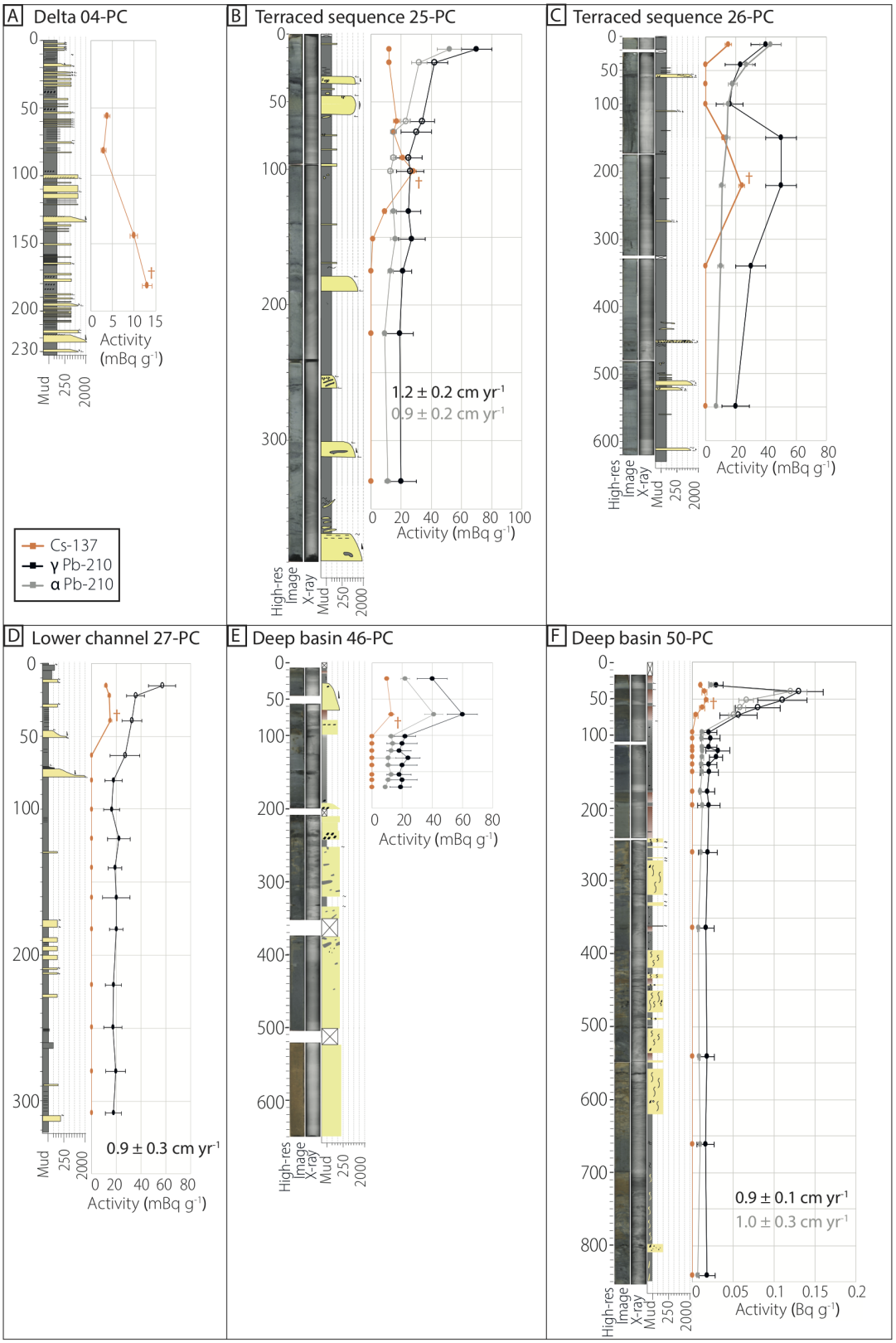
A Delta 04-PC
B Terraced sequence 25-PC
C Terraced sequence 26-PC
D Lower channel 27-PC
E Deep basin 46-PC
F Deep basin 50-PC
Cs-137
γ Pb-210
α Pb-210
1.2 ± 0.2 cm yr⁻¹
0.9 ± 0.2 cm yr⁻¹
0.9 ± 0.3 cm yr⁻¹
0.9 ± 0.1 cm yr⁻¹
1.0 ± 0.3 cm yr⁻¹
Activity (mBq g⁻¹)
Activity (Bq g⁻¹)
High-res Image
X-ray
Mud
250
2000

In the lower channel, 27-PC on the terrace near ADCP 4, returned 0.9 ± 0.3 cm yr^{-1} for ^{210}Pb (Gamma spectrometry only; Fig. 4.10D; Table 4.2). The ^{137}Cs data displays a peak level of activity, but lacks a sample showing the sharp rise to a high peak in activity representative of the onset of the ^{137}Cs activity. ^{137}Cs sediment accumulation rate is estimated at 0.8 cm yr^{-1}, and is thus in agreement with the calculated ^{210}Pb sediment accumulation rate. There is a total of 13 events visible in the core log, suggesting a frequency of one event every ∼25 years (Table 4.2). There is no further distinction of event magnitude in this core log.

Two piston cores are located in the deep basin (46-PC and 50-PC, Fig. 4.9). Core 46-PC did not include enough ^{210}Pb measurements in the excess activity to establish an exponential decay curve (Fig. 4.10E). ^{137}Cs activity in the top two samples suggests post-1954 deposition, therefore a minimum sedimentation rate of 0.6 cm yr^{-1}. The 35 cm thick sand deposit in core 46-PC, from 30-65 cm depth, has been deposited in the last ∼55 years. 50-PC, the most distal core in the deep basin, has ^{210}Pb sediment accumulation rates of 0.9 ± 0.1 (gamma) to 1.0 ± 0.3 (alpha) cm yr^{-1} (Fig. 4.10F; Table 4.2). ^{137}Cs activity suggests a sediment accumulation rate of 1.1 cm yr^{-1}. There are no events in the top of the sediment core, but from 2.40 m depth multiple thick sand beds are logged, corresponding to 218-258 years ago.

4.7 Discussion

The overarching aim is to understand the spatial and temporal scale of turbidity current activity on a source-to-sink scale. First, we discuss the frequency and magnitude of events in Bute Inlet and, second, explore possible origins of the observed event scales. Third, we compare event frequency and magnitude over distance in Bute Inlet to the nearby submarine system in Howe Sound, where suitably detailed information on event frequency, magnitude and runout is available (Stacey et al., 2019).

4.7.1 How many event frequencies are observed in Bute Inlet?

By combining the depositional records, the sediment accumulation rates and the direct measurements, we can establish the frequency and magnitude of events in Bute Inlet on short and longer timescales (Fig. 4.11A). We find three categories of event frequencies.

On short time scales, we see high frequency events. Near the Homathko and South-

gate Deltas, ADCP 1 measured ca. 100 of events annually (Fig. 4.2). Additionally, the combination of accumulation rates and core logs suggest high activity near the delta. The sediments show the presence of ^{137}Cs at 1.8 m depth, suggesting very rapid sediment accumulation rates. The deposits are composed of thin mud and sand alternating layers, indicating frequent turbidity currents occurring near the deltas (Fig. 4.3). With distance, the frequency of events declines. In the upper channel zone, ADCP 2 and 3 only record ∼20 events per year. More distally, ADCP measured frequency declines to 3 events per field season in the lower channel (Fig. 4.2). Thalweg deposits in the upper and lower channel predominantly consist of thicker sands. The channel-lobe-complex experiences only one event per field season. The single successful box core on the lobe shows thick sand deposits. The two failed piston cores suggest sand is predominant elsewhere on the lobe too, although coring via vibro-coring is necessary to confirm sediment sequences. This suggests that events on the lobe are solely deposited here, with the lobe forming the final depositional area for most turbidity currents.

The terraces are underlain by sandy deposits, with a grain size reaching 2 mm, and thicknesses around 5-10 cm (Figs. 4.5-4.7). These coarse-grained deposits require events with high-energy in order to deposit sands ∼15 m above the current-day thalweg. Two piston cores on the terraces, 25 and 27-PC, were successfully analysed for sediment accumulation rates. 25-PC is located in the upper channel on a secondary terrace at 22 m above the current-day channel. This piston core returned a recurrence interval of 15-20 years for the recorded events. 27-PC is located 14 km down-channel from 25-PC. This core in the lower channel is on a terrace 15 m above the current-day channel, and found an event frequency of 1 every 25 years. Thus, intermediate frequency events, occurring every ∼20 years, are recorded on the terraces.

Beyond the channelized system, the deep basin shows that near-surface sandy layers pinch out over distance, and near-surface mud layers become predominant (Fig. 4.9). Two deep basin cores were analysed for sediment accumulation rates. 46-PC shows a 35 cm thick fining upward sequence, deposited in the last ∼55 years. More distal cores show extensive mud layers prevail near the top, with >1.5 m thickness. The most distal core shows that the last thick sand deposit was ca. 240 years ago. We regard these thick sand layers as records of mega-events, low frequency with high energy, resulting in these thick sand deposits. This alternation between quiescent and active periods in the deep basin occurs on time scales beyond the direct monitoring range (i.e. $\gg$ 1 year).

Although our observations show there are three event categories, there is a possibility

that results appear as discrete categories, merely due to observation methods (e.g. moorings at discrete distances). For example, Prior et al. (1987) previously recognised annual events, similar to the high frequency events recorded by the direct monitoring in this study. Based on their direct monitoring data, Prior et al. distinguished two discrete flow categories: frequent low velocity flow versus infrequent large-scale events. The more detailed data in this study suggests a more continuous scale of activity of modern-day turbidity currents, with a gradual decline in activity away from the deltas. For now, there is not sufficient data (e.g. from more closely spaced moorings) available to bridge the gap between the three event categories identified here. However, these events in Bute Inlet could potentially form a single continuous magnitude-frequency distribution.

4.7.2 What is the origins of these different event frequencies?

Here, we discuss the possible emplacement mechanisms of the three different event frequencies found, and thus what determines the different event frequency and magnitudes found.

4.7.2.1 High frequency events

The smaller-scale events in Bute Inlet were previously recognised by (Prior et al., 1987, Bornhold et al., 1994), and are triggered during the yearly freshet season. During this period, the elevated river discharge supplies large volumes of sediment to the Homathko and Southgate Deltas. The rapid deposition of this sediment accompanied by tidal forcing is likely responsible for the triggering of these smaller magnitude events, as has been found in the nearby Squamish Delta (Clare et al., 2016, Hizzett et al., 2018, Hage et al., 2019). The subsequent run-out of events in Bute Inlet is unlikely to be controlled by channel width and slope, as these parameters remain relatively constant over distance (Fig. 4.1). Heerema et al. (2020) found that the initial velocity of events dictates the subsequent runout length of events at other field sites, and a similar relation may hold in Bute Inlet. More powerful events have the ability to accelerate and ignite, and run out over greater distances.

These high frequency events barely exceed the moored height of the ADCPs at ∼20 m above the thalweg (Pope et al., in prep), and are therefore unlikely to deposit sands on the terraces. Additionally, the events that reached the lobe were rapidly dissipating (Chen et al., in prep). The events directly measured by ADCPs in Bute

Inlet are thus high frequency, but low magnitude events. The frequency ranges from 100s events up to 7km from the delta, to one event that manages to runout >40 km to the lobe.

4.7.2.2 Intermediate frequency events

These events are recorded by sand layers on the terraces outside the channel, and occur every ∼20 years. The emplacement of these intermediate event deposits can originate from a variety of mechanisms, three of which are explored here.

A first possible mechanism causing the intermediate scale deposits is channel sidewall collapse, which can lead to increased local sediment input. The erroneous sediment accumulation rate, specifically the ^{137}Cs activity, for the top terrace (26-PC, Fig. 4.10C) could be due to an influx of re-worked sediments. However, most deposits show a fining upward sequence, making sidewall collapse less likely, as this will not allow for sediment sorting and grading.

Second, it could be assumed the modern-day thalweg-to-terrace height difference (∼20 m) is roughly constant through time, and thus representative of the height difference during the event deposition. These events could be due to increased river discharge, as seen in the high frequency events. However, the discharge needs to be considerably higher to overcome the height difference between terrace and thalweg. A peak discharge of ∼2500 m^3 s^{-1} is calculated for a 20-year return period (`https://wateroffice.ec.gc.ca/index_e.html`).

Third, migration of knickpoints may significantly change the height difference between channel floor and terrace, and thus influencing the frequency of terrace deposits. Heijnen et al. (2020) shows that Bute Inlet experiences rapid (100-450 m yr^{-1}) upstream migration of multiple knickpoints, which are steep steps in the thalweg. Such knickpoints thereby excavate the channel thalweg, and will cause changes in the height of terraces above the channel floor. Prior to knickpoint erosion, the channel will experience gradual fill from turbidity current deposits, such that the thalweg will be relatively shallow in comparison to the terraces. A migrating knickpoint varies in height, but can reach up to 30 m. Therefore, the thalweg-to-terrace height difference could temporarily be small or zero, before passage of a knickpoint causes a much greater height difference.

It is possible to estimate the time scales over which knickpoints may change the terrace-channel floor height difference, and thus deposits on terraces. A location along the Bute Inlet channel can experience a migrating knickpoint every ca. 15

years, based on channel length, knickpoint migration rate and number of knickpoints. This period of 15 years is similar to the frequency of intermediate event deposits on terraces, which occur every ∼20 years. Thus, for this third proposed mechanism the event frequency would predominantly be regulated by the channel geometry, and to a lesser extent by the flow magnitude.

4.7.2.3 Low frequency events

The low frequency event deposits in the deep basin can originate from a diverse array of processes. Three processes are suggested here. First, these large (thick) events can originate from the Orford River rather than from the Homathko and Southgate Rivers. The Orford River enters Bute Inlet just downstream of the channel-lobe-complex (Figs. 4.1, 4.9). Although the Orford River can generate an additional influx of sediment, this river is considerably smaller than the Homathko and Southgate Rivers. The Orford River would need considerable increased river discharge levels and sediment load to lead to these thick sand deposits in the deep basin, making this a less likely source for the low frequency events.

Second, the sandy deposits could originate from the Homathko Delta, where during exceptional event magnitudes, turbidity currents may reach the lobe and continue along the flat deep basin. These events could be triggered by for instance glacial lake outburst floods, or exceptionally high river discharge levels. These large events could lead to conduit flushing of the systems, where the event would cannibalise previous deposits (Piper and Normark, 2009). This would suggest events in Bute Inlet are subdivided in two categories, with local, smaller events leading to infill of the submarine system, and large-scale events running through the entire system and flushing it of previous sandy deposits. Thereby, the large-scale events would lead to thick, distal, sand deposits, preserved over longer timescales. This would explain why the deposits in the deep basin likely exceed the possible volume carried in a single river flood, as previous channel filling deposits are eroded and incorporated in a larger event (Piper and Normark, 2009).

Third, similar thick sandy deposits have been found in Howe Sound, with a recurrence interval of ca. 100 years (Stacey et al., 2019). Regional triggers such as earthquakes could lead to synchronous turbidity currents or simultaneous fjord sidewall collapse (i.e. Goldfinger et al., 2007), although additional local controls such as sediment supply can lead to differentiation between the two submarine systems (Pope et al., 2017). Other large-scale, system-wide, changes such as sea level change are less likely

due to the relatively short timescales (∼200 years) over which the events took place. The origins of these low frequency events remain speculative, and more research into the provenance of these sediments is required.

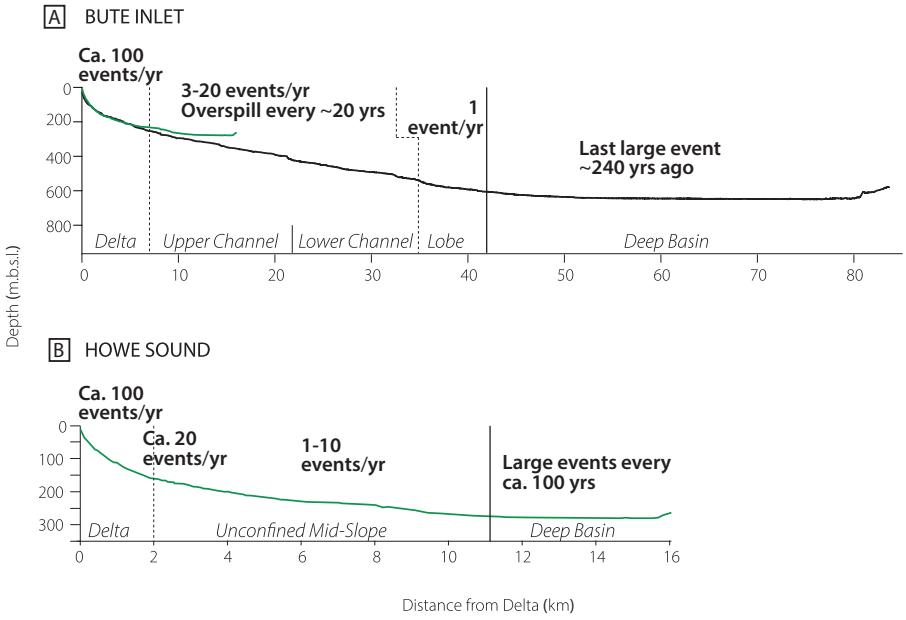

FIGURE 4.11: Synopsis of turbidity current event frequencies in fjords. A) Event frequencies found in Bute Inlet. B) Event frequencies found in Howe Sound (Stacey et al., 2019). Both transects show a vertical black line, which indicates the division between the low magnitude events and the high magnitude events in the deep basin. Note that the length and depth scale between A and B is different. The superimposed green line at A is the Howe Sound transect according to scale. Data in both instances is based on a combination of direct measurements and core log analysis.

4.7.3 How do the event frequency and magnitude over distance in Bute Inlet compare to the nearby Howe Sound fjord?

The frequency-magnitude relationship found in Bute Inlet is now compared to another location, to see if general patterns emerge. There are limited field sites in which there is a good understanding on the frequency over their potential runout distance of turbidity currents especially across a full source-to-sink scale. Moreover, not many field sites have both detailed monitoring data and long-term sediment core records. We are aware of only one such location, the nearby channelized fjord Howe Sound, British Columbia (Fig. 4.11B).

Hughes Clarke et al. (2012) carried out repeat bathymetric surveys, finding highly active proximal channels with over 100 events during summer 2011. Stacey et al. (2019)

extended this study by adding seismic profiles, sediment cores and ^{210}Pb analyses, and established a comprehensive study of event frequency from source-to-sink in this fjord. In Howe Sound, highly active proximal channels experience >100 events per year (Fig. 4.11B). Events are mostly initiated by sediment settling from dilute river plumes (Hizzett et al., 2018). The submarine channels only extend 1-2 km from the river mouth, although the system might still be evolving with channels continuing to grow, due to forced channel avulsion in 1971 (Stacey et al., 2019). Down-slope of these incised channels, the lobe complex experiences ∼20 events per year. Beyond these lobes, the loss of confinement results in the rapid dissipation of events with only 1-10 events per year occurring on the mid-slope. This mid-slope still maintains a gradient between 0.3-1.2°, and lies between the lobe complex and deep-basin. The distal flat basin, 11 km from the delta, records large volume events at a recurrence interval of ca. 100 years.

The turbidity current activity in Bute Inlet and Howe Sound is broadly similar, with high rates of activity on an annual basis, and thick sand deposits in the deep basin on centennial timescales (Fig. 4.11). When looking into the modern-day activity, event frequency diverges, most likely due to the different system size. Both systems experience ca. 100 events yearly near the delta. However, where Bute Inlet experiences only one, dissipating, event per year on the lobe, Howe Sound experiences >20 events on the lobe. The lobe in Howe Sound is only 2 km offshore. Markedly, the unconfined mid-slope in Howe Sound still experiences 1-10 events per year. Thus, it appears that the degree of confinement is a less important control, and other factors such as distance from the delta, seafloor gradient or substrate availability could exert an additional control on modern-day turbidity current activity. Furthermore, it could be that the current disparity in event frequency beyond channel confinement is due to ongoing evolution and expansion of the immature Howe Sound channel system. For instance, the seafloor gradient on the mid-slope in Howe Sound remains between 0.3 and 1.2°, and may be prone to channelization at a later stage following the recent avulsion (Stacey et al., 2019).

When looking on longer timescales, Howe Sound and Bute Inlet both experience larger-scale events that deposit thick sands on the basin floor. In Howe Sound these are suggested to be slightly more frequent, once every 100 years, whereas in Bute Inlet these are suggested to occur ∼240 years ago, although these ages are similar when considering the uncertainty of analysis. A definitive origin of these larger-scale events cannot be established for either system. The deep basin deposits could be due to local, regional or global factors. Local large-scale influx due to heightened river discharge or fjord sidewall collapse could occur within approximately the same time

scale. Regional factors such as earthquakes are possible too. In Howe Sound, the data suggests that at most one deep basin event (out of four) can be associated to an earthquake. Alternatively, a global mechanism, applicable to various submarine systems could lead to these thick sand deposits in the deep basin. Canyon filling and flushing has previously been proposed, where small events fill the channel, and irregular events cannibalise these previously deposited sediments and flush the system (Piper and Normark, 2009). If the larger-scale deposits in the deep basins of Bute Inlet and Howe Sound represent evens on a local, regional or global scale requires further analysis.

4.8 Conclusions

Three event frequencies are seen in Bute Inlet. High frequency events occur annually, and are confined within the channel. Ca. 100 events are observed proximally. Downslope of the delta, the number of flows passing the moorings declines with distance, with one event per year traversing the entire incised channel to the lobe. These high frequency events tend to occur during the freshet season, with elevated river discharge levels (Prior et al., 1987). Intermediate frequency events have recurrence intervals of ca. 20 years, and are deposited on terraces 15-20 m above the current-day thalweg. The origin of these intermediate scale events is speculative, although knickpoint migration is likely to be a major control. Knickpoints are ∼30 m steep steps that erode the channel and occur on similar timescales as the intermediate frequency events (Heijnen et al., 2020). Just before knickpoint migration, the channel will be shallower, with the reduced height difference making the terrace more susceptible to overspill. Moreover, this would suggest that the high and intermediate event frequencies may have similar event magnitudes. Finally, low frequency, high magnitude, events are found in the deep basin, located beyond the channel-lobe-complex. Thick sand deposits were last deposited ca. 240 years ago. Three mechanisms that could lead to these thick deposits are proposed, namely increased input from the nearby Orford river; large-scale failures due to sidewall collapse or earthquakes; or large-scale events from the Homathko Delta that are eroding previous deposits and flushing the submarine channel.

Comparing the event frequencies found in Bute Inlet to the nearby Howe Sound fjord system, similar event frequencies between the two systems are found. Current-day measurements show that both submarine systems are highly active, with ca. 100 events per year near the deltas. Deposits show thick sand deposits on the basin floor

of Howe Sound as well, occurring every ca. 100 years. Again, the origins of these deposits are not well constrained. Further analysis is necessary to determine if these thick distal sand deposits are local, regional, or global; i.e. due to fjord sidewall collapse, earthquakes, or channel filling and flushing following Piper and Normark (2009).

This study adds to our understanding on frequency of turbidity currents over space and time, and manages to bridge a gap between smaller, high-frequency events observed in modern-day turbidity current measurements and the large, infrequent events deposited in the deep basin. It therefore helps to constrain how and why turbidity current frequency and magnitude vary with distance, and hence assess hazards to seafloor infrastructure, and how sediment and organic carbon is moved to the deep-sea.

4.9 Acknowledgements

We thank the crew of the CCGS Vector and RV John Strickland for the assistance in data collection. C.J. Heerema is funded by the European Union's Horizon 2020 research and innovation program under the Marie Skłodowska-Curie grant agreement No 721403 - ITN SLATE. E. Pope was supported by a Leverhulme Trust Early Career Fellowship (ECF-2018-267). M.J.B. Cartigny was supported by a Royal Society Research Fellowship. M.A. Clare acknowledges support from NERC National Capability project Climate Linked Atlantic Sector Science (NE/R015953/1).

Chapter 5

Conclusions and Future Outlook

This thesis has explored the evolution of turbidity currents, using direct field measurements. These sediment density flows can be episodic and powerful, leading to sediment, nutrient and pollutant dispersal to the deep sea. Furthermore, these events can severely damage seafloor infrastructure. Understanding fundamental flow behaviour, such as how these flows evolve, will aid risk assessments, and estimates of global carbon fluxes. Direct measurements from acoustic Doppler current profilers (ADCPs) have been analysed from three locations worldwide. These datasets are all in different oceanographic settings, providing a diverse view on turbidity current behaviour. Chapter 2 includes the most detailed monitoring field experiment to date in the littoral-fed Monterey Canyon, offshore California. This dataset includes 18 months of observations at six mooring locations at sub-minute intervals. Chapter 3 discusses proximal monitoring in the Var Canyon, offshore southeastern France. The Var Canyon is a river-fed canyon system. Finally, Chapter 4 includes source-to-sink direct measurements in combination with sediment cores in Bute Inlet, a river-fed channelized fjord in British Columbia. These three datasets provide new insights into turbidity current flow behaviour. The overall aim of this thesis is to use direct measurements of turbidity currents to understand the evolution of turbidity currents over time and space.

Specifically, these datasets allowed for addressing the following research questions:

1. What determines the evolution of flows over distance? (Chapter 2)
2. Can you identify the trigger of a flow from its velocity signature? (Chapter 3)
3. How do the frequency and magnitude of turbidity currents change with distance, and what controls this pattern? (Chapter 4)

5.1 Main Conclusions

The next sections outline the three scientific chapters and briefly highlight the key research questions and wider interest, what data was available, and the main conclusions of each chapter. Chapter 2 has been published in Earth and Planetary Science Letters as 'What determines the downstream evolution of turbidity currents?' (2020) `https://doi.org/10.1016/j.epsl.2019.116023`. Chapter 3 is in review in Journal of Sedimentary Research as "How distinctive are flood-triggered turbidity currents?"; Chapter 4 is being prepared for submission.

5.1.1 Chapter 2: What determines the evolution of flows over distance?

Due to the difficulty of monitoring turbidity currents in action, relatively little is known about basic flow parameters, such as how their velocity develops over distance. Therefore, it has not been possible to test fundamental theories of turbidity current flow behaviour from the '60-'80s (Bagnold, 1962, Pantin, 1979, Parker et al., 1986, Parker, 1982). These theories suggest that flows can experience positive feedbacks where they erode and accelerate (ignite), or in contrast, they can dissipate as flows deposit and decelerate. Third, flows can autosuspend, where they reach a near-uniform state either due to balanced erosion and deposition or because the seafloor is too hard to erode. Understanding this flow behaviour has important implications for sediment dispersal and hazard assessment, yet it has been difficult to test in the field. The data presented in Chapter 2 provide a unique opportunity to determine how velocity changes over distances, with six moorings deployed over 18 months in the upper Monterey Canyon, offshore California.

Chapter 2 shows broadly consistent patterns in flow runout behaviour in Monterey Canyon, and two factors controlling flow behaviour are found. The runout distance of most flows can be based on their initial flow velocity, as measured at the first mooring. Here, small increases in initial flow velocity lead to disproportional increases in runout length. These flows initially ignite, and when flows exceed a velocity threshold, flows can lengthen and auto-suspend to run out further. This observed autosuspension in Monterey Canyon is also found in Gaoping Canyon, offshore Taiwan. For the Monterey Canyon dataset, the detailed ADCP measurements also show that these faster, auto-suspending flows consist of a high velocity, high density front not previously suggested (see also Paull et al., 2018, Wang et al., 2020).

Besides initial velocity, the observed events in Monterey Canyon suggest that the availability of erodible substrate is another factor controlling flow behaviour. The data shows one event forms an exception to the otherwise consistent flow pattern. Here, initial velocity was low, followed by mid-canyon ignition. As this was the only flow to occur during the quiescent summer months, mid-canyon ignition likely occurred due to the build-up of easy-erodible substrate during preceding months. Thus, flows can ignite when meeting a certain velocity threshold, or when there is easily erodible substrate available.

The field data shows reasonable agreement with the proposed theories on flow behaviour. However, both the proposed theories and field data have significant limitations and key assumptions are necessary, complicating the testing of proposed theories. The older theoretical models do not include a dense near-bed layer, which has been observed in these data, and thus a new turbidity current model is proposed. Initially, flows ignite with a dense and fast layer at its front. This high-velocity, dense front disperses sediment to the rear, creating a dilute trailing cloud, leading to a stretched flow. This turbidity current as a whole is auto-suspending with local erosion at its front and deposition at its rear. As flows dissipate, the dense layer at the front also dissipates.

5.1.2 Chapter 3: Can you identify the trigger of a flow from its velocity signature?

Deposits of flood-triggered turbidity currents (turbidites) are proposed to provide valuable information on past river floods, and thus continental erosion and climate. A series of depositional models have been proposed, which can be used to identify flood-triggered turbidites (Mulder et al., 2003, Nakajima, 2006, Khripounoff et al., 2012, Zavala and Pan, 2018). These depositional models assume that river floods lead to characteristic turbidity current velocity structures, resulting in identifiable flood-triggered turbidites. Four unique criteria of the turbidity currents velocity structures are suggested, caused by the river flood hydrograph: 1) a prolonged duration of the flow; 2) a gradual velocity increase; 3) multiple cycles of acceleration and deceleration; and 4) low peak velocity.

The Var Canyon-River location presented in Chapter 3 includes the analysis of data from a proximal ADCP, 6 km offshore, where detailed velocity measurements allow for testing of the proposed velocity structure criteria. Another mooring, 16 km offshore, is used to determine how this velocity signature evolves down-canyon. Three distinct

events are measured and discussed in Chapter 3, two of which are associated to distinct river floods. A third event is likely initiated by seabed slope failure.

The proximal observations show that the proposed velocity criteria are applicable to flood-triggered events, but that they are not exclusive to flood-triggered events. Rather, the event not associated to a river flood matches the criteria best. Most probably this event is caused by a landslide trigger, such as a breaching failure, where the sustained nature such failure events can resemble flood-triggered events. The down-channel mooring shows re-organisation of the velocity structure of all three events. Amalgamation, due to reduced drag and entrainment of the erodible substrate, transforms the velocity structure from multi-pulsed to single-pulsed event. However, such single-pulsed flows, with a rapid onset, are typically associated with landslide-triggered events in literature. Self-organisation of the flow thus causes the original trigger to be indiscernible within 16 km. Finally, similar river discharge levels have not consistently led to similar turbidity current activity. These observations suggest that identifying paleo-flood deposits may not be as straightforward as previously proposed.

5.1.3 Chapter 4: How do the frequency and magnitude of turbidity currents change with distance, and what controls this pattern?

The frequency and magnitude of turbidity currents affects sediment dispersal, seafloor geohazards and nutrient cycles such as the global carbon cycle. Few studies exist that explore the frequency of turbidity currents over distance, especially when combining direct measurements with sediment cores. Chapter 4 combines ADCP measurements with sediment cores on a source-to-sink scale in Bute Inlet, British Colombia. The combination of direct measurements and sediment cores allows for comparison between present-day frequencies and longer-term variations of turbidity current activity, on a source-to-sink scale.

Three flow frequency classes are found. The ADCPs record yearly small, frequent flows that mostly do not extend beyond the first two moorings. These flows are associated with the yearly freshet season. On the terraces, a second flow class occurs approximately every 20 years. The source of these flows is not well constrained, but a proposed mechanism is knickpoint (steep steps in the channel floor) migration. These knickpoints are suggested to be responsible for channel maintenance and terrace formation (Heijnen et al., 2020). Prior to knickpoint erosion of the channel, the

height difference between terrace and thalweg will be severely reduced, enabling flow overspill. A third flow class is shown in the deep basin, beyond the lobe. Here, current-day mud deposits prevail, but a thick sand deposited ca. 240 years ago. The source and trigger of these flows remains speculative, but are a significantly greater magnitude than the small and intermediate frequency flows. Fjord sidewall collapse, or major events flushing the incised channel are suggested.

Comparison to another nearby Canadian fjord shows commonality in frequency-magnitudes of turbidity currents (Stacey et al., 2019). Both submarine systems suggest bimodality in flow frequency-magnitudes, with frequent, smaller events versus infrequent large-scale, more hazardous, events occurring on centennial timescales. These results suggest the large-scale events are controlled differently from the small-scale events. The former is more likely due to infrequent, large triggers, whereas the small-scale events are likely due to yearly river floods. The large-scale events are more likely preserved in the rock record.

5.2 Synthesis: Evolution of Turbidity Currents

This brief section aims to bring together the three separate scientific chapters, and find commonality in the behaviour of turbidity currents across different oceanographic settings.

5.2.1 The importance of substrate availability

Chapter 2 shows that two factors influence the runout of turbidity currents: initial velocity and the availability of easily-erodible substrate. Substrate availability again is an important factor in the transformation of flow structures, as seen in Chapter 3. Hence, substrate availability can be significant in turbidity current evolution, as it controls runout and structure, inevitably impacting hazard assessments, and dispersal of sediments and nutrients. Both chapters can only speculate that seafloor substrate is important, as there are no direct measurements available of the state of the seafloor. Traer et al. (2012) found that substrate erosion can dominate turbidity current behaviour based on numerical models. Laboratory experiments have shown rapid dissipation for flow-bed interaction with a soft clay bed, due to severe mixing and erosion processes (Verhagen et al., 2013) and cohesive clay bonds (Baas et al., 2014). However, other density flows, such as snow avalanches and pyroclastic density currents, show that substrate entrainment actually increases runout distance

(Mangeney et al., 2007, Pollock et al., 2016). Experimental debris flows show that wet substrate can increase the runout distance and velocity (Iverson et al., 2011). In Monterey Canyon, the seafloor is suggested to comprise of loosely-packed, water-saturated sand, which may therefore easily liquefy (Paull et al., 2013, 2018). The impact of the state of substrate on the behaviour of turbidity currents requires further investigation. Specifically, for turbidity currents we need a greater understanding of the state of the seafloor preceding an event. Future research could be aimed towards more specific geotechnical properties of the substrate, especially proximally as this thesis indicates that initial velocities dictate flow evolution.

5.2.2 The importance of infrequent and larger flows

Chapter 4 shows that the data collected by ADCPs can still be considered small-scale flows over geologic timescales, as these flows are all confined to the main channel thalweg. The large scale, infrequent and more hazardous, flows will ultimately dictate the dispersal of sediments and nutrients. These large-scale events will cannibalise deposits from the small-scale (ADCP measured) flows, and flush submarine systems, such that sediment is eventually deposited on abyssal plains or deep basins. These large-scale flushing events are thus most likely to have a disproportional effect on submarine systems. Thus, although the ADCP measurements suggest initial velocity and substrate availability are important controls on turbidity current evolution, these factors may not be key for large-scale flows. Conversely, our understanding of turbidity currents is largely derived from the large-scale flow deposits, which may occur under different mechanisms and flow dynamics compared to the smaller-scale modern-day flows. As Chapter 3 has shown, amalgamation of flow pulses can severely alter the velocity structure of turbidity currents over distance, which is likely reflected in deposits as well. Future efforts to understand the importance of large flows should be directed at better age-dating of distal events, especially in the larger canyon systems. Unfortunately, there are few cores taken on distal lobes, due to piston cores bouncing in this typical sandy environment, and general inaccessibility as the lobes are deep and far offshore. Even fewer sediment cores from the distal lobes are actually dated. However, at some sites such as Nazaré Canyon, the recurrence interval of large flushing events has been constrained (Allin et al., 2016). Once these distal, large events in canyon systems worldwide are better constrained, their importance locally and globally can be assessed. Comparison of multiple submarine systems is necessary to determine global trends in frequency-magnitude of events.

5.3 Future Outlook

The work presented in this thesis uses ADCP measurements. Although these scientific chapters include the most detailed datasets to date, future direct measurements could improve by increasing the number of locations and simultaneous mooring deployments and by further developing monitoring methods. Finally, implementing the findings from these direct measurements into numerical models is an essential next step.

5.3.1 Increase direct measurement datasets

The recent successful ADCP deployments have led to continuously new insights in turbidity currents (i.e. Xu, 2010, Liu et al., 2012, Khripounoff et al., 2012, Azpiroz-Zabala et al., 2017, Paull et al., 2018, Heerema et al., 2020, Chapters 3 and 4 this thesis). The current deployments have been in a limited number of systems or with a limited number of instruments (as shown in Fig. 1.1, Chapter 1: Introduction). The successes with direct monitoring of turbidity currents, and the limited systems that have been monitored so far, thus invite more field campaigns. These can either be in new submarine systems previously not monitored, or expanding on direct measurements in previously measured systems. By expanding to different submarine systems, commonalities across the world, and across similar oceanographic settings can be found. For instance, if the findings in Chapter 4 apply to Canadian fjords only due to for instance particular geologic settings or earthquake activity, or if they apply elsewhere in other fjords and canyons too. By expanding on existing datasets, we gain an insight on longer-term trends in turbidity current behaviour and activity, and possibly place moorings at sites with remaining questions, i.e. more proximal or distal moorings. Proximal moorings can be used to infer the triggering processes of turbidity currents. As Chapter 3 has shown, the velocity structure of turbidity currents evolves rapidly and getting more proximal measurements can lead to better insights on the initiation processes. For the distal moorings, a larger turbidity current could be recorded if such a flow were to occur. Chapter 4 shows new insights on source-to-sink behaviour in a small-scale system. Continuing this research on greater scale in submarine canyon systems, by including more distal moorings, would be a logical continuation.

5.3.2 New direct measurement methods

ADCP data have provided an incredible wealth of information on turbidity currents in current-day systems. Yet, there are downsides to ADCPs. The instruments are expensive, yet placed in hazardous pathways, and battery and memory card constraints limit deployment times. Thus, ADCP deployments are costly. Moreover, ADCP data is poor in the near-bed region, yet important flow processes occur in this zone. Measurement methods such as hydrophones and smart boulders can provide additional information in direct measurement techniques (i.e. Paull et al., 2018, Lintern et al., 2019, Clare et al., 2020). In this ever-developing field, a focus on direct measurements capturing flow characteristics such as the dense near-bed layer, fluxes between turbidity current and surrounding water and sediment, or internal fluxes of sediment, will be sought-after data.

5.3.3 Beyond direct measurements of turbidity currents

ADCP measurements have been restricted to smaller magnitude flows in a few systems. There is much to learn about turbidity currents beyond these direct measurements. Using data from other gravity flow types, such as pyroclastic flows, debris flows or powder-snow avalanches, could potentially provide valuable insights for all gravity flows. For instance, observations for subaerial gravity flows is considerably more accessible, where test sites at field scale can be used to understand processes such as mixing and entrainment (i.e. Iverson et al., 2011, Sovilla et al., 2015). However, there are also major challenges in monitoring of pyroclastic flows, which are rare, particularly fast and hot, leading to few direct measurements. Yet, the few direct observations from pyroclastic flows have helped to, for instance, constrain their interaction with topography (Sulpizio et al., 2014), which is difficult to constrain for turbidity currents. On the other hand, the detailed vertical data on velocities and sediment concentrations from turbidity currents help to understand internal structures, and such internal velocity measurements are difficult to attain for other gravity flows (i.e. Sovilla et al., 2015). There are however some key differences between these gravity flow types in terms of basic flow physics. For instance, the substrate, maximum speeds, runout distance and the slope at which these events occur varies greatly. Thus, great care is needed in exchanging findings on flow properties between the various gravity flow types.

For turbidity currents specifically, using these high-resolution direct measurements to calibrate numerical, laboratory and theoretical models is another step forward.

Implementing the direct measurements into models can help resolve turbidity current behaviour during large-scale, infrequent flows and provide well-constrained risk assessments. For instance, the effect of substrate on flow behaviour will need to be tested further, for instance via laboratory models, as this is as of yet difficult to define in direct measurements. Proposed hypotheses on substrate-event interactions can then be further tested in at least numerical models, and in time perhaps tested in the field. Furthermore, implementing the data from Monterey Canyon presented in Chapter 2 into a numerical model requires models to be able to capture dissipating, igniting and autosuspending flow behaviour, and be adjusted according to initial velocity. An initial attempt has been made to implement the data from Chapter 2 into a 2.5D numerical model in OpenFOAM that accurately represent the bathymetry as well (Rauter et al., 2019). This model is now freely available, and can be used in the wider scientific community. Although many parameters remain unknown, such as fluxes between the proposed dense frontal cell and the dilute trailing cloud, the data from Monterey Canyon provides a unique opportunity for numerical modelling. For instance, because of the high number of mooring stations, the data from the first mooring station can be used as the initial flow conditions, and the remaining monitoring stations can be used to test between field data and numerical model output.

Bibliography

Allin, J. R., Hunt, J. E., Talling, P. J., Clare, M. A., Pope, E., and Masson, D. G. (2016). Different frequencies and triggers of canyon filling and flushing events in Nazaré Canyon, offshore Portugal. *Marine Geology*, 371:89–105.

Appleby, P. and Oldfield, F. (1992). *Applications of lead-210 to sedimentation studies*. Clarendon Press, United Kingdom.

Appleby, P. G. (2013). 210Pb dating: thirty-five years on. *Journal of Paleolimnology*, 49(4):697–702.

Arnaud, F., Magand, O., Chapron, E., Bertrand, S., Boës, X., Charlet, F., and Mélières, M.-A. (2006). Radionuclide dating (210Pb, 137Cs, 241Am) of recent lake sediments in a highly active geodynamic setting (Lakes Puyehue and Icalma—Chilean Lake District). *Science of The Total Environment*, 366(2-3):837–850.

Azpiroz-Zabala, M., Cartigny, M. J. B., Talling, P. J., Parsons, D. R., Sumner, E. J., Clare, M. A., Simmons, S. M., Cooper, C., and Pope, E. L. (2017). Newly recognized turbidity current structure can explain prolonged flushing of submarine canyons. *Science Advances*, 3(10):e1700200.

Baas, J. H., Best, J. L., Peakall, J., and Wang, M. (2009). A Phase Diagram for Turbulent, Transitional, and Laminar Clay Suspension Flows. *Journal of Sedimentary Research*, 79(4):162–183.

Baas, J. H., Manica, R., Puhl, E., Verhagen, I., and Borges, A. L. d. O. (2014). Processes and products of turbidity currents entering soft muddy substrates. *Geology*, 42(5):371–374.

Bagnold, R. (1962). Auto-suspension of transported sediment; turbidity currents. *Proceedings of the Royal Society of London*, 265(1322):315–319.

Benoit, G. and Rozan, T. F. (2001). 210Pb and 137Cs dating methods in lakes: A retrospective study. *Journal of Paleolimnology*, 25(4):455–465.

Blandin, J. (2010). SOLVEIG III cruise, L'Europe R/V.

Bornhold, B. D., Ren, P., and Prior, D. B. (1994). High-frequency turbidity currents in British Columbia fjords. *Geo-Marine Letters*, 14(4):238–243.

Bouma, A. (1962). Sedimentology of some flysch deposits: A graphic approach to facies interpretation. *Elsevier, Amsterdam-New York*, page 168.

Canals, M., Lastras, G., Urgeles, R., Casamor, J., Mienert, J., Cattaneo, A., De Batist, M., Haflidason, H., Imbo, Y., Laberg, J., Locat, J., Long, D., Longva, O., Masson, D., Sultan, N., Trincardi, F., and Bryn, P. (2004). Slope failure dynamics and impacts from seafloor and shallow sub-seafloor geophysical data: case studies from the COSTA project. *Marine Geology*, 213(1-4):9–72.

Canals, M., Puig, P., Madron, X. D. d., Heussner, S., Palanques, A., and Fabres, J. (2006). Flushing submarine canyons. *Nature*, 444(7117):354–357.

Cantero, M. I., Cantelli, A., Pirmez, C., Balachandar, S., Mohrig, D., Hickson, T. A., Yeh, T.-h., Naruse, H., and Parker, G. (2012). Emplacement of massive turbidites linked to extinction of turbulence in turbidity currents. *Nature Geoscience*, 5(1):42–45.

Carter, L., Gavey, R., Talling, P., and Liu, J. (2014). Insights into Submarine Geohazards from Breaks in Subsea Telecommunication Cables. *Oceanography*, 27(2):58–67.

Clare, M., Hughes Clarke, J., Talling, P., Cartigny, M., and Pratomo, D. (2016). Preconditioning and triggering of offshore slope failures and turbidity currents revealed by most detailed monitoring yet at a fjord-head delta. *Earth and Planetary Science Letters*, 450:208–220.

Clare, M., Lintern, D. G., Rosenberger, K., Hughes Clarke, J. E., Paull, C., Gwiazda, R., Cartigny, M. J. B., Talling, P. J., Perara, D., Xu, J., Parsons, D., Jacinto, R. S., and Apprioual, R. (2020). Lessons learned from the monitoring of turbidity currents and guidance for future platform designs. *Geological Society, London, Special Publications*, 500(1):605–634.

Clare, M. A., Vardy, M. E., Cartigny, M. J., Talling, P. J., Himsworth, M. D., Dix, J. K., Harris, J. M., Whitehouse, R. J., and Belal, M. (2017). Direct monitoring of active geohazards: emerging geophysical tools for deep-water assessments. *Near Surface Geophysics*, 15(4):427–444.

Covault, J. A., Kostic, S., Paull, C. K., Sylvester, Z., and Fildani, A. (2017). Cyclic steps and related supercritical bedforms: Building blocks of deep-water depositional systems, western North America. *Marine Geology*, 393:4–20.

de Stigter, H. C., Boer, W., de Jesus Mendes, P. A., Jesus, C. C., Thomsen, L., van den Bergh, G. D., and van Weering, T. C. (2007). Recent sediment transport and deposition in the Nazaré Canyon, Portuguese continental margin. *Marine Geology*, 246(2-4):144–164.

Edwards, A. and Gray, J. (2015). Erosion–deposition waves in shallow granular free-surface flows. *Journal of Fluid Mechanics*, 762:35–67.

Eidsvik, K. J. and Brørs, B. (1989). Self-accelerated turbidity current prediction based upon (k-ϵ) turbulence. *Continental Shelf Research*, 9(7):617–627.

Feng, Z.-Z. (2019). Words of the Editor-in-Chief —— some ideas about the comments and discussions of hyperpycnal flows and hyperpycnites. *Journal of Palaeogeography*, 8(1):25.

Ferguson, R. and Church, M. (2004). A Simple Universal Equation for Grain Settling Velocity. *Journal of Sedimentary Research*, 74(6):933–937.

Fildani, A. (2017). Submarine Canyons: A brief review looking forward. *Geology*, 45(4):383–384.

Fukushima, Y., Parker, G., and Pantin, H. (1985). Prediction of ignitive turbidity currents in scripps submarine canyon. *Marine Geology*, 67(1):55 – 81.

Gales, J. A., Talling, P. J., Cartigny, M. J., Hughes Clarke, J., Lintern, G., Stacey, C., and Clare, M. A. (2019). What controls submarine channel development and the morphology of deltas entering deep-water fjords? *Earth Surface Processes and Landforms*, 44(2):535–551.

Galy, V., France-Lanord, C., Beyssac, O., Faure, P., Kudrass, H., and Palhol, F. (2007). Efficient organic carbon burial in the Bengal fan sustained by the Himalayan erosional system. *Nature*, 450(7168):407–410.

Gavey, R., Carter, L., Liu, J. T., Talling, P. J., Hsu, R., Pope, E., and Evans, G. (2017). Frequent sediment density flows during 2006 to 2015, triggered by competing seismic and weather events: Observations from subsea cable breaks off southern Taiwan. *Marine Geology*, 384:147–158.

Goldfinger, C., Morey, A. E., Nelson, C. H., Gutiérrez-Pastor, J., Johnson, J. E., Karabanov, E., Chaytor, J., and Eriksson, A. (2007). Rupture lengths and temporal history of significant earthquakes on the offshore and north coast segments of the Northern San Andreas Fault based on turbidite stratigraphy. *Earth and Planetary Science Letters*, 254(1-2):9–27.

Gwiazda, R., Paull, C., Ussler, W., and Alexander, C. (2015). Evidence of modern fine-grained sediment accumulation in the Monterey Fan from measurements of the pesticide DDT and its metabolites. *Marine Geology*, 363:125–133.

Hage, S., Cartigny, M. J., Sumner, E. J., Clare, M. A., Hughes Clarke, J. E., Talling, P. J., Lintern, D. G., Simmons, S. M., Silva Jacinto, R., Vellinga, A. J., Allin, J. R., Azpiroz-Zabala, M., Gales, J. A., Hizzett, J. L., Hunt, J. E., Mozzato, A., Parsons, D. R., Pope, E. L., Stacey, C. D., Symons, W. O., Vardy, M. E., and Watts, C. (2019). Direct Monitoring Reveals Initiation of Turbidity Currents From Extremely Dilute River Plumes. *Geophysical Research Letters*, 46(20):11310–11320.

Hage, S., Galy, V., Cartigny, M., Acikalin, S., Clare, M., Gröcke, D., Hilton, R., Hunt, J., Lintern, D., McGhee, C., Parsons, D., Stacey, C., Sumner, E., and Talling, P. (2020). Efficient preservation of young terrestrial organic carbon in sandy turbidity-current deposits. *Geology*, 48(9):882–887.

Heerema, C. J., Talling, P. J., Cartigny, M. J., Paull, C. K., Bailey, L., Simmons, S. M., Parsons, D. R., Clare, M. A., Gwiazda, R., Lundsten, E., Anderson, K., Maier, K. L., Xu, J. P., Sumner, E. J., Rosenberger, K., Gales, J., McGann, M., Carter, L., and Pope, E. (2020). What determines the downstream evolution of turbidity currents? *Earth and Planetary Science Letters*, 532:116023.

Heezen, B. C. and Ewing, W. M. (1952). Turbidity currents and submarine slumps, and the 1929 Grand Banks [Newfoundland] earthquake. *American Journal of Science*, 250(12):849–873.

Heijnen, M. S., Clare, M. A., Cartigny, M. J. B., Talling, P. J., Hage, S., Lintern, D. G., Stacey, C., Parsons, D. R., Simmons, S. M., Chen, Y., Sumner, E. J., Dix, J. K., and Hughes Clarke, J. E. (2020). Rapidly-migrating and internally-generated knickpoints can control submarine channel evolution. *Nature Communications*, 11(1):3129.

Hirose, K. and Aoyama, M. (2003). Present background levels of surface 137Cs and 239,240Pu concentrations in the Pacific. *Journal of Environmental Radioactivity*, 69(1-2):53–60.

Hizzett, J. L., Hughes Clarke, J. E., Sumner, E. J., Cartigny, M. J. B., Talling, P. J., and Clare, M. A. (2018). Which Triggers Produce the Most Erosive, Frequent, and Longest Runout Turbidity Currents on Deltas? *Geophysical Research Letters*, 45(2):855–863.

Ho, V. L., Dorrell, R. M., Keevil, G. M., Burns, A. D., and McCaffrey, W. D. (2018). Pulse propagation in turbidity currents. *Sedimentology*, 65(2):620–637.

Hu, P., Pähtz, T., and He, Z. (2015). Is it appropriate to model turbidity currents with the three-equation model? *Journal of Geophysical Research: Earth Surface*, 120(7):1153–1170.

Hubbard, S. M., Covault, J. A., Fildani, A., and Romans, B. W. (2014). Sediment transfer and deposition in slope channels: Deciphering the record of enigmatic deep-sea processes from outcrop. *GSA Bulletin*, 126(5-6):857–871.

Hughes Clarke, J. E. (1988). *The geological record of the 1929 Grand Banks earthquake and its relevance to deep-sea clastic sedimentation (unpublished PhD thesis).* PhD thesis, Dalhousie University, Nova Scotia.

Hughes Clarke, J. E. (2016). First wide-angle view of channelized turbidity currents links migrating cyclic steps to flow characteristics. *Nature Communications*, 7:11896.

Hughes Clarke, J. E., Brucker, S., Muggah, J., Church, I., Cartwright, D., Kuus, P., Pratomo, D., and Eisan, B. (2012). The Squamish ProDelta: Monitoring Active Landslides and Turbidity Currents. In *Canadian Hydrographic Conference 2012*.

Hughes Clarke, J. E., Marques, C. R. V., and Pratomo, D. (2014). Imaging Active Mass-Wasting and Sediment Flows on a Fjord Delta, Squamish, British Columbia. In Krastel, S., Behrmann, J.-H., Völker, D., Stipp, M., Berndt, C., Urgeles, R., Chaytor, J., Huhn, K., Strasser, M., and Harbitz, C. B., editors, *Submarine Mass Movements and Their Consequences*, volume 37, pages 249–260. Springer International Publishing, Cham. Series Title: Advances in Natural and Technological Hazards Research.

Hughes Clarke, J. E., Shor, A. N., Piper, D. J. W., and Mayer, L. A. (1990). Large-

scale current-induced erosion and deposition in the path of the 1929 Grand Banks turbidity current. *Sedimentology*, 37(4):613–629.

Inman, D. L., Nordstrom, C. E., and Flick, R. E. (1976). Currents in Submarine Canyons: An Air-Sea-Land Interaction. *Annual Review of Fluid Mechanics*, 8(1):275–310.

Iverson, R. M. (2012). Elementary theory of bed-sediment entrainment by debris flows and avalanches. *Journal of Geophysical Research: Earth Surface*, 117(F3).

Iverson, R. M., Logan, M., LaHusen, R. G., and Berti, M. (2010). The perfect debris flow? Aggregated results from 28 large-scale experiments. *Journal of Geophysical Research: Earth Surface*, 115(F3). Publisher: John Wiley & Sons, Ltd.

Iverson, R. M., Reid, M. E., Logan, M., LaHusen, R. G., Godt, J. W., and Griswold, J. P. (2011). Positive feedback and momentum growth during debris-flow entrainment of wet bed sediment. *Nature Geoscience*, 4(2):116–121.

Johnson, H. P., Gomberg, J. S., Hautala, S. L., and Salmi, M. S. (2017). Sediment gravity flows triggered by remotely generated earthquake waves: Remotely Triggered Turbidites. *Journal of Geophysical Research: Solid Earth*, 122(6):4584–4600.

Khripounoff, A., Crassous, P., Lo Bue, N., Dennielou, B., and Silva Jacinto, R. (2012). Different types of sediment gravity flows detected in the Var submarine canyon (northwestern Mediterranean Sea). *Progress in Oceanography*, 106:138–153.

Khripounoff, A., Vangriesheim, A., Crassous, P., and Etoubleau, J. (2009). High frequency of sediment gravity flow events in the Var submarine canyon (Mediterranean Sea). *Marine Geology*, 263(1-4):1–6.

Kneller, B. and Buckee, C. (2000). The structure and fluid mechanics of turbidity currents: a review of some recent studies and their geological implications: Structure of turbidity currents. *Sedimentology*, 47:62–94.

Kneller, B., Nasr-Azadani, M. M., Radhakrishnan, S., and Meiburg, E. (2016). Long-range sediment transport in the world's oceans by stably stratified turbidity currents: Longe-range transport in the ocean. *Journal of Geophysical Research: Oceans*, 121(12):8608–8620.

Komar, P. D. (1985). The hydraulic interpretation of turbidites from their grain sizes and sedimentary structures. *Sedimentology*, 32(3):395–407.

Kostic, S. and Parker, G. (2006). The response of turbidity currents to a canyon–fan transition: internal hydraulic jumps and depositional signatures. *Journal of Hydraulic Research*, 44(5):631–653.

Kuenen, P. H. (1937). Experiments in connection with Daly's hypothesis on the formation of submarine canyons. *Leidse Geo. Meded.*, 8:327–355.

Kuenen, P. H. and Migliorini, C. I. (1950). Turbidity currents as a cause of graded bedding. *The Journal of Geology*, 58(2):91–127.

Lintern, D. G., Hill, P. R., and Stacey, C. (2016). Powerful unconfined turbidity current captured by cabled observatory on the Fraser River delta slope, British Columbia, Canada. *Sedimentology*, 63(5):1041–1064.

Lintern, D. G., Mosher, D. C., and Scherwath, M. (2019). Advancing from subaqueous mass movement case studies to providing advice and mitigation. *Geological Society, London, Special Publications*, 477(1):1–14.

Liu, J. T., Lin, H.-L., and Hung, J.-J. (2006). A submarine canyon conduit under typhoon conditions off Southern Taiwan. *Deep Sea Research Part I: Oceanographic Research Papers*, 53(2):223–240.

Liu, J. T., Wang, Y.-H., Yang, R. J., Hsu, R. T., Kao, S.-J., Lin, H.-L., and Kuo, F. H. (2012). Cyclone-induced hyperpycnal turbidity currents in a submarine canyon. *Journal of Geophysical Research: Oceans*, 117(C4):C04033.

Løvholt, F., Schulten, I., Mosher, D., Harbitz, C., and Krastel, S. (2019). Modelling the 1929 grand banks slump and landslide tsunami. *Geological Society, London, Special Publications*, 477(1):315–331.

Lowe, D. R. (1976). Subaqueous liquefied and fluidized sediment flows and their deposits. *Sedimentology*, 23(3):285–308. Publisher: John Wiley & Sons, Ltd.

Lowe, D. R. (1979). Sediment gravity flows: their classification and some problems of application to natural flows and deposits. In Doyle, L. and Pilkey, O., editors, *Geology of Continental Slopes*, pages 75–82. Society of Economic Paleontologists and Mineralogists Special Publication.

Luchi, R., Balachandar, S., Seminara, G., and Parker, G. (2018). Turbidity Currents With Equilibrium Basal Driving Layers: A Mechanism for Long Runout. *Geophysical Research Letters*, 45(3):1518–1526.

Maier, K. L., Gales, J. A., Paull, C. K., Rosenberger, K., Talling, P. J., Simmons, S. M., Gwiazda, R., McGann, M., Cartigny, M. J. B., Lundsten, E., Anderson, K., Clare, M. A., Xu, J., Parsons, D., Barry, J. P., Wolfson-Schwehr, M., Nieminski, N. M., and Sumner, E. J. (2019). Linking Direct Measurements of Turbidity Currents to Submarine Canyon-Floor Deposits. *Frontiers in Earth Science*, 7:144.

Mangeney, A., Tsimring, L. S., Volfson, D., Aranson, I. S., and Bouchut, F. (2007). Avalanche mobility induced by the presence of an erodible bed and associated entrainment. *Geophysical Research Letters*, 34(22):L22401.

Mas, V., Mulder, T., Dennielou, B., Schmidt, S., Khripounoff, A., and Savoye, B. (2010). Multiscale spatio-temporal variability of sedimentary deposits in the Var turbidite system (North-Western Mediterranean Sea). *Marine Geology*, 275(1-4):37–52.

Mastbergen, D. R. and Van Den Berg, J. H. (2003). Breaching in fine sands and the generation of sustained turbidity currents in submarine canyons: Breaching in submarine canyons. *Sedimentology*, 50(4):625–637.

Middleton, G. V. (1966). Small-Scale Models of Turbidity Currents and the Criterion for Auto-Suspension. *Journal of Sedimentary Research*, 36(1).

Middleton, G. V. and Hampton, M. (1973). Sediment gravity flows: mechanics of flow and deposition. In Middleton, G. V. and Bouma, A., editors, *Turbidity and Deep Water Sedimentation*, pages 1–38. SEPM, Pacific Section, Short Course Lecture Notes.

Mulder, T. and Alexander, J. (2001). The physical character of subaqueous sedimentary density flows and their deposits. *Sedimentology*, 48(2):269–299.

Mulder, T., Migeon, S., Savoye, B., and Jouanneau, J.-M. (2001). Twentieth century floods recorded in the deep Mediterranean sediments. *Geology*, 29(11):1011–1014.

Mulder, T., Savoye, B., Piper, D. J. W., and Syvitski, J. P. M. (1998). The Var submarine sedimentary system: understanding Holocene sediment delivery processes and their importance to the geological record. *Geological Society, London, Special Publications*, 129(1):145–166.

Mulder, T., Savoye, B., and Syvitski, J. P. M. (1997). Numerical modelling of a mid-sized gravity flow: the 1979 Nice turbidity current (dynamics, processes, sediment budget and seafloor impact). *Sedimentology*, 44(2):305–326.

Mulder, T., Syvitski, J. P., Migeon, S., Faugères, J.-C., and Savoye, B. (2003). Marine hyperpycnal flows: initiation, behavior and related deposits. A review. *Marine and Petroleum Geology*, 20(6-8):861–882.

Nakajima, T. (2006). Hyperpycnites Deposited 700 km Away from River Mouths in the Central Japan Sea. *Journal of Sedimentary Research*, 76(1):60–73.

Nilsen, T. H., Shew, R. D., Steffens, G. S., and Studlick, J. R. J., editors (2008). *Atlas of Deep-Water Outcrops*. American Association of Petroleum Geologists, Oklahoma, U.S.A.

Normandeau, A., Bourgault, D., Neumeier, U., Lajeunesse, P., St-Onge, G., Gostiaux, L., and Chavanne, C. (2020). Storm-induced turbidity currents on a sediment-starved shelf: Insight from direct monitoring and repeat seabed mapping of upslope migrating bedforms. *Sedimentology*, 67(2):1045–1068.

Pantin, H. (1979). Interaction between velocity and effective density in turbidity flow: Phase-plane analysis, with criteria for autosuspension. *Marine Geology*, 31(1-2):59–99.

Parker, G. (1982). Conditions for the ignition of catastrophically erosive turbidity currents. *Marine Geology*, 46(3-4):307–327.

Parker, G., Fukushima, Y., and Pantin, H. M. (1986). Self-accelerating turbidity currents. *Journal of Fluid Mechanics*, 171(-1):145.

Parsons, J. D., Bush, J. W. M., and Syvitski, J. P. M. (2001). Hyperpycnal plume formation from riverine outflows with small sediment concentrations. *Sedimentology*, 48(2):465–478.

Parsons, J. D., Friedrichs, C., Traykovski, P., Mohrig, D., Imran, J., Syvitski, J. P. M., Parker, G., Puig, P., Buttles, J., and Garcia, M. H. (2007). The mechanics of marine sediment gravity flows. In Nittrouer, C. A., Austin, J., Field, M., Syvitski, J. P. M., and Wiberg, P., editors, *Continental Margin Sedimentation: From Sediment Transport to Sequence Stratigraphy*, pages 275–333. Oxford: Blackwell.

Paull, C., Caress, D., Lundsten, E., Gwiazda, R., Anderson, K., McGann, M., Conrad, J., Edwards, B., and Sumner, E. (2013). Anatomy of the La Jolla Submarine Canyon system; offshore southern California. *Marine Geology*, 335:16–34.

Paull, C. K., Caress, D. W., Ussler, W., Lundsten, E., and Meiner-Johnson, M. (2011). High-resolution bathymetry of the axial channels within Monterey and Soquel submarine canyons, offshore central California. *Geosphere*, 7(5):1077–1101.

Paull, C. K., Mitts, P., Ussler, W., Keaten, R., and Greene, H. G. (2005). Trail of sand in upper Monterey Canyon: Offshore California. *Geological Society of America Bulletin*, 117(9):1134.

Paull, C. K., Schlining, B., Ussler, W., Lundste, E., Barry, J. P., Caress, D. W., Johnson, J. E., and McGann, M. (2010a). Submarine Mass Transport Within Monterey Canyon: Benthic Disturbance Controls on the Distribution of Chemosynthetic Biological Communities. In Mosher, D. C., Shipp, R. C., Moscardelli, L., Chaytor, J. D., Baxter, C. D. P., Lee, H. J., and Urgeles, R., editors, *Submarine Mass Movements and Their Consequences*, pages 229–246. Springer Netherlands, Dordrecht.

Paull, C. K., Talling, P. J., Maier, K. L., Parsons, D., Xu, J., Caress, D. W., Gwiazda, R., Lundsten, E. M., Anderson, K., Barry, J. P., Chaffey, M., O'Reilly, T., Rosenberger, K. J., Gales, J. A., Kieft, B., McGann, M., Simmons, S. M., McCann, M., Sumner, E. J., Clare, M. A., and Cartigny, M. J. (2018). Powerful turbidity currents driven by dense basal layers. *Nature Communications*, 9(1).

Paull, C. K., Ussler III, W., Caress, D. W., Lundsten, E., Covault, J. A., Maier, K. L., Xu, J., and Augenstein, S. (2010b). Origins of large crescent-shaped bedforms within the axial channel of Monterey Canyon, offshore California. *Geosphere*, 6(6):755–774.

Peakall, J., Ashworth, P., and Best, J. L. (1996). Physical modelling in fluvial geomorphology: principles, applications and unresolved issues. In Rhoads, B. and Thorn, C., editors, *The Scientific Nature of Geomorphology*, pages 221–253. John Wiley and Sons, Chichester.

Piper, D. J. and Normark, W. R. (2009). Processes That Initiate Turbidity Currents and Their Influence on Turbidites: A Marine Geology Perspective. *Journal of Sedimentary Research*, 79(6):347–362.

Piper, D. J. W. and Aksu, A. E. (1987). The source and origin of the 1929 grand banks turbidity current inferred from sediment budgets. *Geo-Marine Letters*, 7(4):177–182.

Piper, D. J. W., Cochonat, P., and Morrison, M. L. (1999). The sequence of events

around the epicentre of the 1929 Grand Banks earthquake: initiation of debris flows and turbidity current inferred from sidescan sonar. *Sedimentology*, 46(1):79–97.

Piper, D. J. W. and Hundert, T. (2002). Provenance of distal Sohm Abyssal Plain sediments: history of supply from the Wisconsinan glaciation in eastern Canada. *Geo-Marine Letters*, 22(2):75–85.

Piper, D. J. W. and Savoye, B. (1993). Processes of late Quaternary turbidity current flow and deposition on the Var deep-sea fan, north-west Mediterranean Sea. *Sedimentology*, 40(3):557–582.

Piper, D. J. W., Shor, A. N., and Hughes Clarke, J. E. (1988). The 1929 "Grand Banks" earthquake, slump, and turbidity current. In *Geological Society of America Special Papers*, volume 229, pages 77–92. Geological Society of America.

Plink-Björklund, P. and Steel, R. J. (2004). Initiation of turbidity currents: outcrop evidence for Eocene hyperpycnal flow turbidites. *Sedimentary Geology*, 165(1-2):29–52.

Pohl, F., Eggenhuisen, J. T., Kane, I. A., and Clare, M. A. (2020). Transport and Burial of Microplastics in Deep-Marine Sediments by Turbidity Currents. *Environmental Science & Technology*, 54(7):4180–4189.

Pollock, N., Brand, B., and Roche, O. (2016). The controls and consequences of substrate entrainment by pyroclastic density currents at Mount St Helens, Washington (USA). *Journal of Volcanology and Geothermal Research*, 325:135–147.

Pope, E. L., Talling, P. J., and Carter, L. (2017). Which earthquakes trigger damaging submarine mass movements: Insights from a global record of submarine cable breaks? *Marine Geology*, 384:131–146.

Pouliquen, O. and Forterre, Y. (2002). Friction law for dense granular flows: application to the motion of a mass down a rough inclined plane. *Journal of Fluid Mechanics*, 453:133–151.

Prior, D. B., Bornhold, B. D., and Johns, M. W. (1986). Active sand transport along a fjord-bottom channel, Bute Inlet, British Columbia. *Geology*, 14(7):581–584.

Prior, D. B., Bornhold, B. D., Wiseman, W. J., and Lowe, D. R. (1987). Turbidity Current Activity in a British Columbia Fjord. *Science*, 237(4820):1330–1333.

Puig, P., Ogston, A. S., Mullenbach, B. L., Nittrouer, C. A., Parsons, J. D., and Sternberg, R. W. (2004). Storm-induced sediment gravity flows at the head of the Eel submarine canyon, northern California margin: Storm-induced sediment gravity flows. *Journal of Geophysical Research: Oceans*, 109(C3).

Rauter, M., Heerema, C. J., Issler, D., and Talling, P. J. (2019). Applications of the finite area method on a geographic scale: from dense snow avalanches to turbidity currents. In *OpenFOAM Conference 2019*.

Ritchie, J. C. and McHenry, J. R. (1990). Application of Radioactive Fallout Cesium-137 for Measuring Soil Erosion and Sediment Accumulation Rates and Patterns: A Review. *Journal of Environmental Quality*, 19(2):215–233.

Rowe, G. T. (1972). The Exploration of Submarine Canyons and their Benthic Faunal Assemblages. *Proceedings of the Royal Society of Edinburgh. Section B. Biology*, 73:159–169.

Sequeiros, O. E., Bolla Pittaluga, M., Frascati, A., Pirmez, C., Masson, D. G., Weaver, P., Crosby, A. R., Lazzaro, G., Botter, G., and Rimmer, J. G. (2019). How typhoons trigger turbidity currents in submarine canyons. *Scientific Reports*, 9(1):9220.

Sequeiros, O. E., Mosquera, R., and Pedocchi, F. (2018). Internal Structure of a Self-Accelerating Turbidity Current. *Journal of Geophysical Research: Oceans*, 123(9):6260–6276.

Sequeiros, O. E., Naruse, H., Endo, N., Garcia, M. H., and Parker, G. (2009). Experimental study on self-accelerating turbidity currents. *Journal of Geophysical Research*, 114(C5).

Shanmugam, G. (2002). Ten turbidite myths. *Earth-Science Reviews*, 58(3):311–341.

Shanmugam, G. (2018). The hyperpycnite problem. *Journal of Palaeogeography*, 7(1):6.

Silva Jacinto, R. (2008). SOLVEIG I cruise, L'Europe R/V.

Simmons, S. M., Azpiroz-Zabala, M., Cartigny, M. J. B., Clare, M. A., Cooper, C., Parsons, D. R., Pope, E. L., Sumner, E. J., and Talling, P. J. (2020). Novel Acoustic Method Provides First Detailed Measurements of Sediment Concentration Structure Within Submarine Turbidity Currents. *Journal of Geophysical Research: Oceans*, 125(5).

Southard, J. B. and Mackintosh, M. E. (1981). Experimental test of autosuspension. *Earth Surface Processes and Landforms*, 6(2):103–111.

Sovilla, B., McElwaine, J. N., and Louge, M. Y. (2015). The structure of powder snow avalanches. *Comptes Rendus Physique*, 16(1):97–104. Granular physics / Physique des milieux granulaires.

St-Onge, G., Mulder, T., Piper, D. J., Hillaire-Marcel, C., and Stoner, J. S. (2004). Earthquake and flood-induced turbidites in the Saguenay Fjord (Québec): a Holocene paleoseismicity record. *Quaternary Science Reviews*, 23(3-4):283–294.

Stacey, C. D., Hill, P. R., Talling, P. J., Enkin, R. J., Hughes Clarke, J., and Lintern, D. G. (2019). How turbidity current frequency and character varies down a fjord-delta system: Combining direct monitoring, deposits and seismic data. *Sedimentology*, 66(1):1–31.

Stacey, M. W. and Bowen, A. J. (1988). The vertical structure of turbidity currents and a necessary condition for self-maintenance. *Journal of Geophysical Research*, 93(C4):3543.

Stevens, T., Paull, C. K., Ussler, W., McGann, M., Buylaert, J.-P., and Lundsten, E. (2014). The timing of sediment transport down Monterey Submarine Canyon, offshore California. *Geological Society of America Bulletin*, 126(1-2):103–121.

Stevenson, C. J., Feldens, P., Georgiopoulou, A., Schönke, M., Krastel, S., Piper, D. J. W., Lindhorst, K., and Mosher, D. (2018). Reconstructing the sediment concentration of a giant submarine gravity flow. *Nature Communications*, 9(1):2616.

Stevenson, C. J., Talling, P. J., Sumner, E. J., Masson, D. G., Frenz, M., and Wynn, R. B. (2014). On how thin submarine flows transported large volumes of sand for hundreds of kilometres across a flat basin plain without eroding the sea floor. *Sedimentology*, 61(7):1982–2019.

Stow, D. and Aksu, A. (1978). Disturbances in soft sediments due to piston coring. *Marine Geology*, 28(1-2):135–144.

Sulpizio, R., Dellino, P., Doronzo, D., and Sarocchi, D. (2014). Pyroclastic density currents: state of the art and perspectives. *Journal of Volcanology and Geothermal Research*, 283:36–65.

Sumner, E. J. and Paull, C. K. (2014). Swept away by a turbidity current in Mendocino submarine canyon, California: Swept Away. *Geophysical Research Letters*, 41(21):7611–7618.

Symons, W. O., Sumner, E. J., Talling, P. J., Cartigny, M. J., and Clare, M. A. (2016). Large-scale sediment waves and scours on the modern seafloor and their implications for the prevalence of supercritical flows. *Marine Geology*, 371:130–148.

Talling, P. J. (2014). On the triggers, resulting flow types and frequencies of subaqueous sediment density flows in different settings. *Marine Geology*, 352:155–182.

Talling, P. J., Allin, J., Armitage, D. A., Arnott, R. W. C., Cartigny, M. J. B., Clare, M. A., Felletti, F., Covault, J. A., Girardclos, S., Hansen, E., Hill, P. R., Hiscott, R. N., Hogg, A. J., Clarke, J. H., Jobe, Z. R., Malgesini, G., Mozzato, A., Naruse, H., Parkinson, S., Peel, F. J., Piper, D. J. W., Pope, E., Postma, G., Rowley, P., Sguazzini, A., Stevenson, C. J., Sumner, E. J., Sylvester, Z., Watts, C., and Xu, J. (2015). Key Future Directions For Research On Turbidity Currents and Their Deposits. *Journal of Sedimentary Research*, 85(2):153–169.

Talling, P. J., Masson, D. G., Sumner, E. J., and Malgesini, G. (2012). Subaqueous sediment density flows: Depositional processes and deposit types. *Sedimentology*, 59(7):1937–2003.

Talling, P. J., Paull, C. K., and Piper, D. J. (2013). How are subaqueous sediment density flows triggered, what is their internal structure and how does it evolve? Direct observations from monitoring of active flows. *Earth-Science Reviews*, 125:244–287.

Teledyne (2010). ADCP coordinate transformation. P/N 951-6079-00.

Teledyne (2011). Acoustic Doppler Current Profiler principles of operation: a practical primer. P/N 951-6069-00.

Thorne, P. D. and Hanes, D. M. (2002). A review of acoustic measurement of small-scale sediment processes. *Continental Shelf Research*, 22(4):603–632.

Traer, M. M., Hilley, G. E., Fildani, A., and McHargue, T. (2012). The sensitivity of turbidity currents to mass and momentum exchanges between these under-

flows and their surroundings. *Journal of Geophysical Research: Earth Surface*, 117(F1):F01009.

van Loon, A. J. T., Hüneke, H., and Mulder, T. (2019). The hyperpycnite problem: comment. *Journal of Palaeogeography*, 8(1):24.

van Rijn, L. C., Bisschop, R., and van Rhee, C. (2019). Modified sediment pick-up function. *Journal of Hydraulic Engineering*, 145(1):06018017.

Verhagen, I. T. E., Baas, J. H., Jacinto, R. S., McCaffrey, W. D., and Davies, A. G. (2013). A first classification scheme of flow-bed interaction for clay-laden density currents and soft substrates. *Ocean Dynamics*, 63(4):385–397.

Vetter, E. W. and Dayton, P. K. (1999). Organic enrichment by macrophyte detritus, and abundance patterns of megafaunal populations in submarine canyons. *Marine Ecology Progress Series*, 186:137–148.

Wang, Z., Xu, J., Talling, P. J., Cartigny, M. J., Simmons, S. M., Gwiazda, R., Paull, C. K., Maier, K. L., and Parsons, D. R. (2020). Direct evidence of a high-concentration basal layer in a submarine turbidity current. *Deep Sea Research Part I: Oceanographic Research Papers*, 161:103300.

Winterwerp, J. C. (2006). Stratification effects by fine suspended sediment at low, medium, and very high concentrations. *Journal of Geophysical Research*, 111(C5).

Winterwerp, J. C., Bakker, W. T., Mastbergen, D. R., and van Rossum, H. (1992). Hyperconcentrated Sand-Water Mixture Flows over Erodible Bed. *Journal of Hydraulic Engineering*, 118(11):1508–1525.

Winterwerp, J. C., de Groot, M. B., Mastbergen, D. R., and Verwoert, H. (1990). Hyperconcentrated Sand-Water Mixture Flows Over a Flat Bed. *Journal of Hydraulic Engineering*, 116(1):36–54.

Wolman, M. G. and Miller, J. P. (1960). Magnitude and Frequency of Forces in Geomorphic Processes. *The Journal of Geology*, 68(1):54–74. Publisher: The University of Chicago Press.

Wynn, R. B., Huvenne, V. A., Le Bas, T. P., Murton, B. J., Connelly, D. P., Bett, B. J., Ruhl, H. A., Morris, K. J., Peakall, J., Parsons, D. R., Sumner, E. J., Darby, S. E., Dorrell, R. M., and Hunt, J. E. (2014). Autonomous Underwater Vehicles (AUVs): Their past, present and future contributions to the advancement of marine geoscience. *Marine Geology*, 352:451–468.

Xu, J. (2010). Normalized velocity profiles of field-measured turbidity currents. *Geology*, 38(6):563–566.

Xu, J. P., Noble, M. A., and Rosenfeld, L. K. (2004). In-situ measurements of velocity structure within turbidity currents: velocity structure in turbidity currents. *Geophysical Research Letters*, 31(9):n/a–n/a.

Zavala, C. (2019). The new knowledge is written on sedimentary rocks – a comment on Shanmugam's paper "the hyperpycnite problem". *Journal of Palaeogeography*, 8(1):23.

Zavala, C., Arcuri, M., Di Meglio, M., Gamero Diaz, H., and Contreras, C. (2011). A genetic facies tract for the analysis of sustained hyperpycnal flow deposits. In Slatt, R. and Zavala, C., editors, *Sediment transfer from shelf to deep water—Revisiting the delivery system*, pages 31–51. AAPG Studies in Geology.

Zavala, C. and Pan, S. X. (2018). Hyperpycnal flows and hyperpycnites: Origin and distinctive characteristics. *Lithologic Reservoirs*, 30(1):1–27.

Zavala, C., Ponce, J. J., Arcuri, M., Drittanti, D., Freije, H., and Asensio, M. (2006). Ancient Lacustrine Hyperpycnites: A Depositional Model from a Case Study in the Rayoso Formation (Cretaceous) of West-Central Argentina. *Journal of Sedimentary Research*, 76(1):41–59.

Zeng, J., Lowe, D. R., Prior, D. B., Wiseman, W. J., and Bornhold, B. D. (1991). Flow properties of turbidity currents in Bute Inlet, British Columbia. *Sedimentology*, 38(6):975–996.